AD-A190 689 DEVELOPMENT OF ENCAPSULATED LITHIUM HYDRIDE THERMAL ENERGY STORAGE FOR SP (U) OAK RIDGE NATIONAL LAB TN ENGINEERING TECHNOLOGY DIV D G MORRIS ET AL DEC 87 1/2

UNCLASSIFIED ORNL/TM-10413 DE-AC05-84OR21400 F/G 10/4 NL

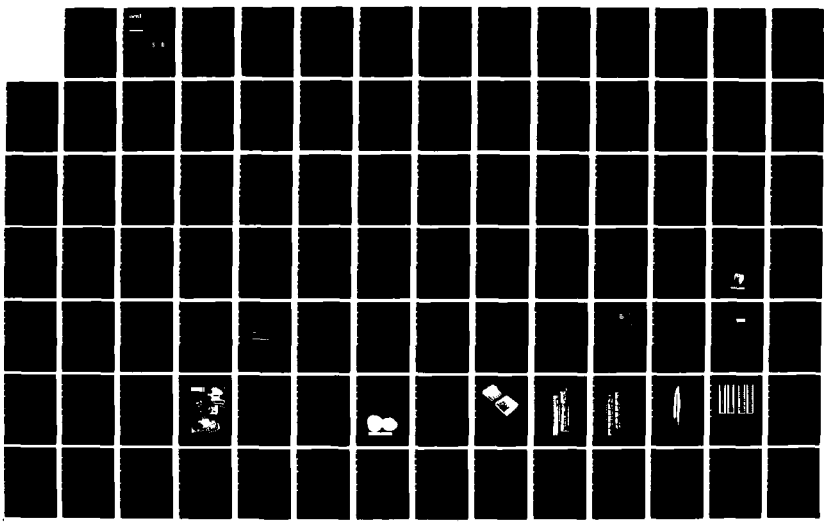

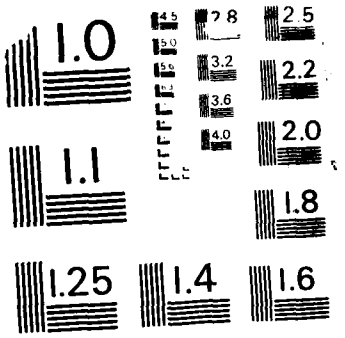

(1)

ornl

ORNL/TM-10413

OAK RIDGE
NATIONAL
LABORATORY

MARTIN MARIETTA

Development of Encapsulated Lithium Hydride Thermal Energy Storage for Space Power Systems

D. G. Morris
J. P. Foote
M. Olszewski

OPERATED BY
MARTIN MARIETTA ENERGY SYSTEMS, INC.
FOR THE UNITED STATES
DEPARTMENT OF ENERGY

Printed in the United States of America. Available from
National Technical Information Service
U.S. Department of Commerce
5285 Port Royal Road, Springfield, Virginia 22161
NTIS price codes—Printed Copy: A06 Microfiche A01

ORNL/TM-10413

Engineering Technology Division

DEVELOPMENT OF ENCAPSULATED LITHIUM HYDRIDE THERMAL ENERGY STORAGE FOR SPACE POWER SYSTEMS

D. G. Morris J. P. Foote
M. Olszewski

Date Published - December 1987

Prepared for the
Air Force Wright Aeronautical Laboratories
AeroPropulsion Laboratory
under
Interagency Agreement DOE 40-1508-84
Air Force MIPR Nos. FY 1455-85-N0617 FY 1455-85-N0632
and FY 1455-86-N0615

Prepared by the
OAK RIDGE NATIONAL LABORATORY
Oak Ridge, Tennessee 37830
operated by
MARTIN MARIETTA ENERGY SYSTEMS, INC.
for the
U.S. DEPARTMENT OF ENERGY
under Contract No. DE-AC05-840R21400

CONTENTS

ACKNOWLEDGMENTS

This work was sponsored by the Air Force Wright Aeronautical Laboratories, AeroPropulsion Laboratory. The authors would like to acknowledge the guidance and assistance provided by J. E. Johnson (program monitor), E. B. Kennel, and E. T. Mahefkey at the Air Force Wright Aeronautical Laboratories. The extensive Y-12 Plant experience in lithium hydride was tapped to accomplish experimental objectives; W. L. Asbury, C. E. Irwin, G. E. Wrenn, and others at the Y-12 Plant have been extremely helpful. The contributions of J. Braunstein, Chemistry Division, and E. H. Guinn, H. W. Hoffman, M. Siman-Tov, and R. P. Wichner of the Engineering Technology Division are appreciated.

DEVELOPMENT OF ENCAPSULATED LITHIUM HYDRIDE THERMAL ENERGY STORAGE FOR SPACE POWER SYSTEMS

D. G. Morris J. P. Foote
M. Olszewski

ABSTRACT

Inclusion of thermal energy storage in a pulsed space power supply will reduce the mass of the heat rejection system. In this mode, waste heat generated during the brief high-power burst operation is placed in the thermal store; later, the heat in the store is dissipated to space via the radiator over the much longer nonoperational period of the orbit. Thus, the radiator required is of significantly smaller capacity. Scoping analysis indicates that use of lithium hydride as the thermal storage medium results in system mass reduction benefits for burst periods as long as 800 s.

A candidate design for the thermal energy storage component utilizes lithium hydride encapsulated in either 304L stainless steel or molybdenum in a packed-bed configuration with a lithium or sodium-potassium (NaK) heat transport fluid. Key issues associated with the system design include phase-change induced stresses in the shell, lithium hydride and shell compatibility, lithium hydride dissociation and hydrogen loss from the system, void presence and movement associated with the melt-freeze process, and heat transfer limitations on obtaining the desired energy storage density.

Preliminary thermal analysis indicates that, for lithium hydride in a sphere of 4-cm maximum diameter, complete lithium hydride melting will be achieved in the 500 s; this provides a subunit with maximum energy storage density. However, an elastic stress analysis indicates that the stresses generated in a rigid spherical shell by the melting lithium hydride will necessitate a thick shell, significantly reducing the energy storage density. This may be mitigated by cracks which form in the lithium hydride during cooldown, providing channels for flow of the melting salt during the charge cycle. Alternative approaches to shell stress reduction would control heat flow so as to locate the void that forms in a region accessible to the melting lithium hydride or to use a flexible shell, such as a bellows, for containment.

Initial scoping experiments with encapsulated lithium hydride have been completed for cylindrical cans of 2.54-cm length, 3.81-cm diameter, and 0.0635 and 0.0889-cm (25 and

35-mil) wall thicknesses. Four thermal cycles were completed without shell failure with a 0.0889-cm (35-mil) thick can. Post-test examination of all cans tested showed the presence of numerous cracks in the lithium hydride.

1. INTRODUCTION

Power levels associated with space defense weapon systems are estimated to be very high, with projections in the multimegawatt power range. Moreover, while these high power levels are required only in a pulsed mode, i.e., for moderately short periods of time, the heat rejection system must still be sized for the full thermal load. Energy storage devices may be employed to reduce the size and mass of power system components. This report documents a study on the use of thermal energy storage (TES) in the heat rejection system for this purpose.

The sink-side TES unit accepts reject heat from the power conversion system during burst power operation. Then, during the remaining portion of the orbit, which is typically an order of magnitude longer than the burst mode period, the stored reject heat is dissipated to space. Thus the heat rejection rate is reduced, and a smaller radiator is required. In concepts where launch packages are constrained by volume rather than mass, this can be a critically important attribute. If the reduction in radiator mass is greater than the additional mass of the storage module, overall system mass savings are possible.

Lithium hydride, because of its superior heat storage properties and convenient melting temperature, appears to be the best candidate for use in sink-side TES applications. To maximize storage density, both sensible and latent heat characteristics of the medium are used. Several TES design concepts based on LiH storage are being evaluated analytically and/or experimentally. One concept employs the direct contact of the heat transport medium (NaK or lithium) with lithium hydride to effect the highest heat transfer rates and storage densities possible.[1] Another approach uses encapsulated shapes of lithium hydride in a packed bed or bulk lithium hydride can be used in a conventional shell and tube configuration.

This report focuses on the encapsulated shapes concept and describes the analytical and experimental work that has been completed to date. Since this program is in its early stages, most of the work has been scoping in nature. However, some fairly detailed phase-change heat transfer analysis has been performed in spherical geometry. In addition, analytical efforts have been extended to characterizing the behavior of the void which occurs due to the large lithium hydride volumetric shrinkage during the solidification process.

Analytical and experimental work have addressed basic feasibility issues associated with encapsulated lithium hydride: phase-change induced stresses on heat-up, hydrogen diffusion through shell walls, heat transfer rate, void behavior, and material constraints. The impact of these issues on the design of lithium hydride encapsulated shapes has been evaluated, and design alternatives have been identified for circumventing the key problem areas.

The following sections of this report contain a description of the encapsulated shape design concept a presentation of the analytical work completed, results of an assessment of the value (i.e., power system mass and area savings) of sink-side thermal energy storage are presented, and an evaluation of the feasibility issues. This is followed by a discussion of the initial scoping experiments with encapsulated lithium hydride. Finally, based on work to date, preliminary conclusions are provided.

2. SYSTEM CONCEPT ANALYSIS

A preliminary system value analysis was performed to determine if the heat storage/rejection concept had sufficient merit to warrant development. The analysis also was useful in determining, in a preliminary manner, the minimum required storage density that resulted in the encapsulated lithium hydride storage unit concept being feasible for burst power applications. A scoping design analysis was then conducted to determine if the storage unit could be designed to meet the storage density goals.

2.1 System Concept

A simplified schematic of a no effluent space power system employing encapsulated sink-side thermal storage is shown in Fig. 2.1. Depending upon the application the heat source could be nuclear, chemical or solar. Power conversion can be accomplished using dynamic systems such as Rankine and Brayton cycles, or static systems such as thermionics. As mentioned previously waste heat would be stored in the encapsulated lithium hydride during burst power operation. The stored heat would then be rejected over the longer, non-operational portion of the orbit. The candidate heat transport fluids include NaK and lithium, while the radiator could utilize heat pipe technology. Other technologies as they are developed would provide alternatives.

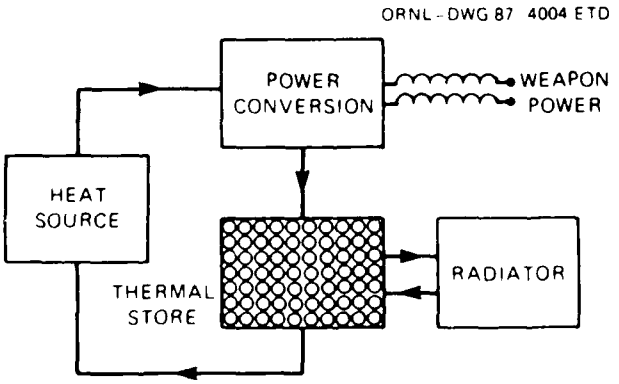

Fig. 2.1. Schematic of power system employing encapsulated sink-side thermal storage.

2.2 Value Analysis

The mass of the heat rejection system using storage was compared to the mass of the baseline system, which used only a radiator, to give a measure of the value of the storage system. In the baseline system, waste heat is rejected immediately via radiation during the power generation portion of the orbit. Thus, the radiator is sized to handle the instantaneous load imposed by the power cycle. With thermal storage the reject heat is placed into storage during the power generation portion of the orbit; then, during the non-operational portion of the orbit the stored heat is rejected via radiation.

The major parameters of concern include: energy storage density, minimum temperature of the storage medium, burst operation period and radiator specific mass. The storage density depends upon the design of the unit (which is addressed in the subsequent section) and the temperature swing (the difference between the maximum and minimum storage temperature). The storage medium utilizes the sensible heat of the liquid and solid phases in addition to the latent heat of fusion. Thus, the total heat stored is strongly influenced by the temperature swing. The maximum temperature of the storage unit is controlled by the reactor coolant temperature, which in this analysis was assumed to be 1100 K. The temperature swing, therefore, was fixed by the minimum storage temperature. Variation of the minimum storage temperature produces two opposing effects. As the minimum storage temperature increases, the temperature swing decreases. This decreases the storage density and increases the required storage mass. However, the average radiator flux increases and this decreases the required radiator area and mass.

The total orbit time was fixed at 6000 s and the burst period varied between 100 and 900 s. Thus, the non-operational period (the time available for heat rejection) varied between 5900 and 5100 s. The baseline (i.e., non-storage) system radiator was assumed to operate at 1100 K. This results in a radiator heat flux of 74.3 kW/m^2. The radiator specific mass was fixed at 20 kg/m^2, which is felt to be representative of a survivable heat pipe system.

Previous analysis by Olszewski and Morris[2] indicated that the optimal heat storage/rejection system operated with minimum storage temperature in the range of 500 to 700 K. The analysis was, therefore, confined to this range of lower operating temperatures.

The value analysis results are given in Fig. 2.2. The crossover time is defined as the time at which the storage heat rejection and the radiator-only systems are of equal mass. For total generation times less than the crossover time the storage system is lighter. Thus, a storage heat rejection system with a storage density of 3 MJ/kg operating with a lower temperature of 700 K will show advantage over a radiator-only system for generation times of 600 s or less. As anticipated but not illustrated in the figure (see Ref. 2 for details) the value of storage (i.e., mass savings) increases with decreasing generation time. To have reasonable applicability to burst power needs it is desirable that the storage system have a crossover time of at least 500 s. From Fig. 2.2 it is evident that this will require a system storage density of at least 3 MJ/kg. Thus, the research program is directed at achieving a system storage density exceeding this value.

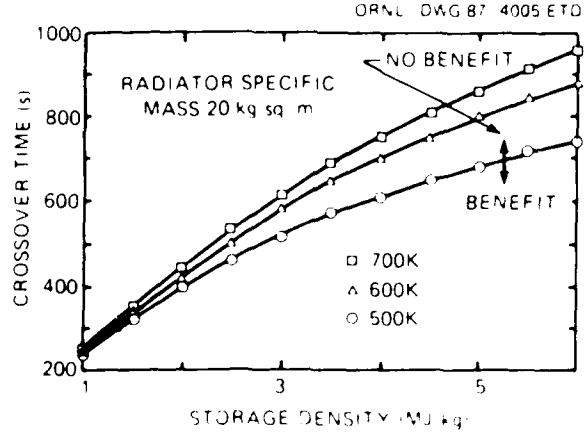

Fig. 2.2. Heat rejection system crossover time for varying minimum storage temperatures.

2.3 Storage System Conceptual Design

Preliminary system conceptual designs were prepared for the proposed storage system using encapsulated lithium hydride shapes in a

packed bed configuration. The purpose of this design analysis was to determine if the system storage densities could meet the goal of 3 MJ/kg or greater as determined by the value analysis. Conceptual designs were completed for modules that would meet the requirements of the following mission:

- burst generation time, 500 s
- system output power, 300 MW(e)
- power system efficiency, 25%
- reject heat load, 900 MW(t)
- heat stored, 450 GJ.

The TES system operational storage density depends upon many design related factors. The storage medium used, thickness of the encapsulating shell, packing density of the encapsulated shapes and choice of coolant have significant impact on the mass requirements of the non-storage components of the unit and this affects the storage density of the system.

System storage densities were calculated for several design options. Lithium and NaK were examined as the heat transport fluids. Also, the storage medium was examined using naturally occurring lithium (Li^7) and the isotope lithium 6 (Li^6). Preliminary information indicates that Li^6 possess the same molar thermal properties as Li^7. Thus, on a mass basis the heat of fusion and specific heat will be 12% higher for the Li^6.

It was assumed that the lithium hydride was formed in spheres and encapsulated with a 0.013-cm (5-mil) thick stainless steel shell (this shell thickness assumption represents a design goal). As described in Sect. 3.2, lithium hydride heat transport properties limit the maximum lithium hydride sphere diameter to 3.8 cm (the maximum sphere diameter that allows for complete melting of the lithium hydride in the 500 s burst time). With this design the mass of the lithium hydride sphere (using Li^7) is 15.8 g and that of the steel shell is 4.7 g.

Results of the design analysis are presented in Table 2.1. As indicated by these results lithium is the preferred thermal transport medium since all designs yield storage system densities in excess of

Table 2.1. Storage system operational energy densities (MJ/Kg)

Minimum store temperature (K)	LiH only		Encapsulated							
			Li^7				Li^6			
	Li^7	Li^6	75%		60%		75%		60%	
			NaK	Li	NaK	Li	NaK	Li	NaK	Li
300.	7.90	9.04	4.46	5.32	3.70	5.02	4.78	5.76	3.91	5.37
400.	7.44	8.51	4.20	4.99	3.47	4.68	4.50	5.40	3.67	5.01
500.	6.96	7.96	3.92	4.65	3.23	4.34	4.21	5.03	3.42	4.64
600.	6.42	7.34	3.62	4.27	2.97	3.96	3.88	4.62	3.14	4.23
700.	5.80	6.63	3.27	3.84	2.68	3.53	3.51	4.16	2.83	3.78

3 MJ/kg. The use of Li^6 is also preferred because of its enhanced storage density. As indicated by the detailed mass breakdown information presented in Table 2.2 the mass of the encapsulated storage medium (lithium hydride and shell) and the coolant essentially determine the system mass. Since the storage capacity of the coolant is much less than that of the encapsulated lithium hydride (<10% of the storage capacity of the lithium hydride), increasing the packing density (by using two sphere sizes) has a significant impact.

Table 2.2. Storage system detailed mass breakdown for 700 K minimum storage temperature design option

Storage medium lithium isotope	Coolant	Packing density (%)	Mass (kg)			
			Storage medium	Coolant	Piping container etc.	Total
Li^7	NaK	60	95,377	68,316	4,500	168,194
Li^6	NaK	60	86,225	68,471	4,500	159,196
Li^6	Li	60	79,435	35,146	4,500	119,081
Li^6	Li	75	84,870	18,776	4,500	108,146

Using the results in Table 2.1 with those in Fig. 2.2 confirm the applicability of the packed bed design for burst power needs. The design using Li^6, a packing density of 75% and lithium coolant yields an operational storage density of 4.2 MJ/kg at a minimum storage temperature of 700 K. Combining these values with the value analysis results in Fig. 2.2 indicates that the storage system would be attractive for burst times as long as 800 s. This greatly exceeds the original goal of 500 s.

In summary, system storage densities of 3 MJ/kg or greater will be required to produce a feasible sink-side heat storage unit. It is reasonable to expect operational storage densities in excess of 3 MJ/kg using the encapsulated lithium hydride packed bed concept. The most promising system uses Li^6 as the storage medium with a packing density of 75% and lithium as the thermal transport medium.

3. DEVELOPMENT ISSUES AND EVALUATION

3.1 Overview of Issues

As indicated in Sect. 2.3, the lithium hydride encapsulating shell must be sufficiently thin to achieve a storage system design which provides overall system mass savings. However, there are several factors (design issues) which might not allow the use of a thin shell, and therefore need to be investigated. The key issue of concern is stress induced in the shell during heatup. The stress results from hydrostatic forces as lithium hydride expands during phase change. A second area of concern is hydrogen diffusion through the shell. The rate of hydrogen loss varies inversely with shell thickness. Thus, hydrogen loss increases with decreasing shell thickness.

As mentioned previously, if lithium hydride is encapsulated in spheres, the poor heat transport properties of lithium hydride limit the maximum sphere size to about 3.8 cm (for a 500 s burst time). Void behavior plays a key role in assessing the design limitations resulting from poor lithium hydride heat transport, and even more importantly, on phase-change induced shell stress. A void at a shell surface reduces heat transfer although hydrogen is a good gas thermal conductor. The way in which the void influences shell stress is described later in this section.

From a materials standpoint, compatibility of the shell with lithium hydride, lithium, and hydrogen is required over a fairly wide range of temperatures. However, compatibility concerns are somewhat mitigated by the rather short projected system integrated operating time. Other materials concerns include thermal shock resistance, material cost, ease of fabrication, strength, and ductility.

Sections 3.2 through 3.6 describe models, analysis, and research conducted to date to assess and resolve the key design issues.

3.2 Thermal Analysis

3.2.1 Description of heat transfer model

A two-dimensional finite difference heat transfer computer code is being developed to model the thermal performance of lithium hydride encapsulated in a spherical shell. The model uses the "enthalpy" method to account for phase change in the salt. In the enthalpy method, the location of the phase change front is not determined directly but is inferred from the energy content of the material. This method has been used extensively at ORNL, for example see Refs. 3 and 4. A non-typical aspect of the present computer program is that the fully implicit form of the heat balance equations is solved, rather than the explicit form usually employed. The two main reasons for using the fully implicit solution are to avoid stability problems associated with the explicit solution and to minimize the difficulty in implementing a natural convection model during the latter part of the project. Heat balance equations are solved on a regular grid in r, θ coordinates. The equations are solved directly for the one-dimensional case or by line relaxation for the two-dimensional case. The solution method is given in Ref. 5. Temperatures are scaled so the scaled temperature, T', at the melt point is zero:

$$T' = T - T_{mp} ,$$

where

$$T_{mp} \approx 956 \text{ K } (1260^0\text{F})$$

Energy content is scaled so the energy content, E, of the solid at the melt point is zero. Therefore,

$$E = C_s T' \qquad \text{For } T' < 0$$

$$E = C_\ell T' + H_{s\ell} \qquad \text{For } T' > 0$$

where C_s and C_ℓ are the specific heats of the solid and liquid, and $H_{s\ell}$ is the heat of fusion [$\approx$ 2.6 MJ/kg ($\approx$1109 Btu/lbm)]. When a given node

has $0 < E < H_{s\ell}$, the temperature is fixed at zero until enough heat is added or removed so $E > H_{s\ell}$ or $E < 0$.

Results from the finite difference model were compared to an analytical solution for a one-dimensional Stefan problem for a sphere. In the problem considered, a sphere of lithium hydride is initially liquid at the fusion temperature. At time = 0 a temperature 56 K (100°F) below the fusion temperature is applied at the outer surface and is maintained thereafter. Density, specific heat and thermal conductivity are considered to be constant. An asymptotic solution for this problem is given in Ref. 6. In Fig. 3.1 the predicted phase front locations for the finite difference calculation and the analytical solution are compared (R_o is the radius of the sphere).

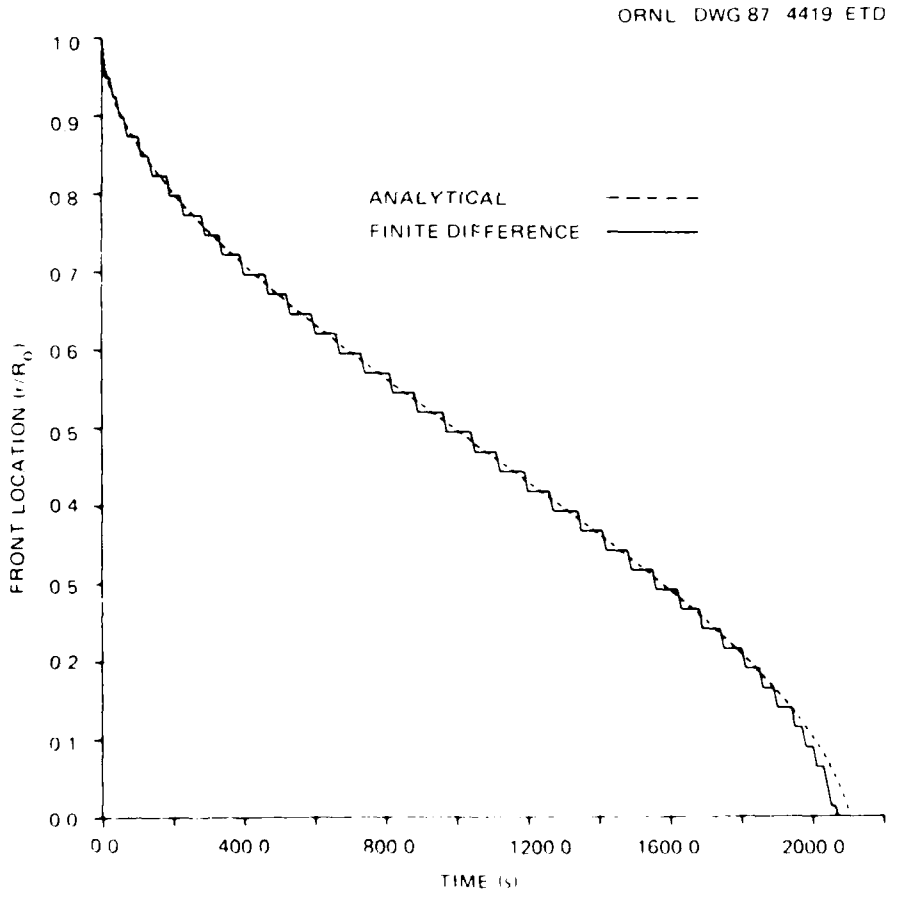

Fig. 3.1. Comparison of phase front location predicted by analytical solution and finite difference calculation for one-dimensional Stefan problem.

As can be seen from the plot, agreement between the two solutions was satisfactory. Results of two-dimensional calculations were checked against results from the explicit HEATING6 code (see Ref. 4) and were found to agree within 1%, thus confirming that the numerical formulation was correct. Comparison with experimental results will be needed to validate the model.

3.2.2 Heat transfer analysis

The finite difference code was used to determine the thermal response of single spheres of various diameters exposed to liquid metal convection when the fluid temperature undergoes a step change from 300 K (80°F) to 1100 K (1520°F). This simulates the power-up of an orbital power system where spheres containing lithium hydride arranged in a packed bed would be used as a heat sink with NaK or lithium as the heat transfer fluid. Theoretical relationships for convection coefficients for a liquid metal flowing past a single sphere have been developed. The convection coefficient for a single sphere varies strongly with angle from the leading stagnation point, with a maximum at the leading stagnation point and a minimum at the trailing stagnation point. However, it was felt that an average value over the entire surface would be more representative of convection in a packed bed. Based on correlations given in Ref. 7, an average value of 17 kW/m^2-K (3000 Btu/h-ft^2-°F) [for a fluid velocity of 0.30 m/s (1 ft/s)] was used in the study.

The mass of lithium hydride in the spheres was set so they are completely filled when the lithium hydride is liquid. The shells are stainless steel, with thickness equal to 1% of the inside radius [e.g., for R_i = 1.9 cm, shell thickness = 0.019 cm (7.5 mil)]. Linear scaling of shell thickness can be justified due to stress considerations, and as a result the shell has no effect when comparing the specific energy content of different size spheres. Properties for the shell material, and solid and liquid lithium hydride were considered to be constant. A list of property values used in the study is given in Table 3.1.

In order to formulate a thermal model for melting of lithium hydride in a sphere, two important assumptions must be made. The first of these is the initial location of the void in the solid material. The

Table 3.1. Property values used in thermal analysis

Material	Density, g/cm^3 (lbm/ft^3)	Specific heat J/g-K (Btu/lbm-°F)	Thermal conductivity J/s-cm-K (Btu/h-ft-°F)
Solid LiH	0.69 (43.08)	6.28 (1.50)	0.042 (2.42)
Liquid LiH	0.55 (34.30)	7.37 (1.76)	0.021 (1.21)
Stainless steel	7.81 (487.6)	0.582 (0.139)	0.22 (12.86)

LiH melt temperature = 956 K (1260°F).

LiH heat of fusion = 2.58 MJ/kg (1109 Btu/lbm).

behavior of the void during solidification is not well understood, and developing an understanding of void mechanics is one of the main goals of this project (void mechanics is discussed in detail in Sect. 3.3). Minimum energy considerations indicate that in the case of uniform cooling in micro-gravity, a spherical void will form in the center of the container (no stability analysis has been done to determine if other shapes are possible). This assumption is made in the present study. A second critical assumption that must be made concerns how the volumetric expansion due to melting is accounted for in the case where the liquid is not in contact with the void. The first possibility is that the shell expands to provide the required volume. This case is not of interest in the heat transfer study, since any practical shell would be able to expand very little before rupturing. It is, however, of great interest in determining the design of the shell. This problem is discussed in detail in Sect. 3.4.4. A second way the volume expansion could be accommodated is for the solid to be crushed uniformly inward into the void. Whether or not this is a realistic possibility with a practical shell thickness depends on the compressive strength of the solid lithium hydride, but in any event it provides a limiting case for the heat transfer study. A third possibility is for the excess liquid to leak through the solid into the void. This would likely occur if there are sufficient cracks in the solid. Heat transfer calculations were carried out assuming the second case mentioned above, hereafter referred to as the "crush" model, and the last case, hereafter referred

to as the "leak" model. In the leak model calculations, the means by which the liquid makes its way through the solid is not considered. It is assumed that liquid at the fusion temperature appears in a freezing volume at the inner surface of the solid. In reality, the phase front at the inner surface of the solid may not be uniform since the liquid passes through localized cracks in the solid. The processes involved in the two models are illustrated in Fig. 3.2.

Figure 3.3 compares the fraction of the lithium hydride melted versus time for the crush and the leak models. The results shown are

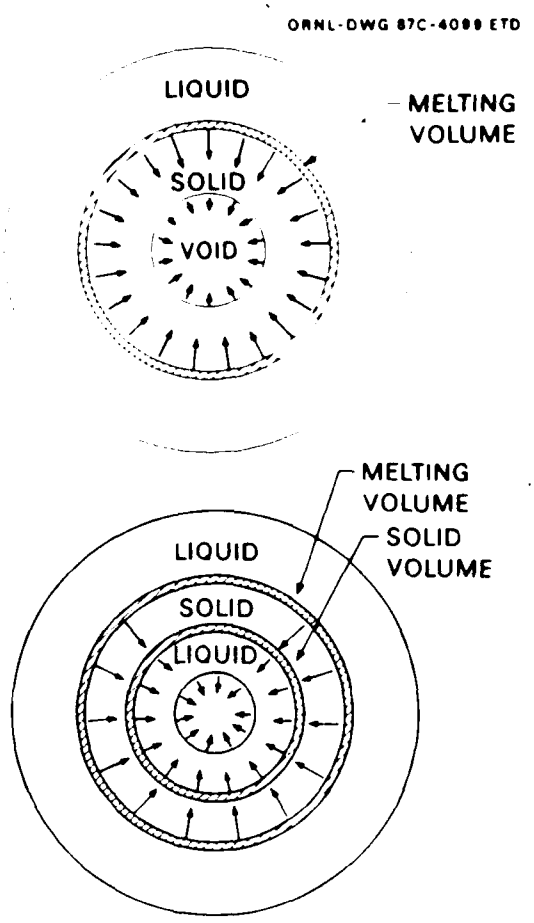

Fig. 3.2. Crush and leak thermal models.
a. Crush model — solid is uniformly crushed toward center to account for volume expansion at melt front.
b. Leak model — excess liquid from melting volume appears in freezing volume at inner surface of solid. How it gets there is not considered.

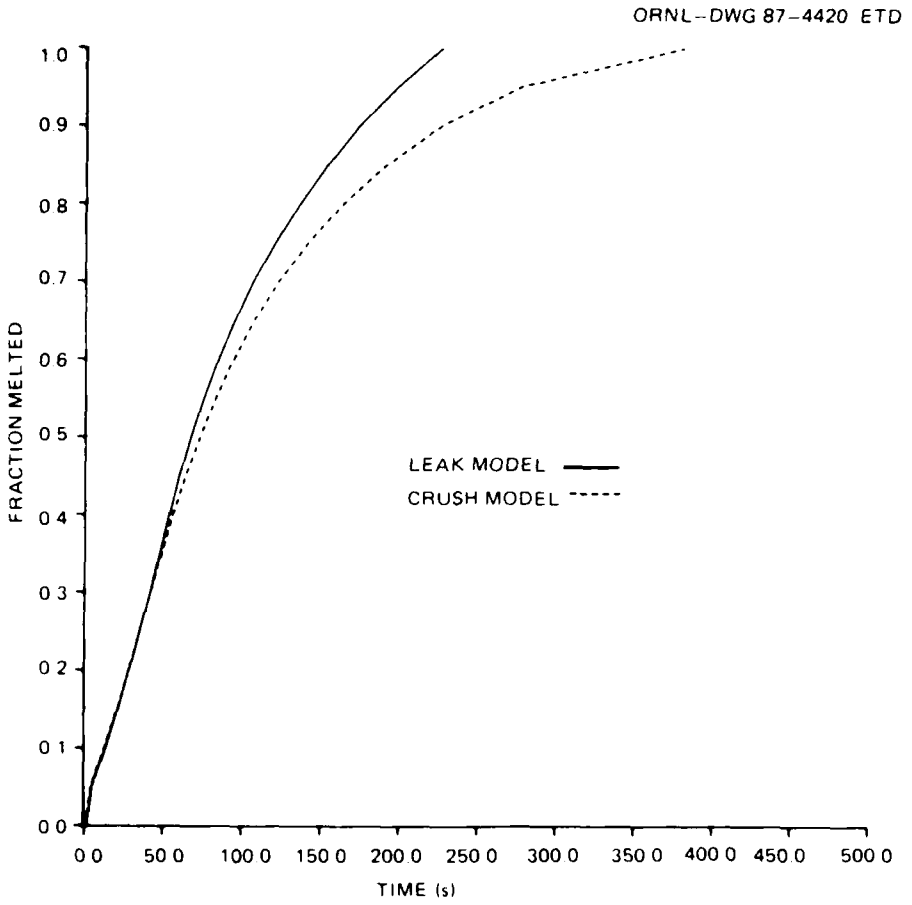

Fig. 3.3. Fraction melted versus time, R_o = 1.9 cm.

for a 1.9-cm radius sphere. During the early stage of the melting process, the two models give very similar results, but as the process continues the rate of melting predicted by the leak model begins to exceed that of the crush model. This difference increases with time. This result is due primarily to two effects. The conduction path through the liquid is shorter in the leak model. In addition, some heat is carried along with the liquid that leaks through the solid and thus bypasses the conduction path through the solid.

Figure 3.4 shows a comparison of energy gain vs time for spheres ranging from 0.635 to 3.81 cm in radius. Assuming a total time of 500 s available for charging, the 1.9-cm radius sphere is the largest that attains its maximum potential energy storage in the required time. As shown in Fig. 3.5, the 3.81-cm radius sphere requires about 900 s to

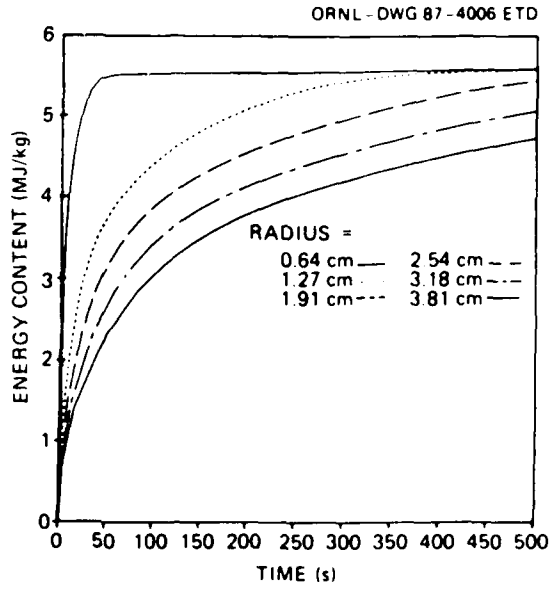

Fig. 3.4. Energy storage versus time for lithium hydride spheres (leak model).

completely melt. Table 3.2 lists energy content after 500 s for the various sphere sizes predicted by the crush and leak models. It is interesting to note that the results for the two cases do not differ greatly (the maximum difference is about 2%).

In summary, the mechanism by which the volume expansion due to melting is accommodated is not critical in the heat transfer model, as

Table 3.2. Energy content at 500 s for various sphere sizes

Diameter		Energy content at t = 500 s			
		Crush model		Leak model	
(cm)	(inches)	(MJ/kg)	(% max)	(MJ/kg)	(% max)
1.27	0.50	5.560	100.0	5.559	100.0
2.54	1.00	5.558	99.96	5.558	99.98
3.81	1.50	5.532	99.50	5.550	99.84
5.08	2.00	5.260	94.60	5.412	97.36
6.35	2.50	4.918	88.45	5.039	90.65
7.62	3.00	4.611	82.93	4.701	84.57

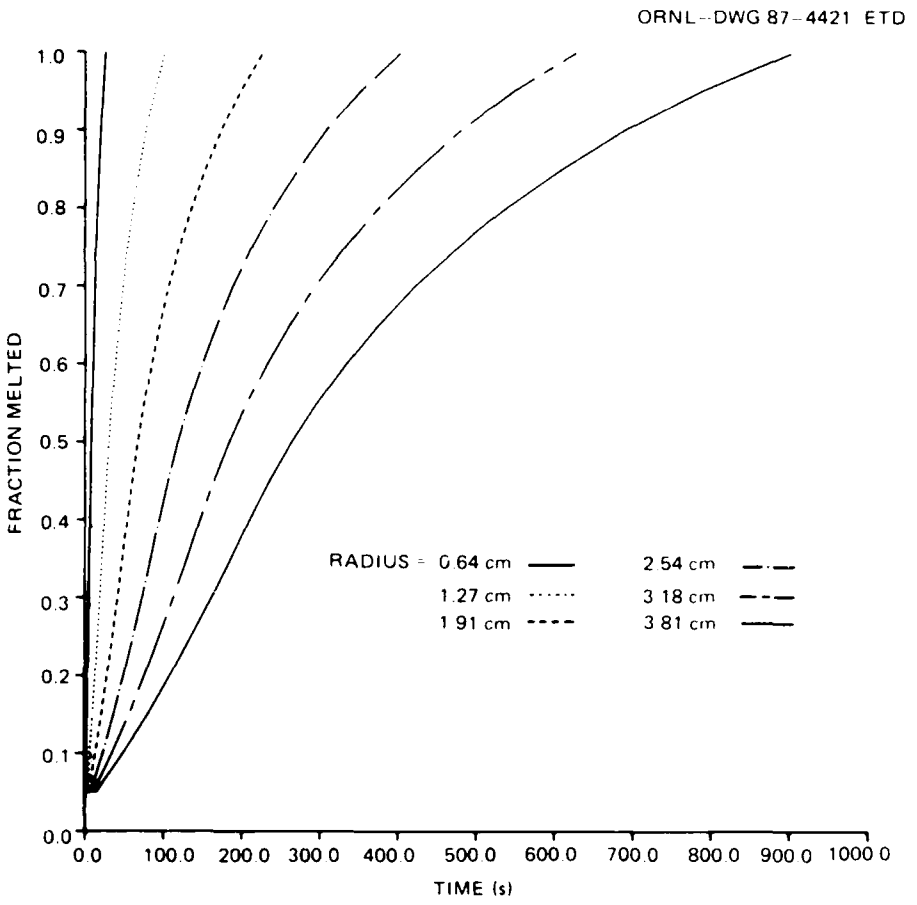

Fig. 3.5. Fraction melted versus time for lithium hydride spheres (leak model).

the crush and leak models give very similar results. Both models indicate that for complete melting in 500 s with an 1100 K source temperature, the maximum container diameter that can be used is about 3.81 cm.

3.3 Void Mechanics

3.3.1 Physics of solid-liquid-vapor systems

Determination of liquid-vapor interface shapes is a class of problems which has received a great deal of study. However, with the exception of some relatively simple geometries, no straightforward method of solving for interface shapes is available. Surface energy

arises because molecules at the surface of a liquid are not attracted equally from all sides as are those in the bulk liquid. Thus, these molecules have some excess energy compared to molecules in the bulk liquid. The unequal attraction experienced by the surface molecules results in a force acting along the liquid surface. This force can be represented as a uniform tension acting on a hypothetical membrane stretched over the surface and is referred to as surface tension, σ. The relationship of the surface tensions between the liquid and vapor, $\sigma_{\ell v}$, the solid and vapor, σ_{sv}, and the solid and liquid, $\sigma_{s\ell}$, is expressed by the equation

$$\sigma_{\ell v} \cos \theta = \sigma_{sv} - \sigma_{s\ell}$$

where θ is the angle of contact between the solid and liquid. This relationship, known as Young's equation, is usually represented as a force balance as shown in Fig. 3.6. It is questionable if it can be

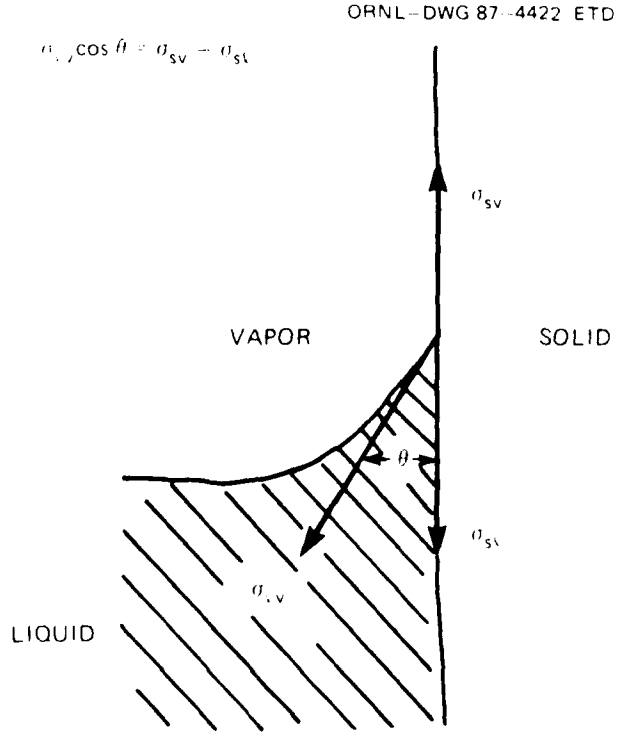

Fig. 3.6. Contact angle — Young's equation.

justified on that basis, however, since the force normal to the solid surface is not balanced. Alternately, Young's equation can be derived based on thermodynamic considerations.[8]

Although the surface tension and contact angle are manifestations of microscopic forces, together they have been found to provide an adequate representation of the macroscopic behavior of capillary systems. The main disadvantage of the surface tension-contact angle representation is that the contact angle can be strongly influenced by the condition of the surface and is subject to hysteresis when the liquid advances or recedes, thus causing some uncertainty in calculations.

There are two basic approaches that can be used to calculate interface shapes. The first involves minimizing the free energy, F, of the system, which for an isothermal capillary system of mass, m, is the sum of the surface energy and potential energy, and can be expressed as:

$$F = \int_{A_c} \sigma \, dA + \int_V \rho g h \, dV$$

where A_c is the capillary area, V is the total system volume and h is the elevation relative to a fixed reference. The equation for the minimum energy surface can be determined by applying the calculus of variations ($\delta F = 0$) with the constraint that the liquid volume is constant. This method has been applied successfully to determine equilibrium interface shapes in axisymmetric containers.[9]

A second method that can be used to calculate interface shapes involves balancing forces on the interface. Consider a small surface element dA of the liquid-vapor interface as shown in Fig. 3.7. Element dA has minimum and maximum radii of curvature R_1 and R_2 with origins along the normal to dA. Since they represent principal (maximum and minimum) curvatures, the planes of R_1 and R_2 are perpendicular to each other. The length, L_1, of dA in the plane of R_1 is $R_1\Delta\theta_1$, where $\Delta\theta_1$ is assumed to be very small. Similarly, the length L_2 of dA in the plane of R_2 is $R_2\Delta\theta_2$. In order for forces directed along the normal to be balanced, the normal component of the surface tension forces acting on the edges of dA must equal the pressure force on dA. The equation expressing the

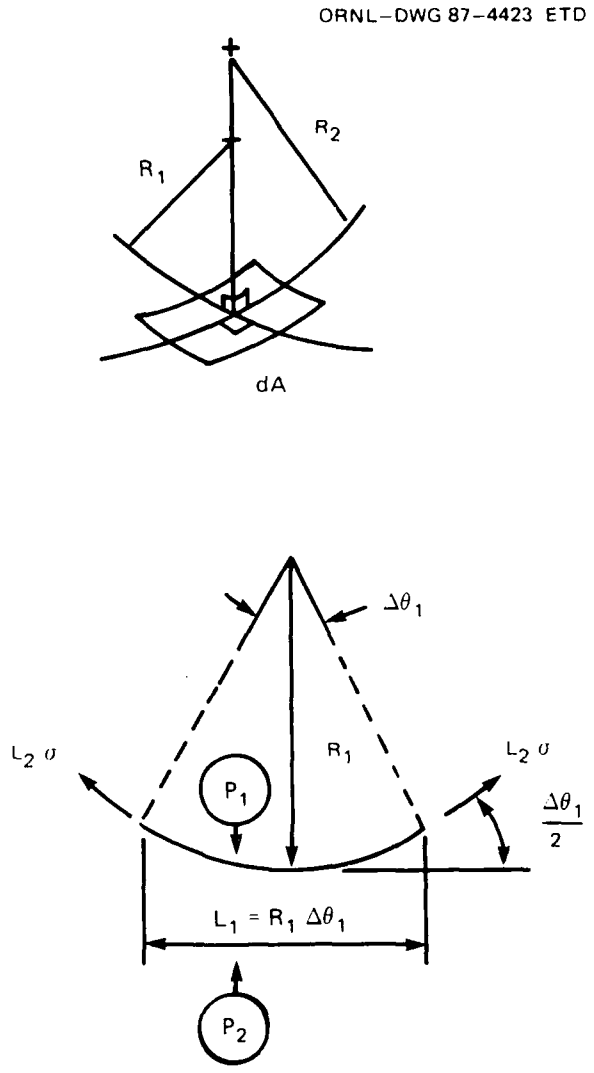

Fig. 3.7. Force balance method — Laplace equation.

force balance is

$$(P_1 - P_2)\, L_1 L_2 = 2L_1\sigma \sin\frac{\Delta\theta_2}{2} + 2L_2\sigma \sin\frac{\Delta\theta_1}{2}$$

Substituting for L_1 and L_2 in terms of R and $\Delta\theta$, and assuming

$\sin \Delta\theta \approx \Delta\theta$, the equation becomes

$$(P_1 - P_2)(R_1\Delta\theta_1)(R_2\Delta\theta_2) = 2(R_1\Delta\theta_1)\,\sigma\,\frac{\Delta\theta_2}{2} + 2\,(R_2\Delta\theta_2)\,\sigma\,\frac{\Delta\theta_1}{2}$$

which reduces to

$$P_1 - P_2 = \sigma\left(\frac{1}{R_1} + \frac{1}{R_2}\right) \tag{3.1}$$

Equation (3.1) is called the Laplace equation and is the classical expression for equilibrium of a liquid-vapor interface. It should be noted that the Laplace equation can also be derived from minimum energy considerations.[10] Of course, both of the methods mentioned above must give the same result, so the choice of method depends on the particular problem being considered. Most sources indicate that the minimum energy formulation is more straightforward for most situations, with the exception of a few simple cases. However, it appears that the number of cases, simple or otherwise, for which a closed form solution can be obtained is very limited.

3.3.2 Determination of interface shape for an axisymmetric case

Fortunately, for an axisymmetric case a vertical force balance can be used to find the interface shape. Consider an element of the interface with length dL, as shown in Fig. 3.8. This element forms an annular ring about the axis of symmetry. The pressure difference across the interface is $P_v - P_\ell$, where P_v and P_ℓ are the vapor and liquid pressures. P_ℓ can be expressed in terms of the liquid pressure at the origin, $P_{\ell o}$, and the hydrostatic head; so

$$P_v - P_\ell = P_v - P_{\ell o} + \rho g z$$

The projected area that the pressure difference acts over is $2\pi r\Delta r$. Therefore the pressure force in the -z direction is

$$(P_v - P_{\ell o} + \rho g z)\; 2\pi r\Delta r$$

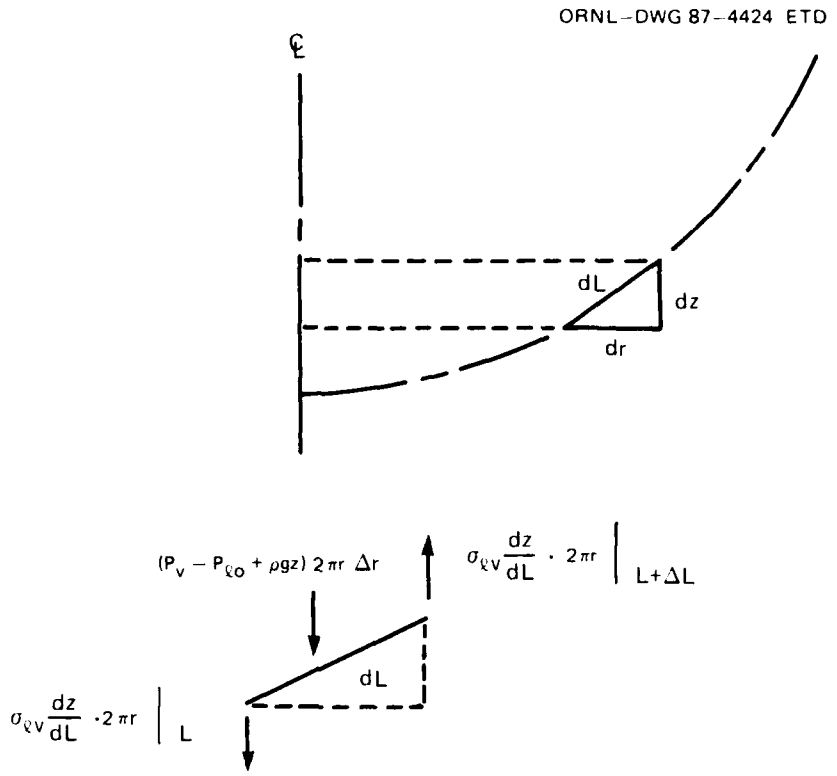

Fig. 3.8. Vertical force balance for axisymmetric interface.

Surface tension forces act along the edges of the element at L and L + ΔL. The surface tension force at each edge is given by $\sigma_{\ell v}\ (2\pi r\ )$, and the vertical component is

$$\sigma_{\ell v}\ (2\pi r)\ \frac{\Delta z}{\Delta L}$$

The expression for the force balance is therefore

$$(P_v - P_{\ell o} + \rho gz)\ 2\pi r\ \Delta r = \sigma_{\ell v}\ (2\pi r)\ \frac{\Delta z}{\Delta L}\Big|_{L\ +\ \Delta L} - \sigma_{\ell v}\ (2\pi r)\ \frac{\Delta z}{\Delta L}\Big|_{L}$$

which can be rewritten

$$(P_v - P_{\ell o} + \rho gz)\ r\ \frac{\Delta r}{\Delta L} = \frac{\sigma_{\ell v}\ r\ \frac{\Delta z}{\Delta L}\Big|_{L\ +\ \Delta L} - \sigma_{\ell v}\ r\ \frac{\Delta z}{\Delta L}\Big|_{L}}{\Delta L}$$

Taking the limit as $\Delta L \to 0$, the differential equation is

$$(P_v - P_{\ell o} + \rho gz)\, r \frac{dr}{dL} = \frac{d}{dL}\left(\sigma_{\ell v}\, r \frac{dz}{dL}\right) \tag{3.2}$$

For a constant surface tension case, the right side of Eq. (3.2) can be differentiated to give

$$(P_v - P_{\ell o} + \rho gz)\, r \frac{dr}{dL} = \sigma_{\ell v}\left(\frac{dr}{dL} \cdot \frac{dz}{dL} + r \frac{d^2z}{dL^2}\right)$$

which can be rearranged yielding

$$\frac{d^2z}{dL^2} = \left(\frac{P_v - P_{\ell o}}{\sigma_{\ell v}} + \frac{\rho gz}{\sigma_{\ell v}} - \frac{1}{r}\frac{dz}{dL}\right) \frac{dr}{dL} \tag{3.3}$$

At this point two simplifications can be introduced. Using Eq. (3.1), the pressure difference at the origin can be expressed in terms of the radius of curvature at the origin, where $R_1 = R_2 = R_0$, giving

$$P_v - P_{\ell o} = \frac{2\sigma_{\ell v}}{R_o}$$

or

$$\frac{P_v - P_{\ell o}}{\sigma_{\ell v}} = \frac{2}{R_o} \tag{3.4}$$

The relationship between $\frac{dr}{dL}$ and $\frac{dz}{dL}$ is

$$\left(\frac{dr}{dL}\right)^2 + \left(\frac{dz}{dL}\right)^2 = 1$$

or

$$\frac{dr}{dL} = \sqrt{1 - \left(\frac{dz}{dL}\right)^2}\,. \tag{3.5}$$

Substituting Eqs. (3.4) and (3.5) into Eq. (3.3) yields

$$\frac{d^2z}{dL^2} = \left(\frac{2}{R_o} + \frac{\rho gz}{\sigma_{\ell v}} - \frac{1}{r}\frac{dz}{dL}\right) \sqrt{1 - \left(\frac{dz}{dL}\right)^2} \tag{3.6}$$

Eqs. (3.5) and (3.6) can be solved by the Runge-Kutta method to yield interface shapes for given values of $\sigma_{\ell v}$, ρ and g. The solution is iterative, with values of R_o being guessed to provide the required vapor volume and contact angle between the liquid and container. Equations similar to Eqs. (3.5) and (3.6) were used in Ref. 11 to develop an extensive set of curves that give meniscus shape as a function of $\rho g/\sigma_{\ell v}$ and θ. Figure 3.9 shows interface shapes for liquid lithium hydride in a spherical container for void fractions ranging from 5 to 25%. It should be noted that for the micro-gravity case the interface shape is a segment of a sphere, and for the case where $\theta = 0°$, shown in Fig. 3.9c, the interface is a spherical bubble which has no affinity for the container wall and may be completely surrounded by the liquid.

3.3.3 Effect of surface tension gradients

In order to determine the shape and location of the void in the above case, it is necessary to consider the effect of surface tension gradients. Surface tension gradients can be caused by variations in the chemical composition of the liquid, and surface tension in general decreases linearly with increasing temperature. A surface tension gradient produces a shear stress along the surface of the liquid, causing liquid to move toward the region of higher surface tension. Consequently, the bubble tends to move toward the region of lower surface tension. This phenomenon can be explained in terms of the surface energy as well, since the surface energy is decreased when the surface temperature is higher. Flow resulting from surface tension gradients is called Marangoni flow. The complete vector equation describing Marangoni flow, given in Ref. 10, is

$$\left[P_v - P_\ell - \sigma_{\ell v} \left(\frac{1}{R_1} + \frac{1}{R_2} \right) \right] \bar{n} = - \bar{T} \cdot \bar{n} + \nabla \sigma_{\ell v}$$

where $\bar{n}$ is the unit normal to the surface and $\bar{T}$ is the viscous stress tensor at the surface of the liquid, not including pressure terms. Although the above equation would be very difficult to apply for a general case, it shows that if a surface tension gradient exists there must be motion in the fluid.

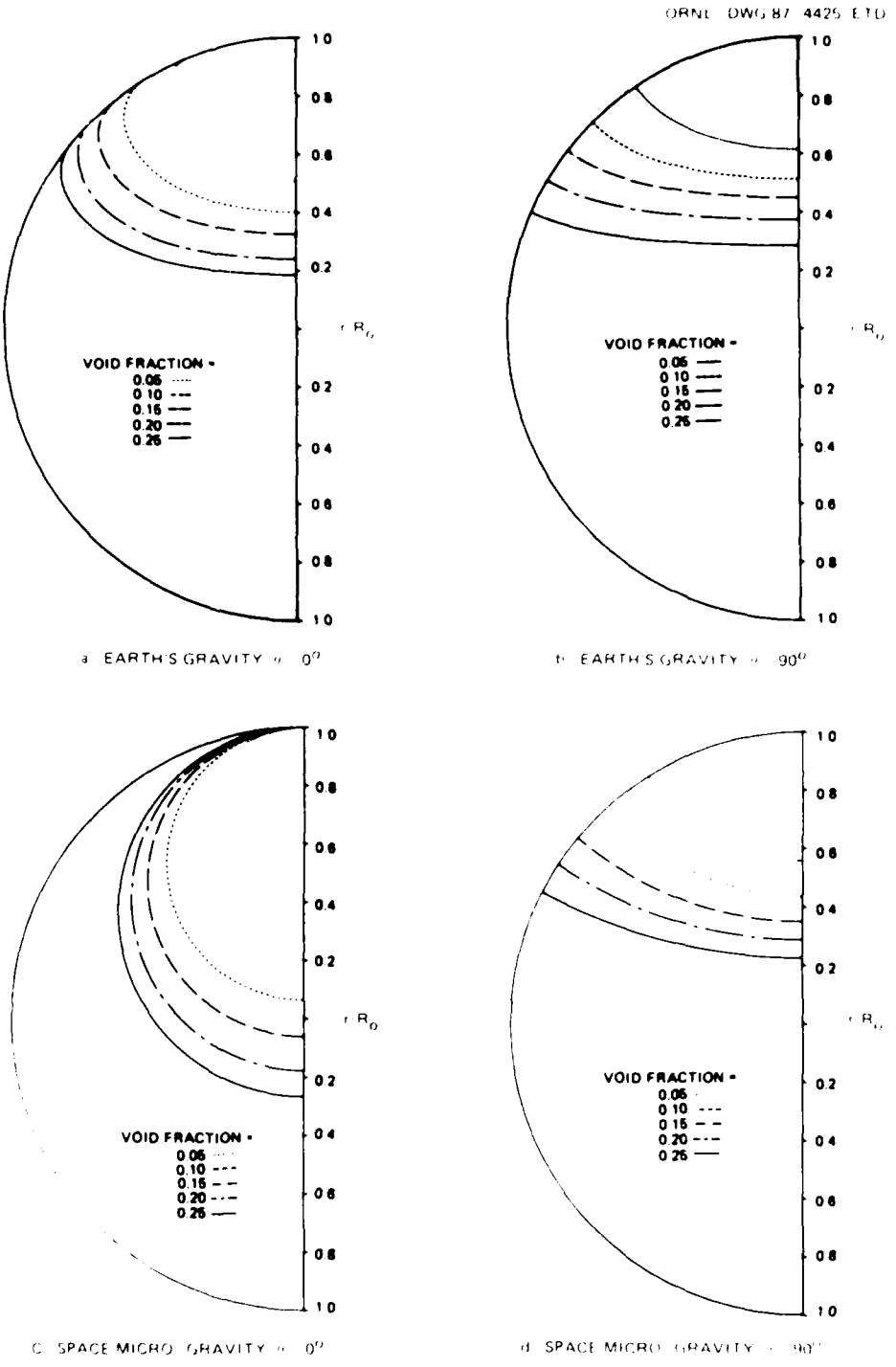

Fig. 3.9. Void shape in a spherical container in earth's gravity and space micro-gravity using the force balance method.
a. Earth's gravity, $\theta = 0°$.
b. Earth's gravity, $\theta = 90°$.
c. Space micro-gravity, $\theta = 0°$.
d. Space micro-gravity, $\theta = 90°$.

The effect of a surface tension gradient on the interface shape can be estimated using Eq. (3.2). In the present case, the surface tension will vary linearly in the z direction, so

$$\sigma_{\ell v} = \sigma_o + \lambda z$$

where σ_o is the surface tension at the origin and $\lambda = \frac{d\sigma}{dz}$. Inserting this into Eq. (3.2) yields

$$(P_v - P_{\ell o} + \rho g z)\, r \frac{dr}{dL} = \frac{d}{dL}\left[(\sigma_o + \lambda z)\, r \frac{dz}{dL}\right]$$

Following the same steps used to develop Eq. (3.6) the resulting differential equation is

$$\frac{d^2z}{dL^2} = \left(\frac{\frac{2}{R_o} + \frac{\rho g z}{\sigma_o}}{1 + \frac{\lambda}{\sigma_o} z} - \frac{1}{r}\frac{dz}{dL}\right)\sqrt{1 - \left(\frac{dz}{dL}\right)^2} - \frac{\frac{\lambda}{\sigma_o}\left(\frac{dz}{dL}\right)^2}{1 + \frac{\lambda}{\sigma_o} z} \qquad (3.7)$$

Eq. (3.7) can be substituted for Eq. (3.6) and used together with Eq. (3.5) to solve for the interface shape. Figure 3.10 shows a comparison of the predicted void shape for a zero g, zero contact angle situation with no surface tension gradient versus the predicted shape with a surface tension gradient corresponding to a 22 K/cm (100°F/in.) temperature increase in the -z direction. As shown in the figure, the effect of the surface tension gradient on the interface shape is very small, resulting in a slight stretching of the bubble along the z-axis.

The effect of the surface tension gradient on the bubble location is much more significant. An estimate of the resultant force on a spherical bubble due to Marangoni flow is developed in Ref. 12 for the case of a uniform surface tension gradient. The shear stress due to the surface tension gradient is integrated over the surface of the bubble, and the resultant force, F_m, in the z direction is found to be

$$F_m = \frac{8}{3}\pi R_o^2 \lambda$$

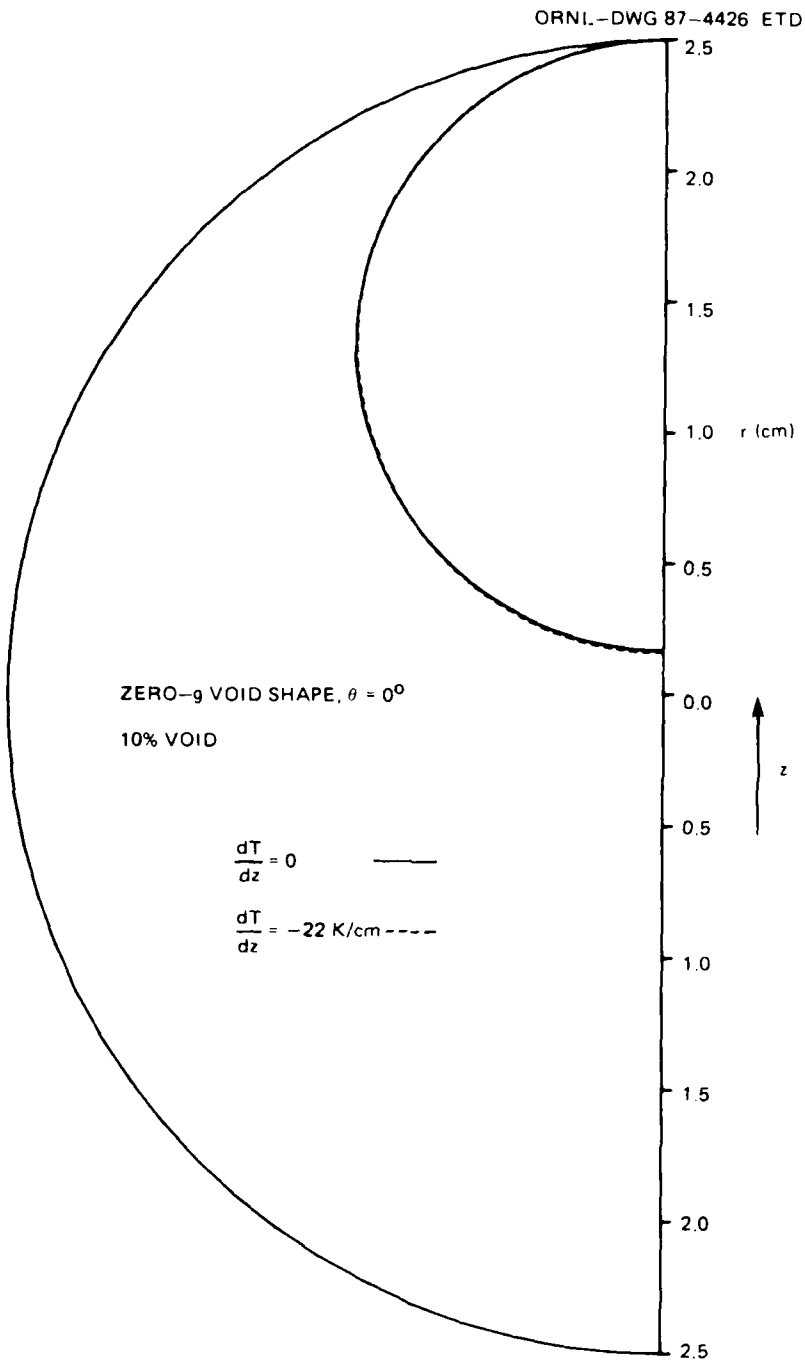

Fig. 3.10. Effect of temperature gradient on zero-g void shape.

where R_o is the bubble radius. The buoyancy force, F_b, is given by

$$F_b = \frac{4}{3} \pi R_o^3 \, (\rho_\ell - \rho_v) \, g$$

Under normal gravity conditions, the Marangoni force is negligible compared to the buoyant force. On the other hand, under orbital conditions where the maximum effective gravity is less than 10^{-6} g, the Marangoni force dominates for $dT/dz \approx 1.82$ K/m (1°F/ft). Assuming the bubble motion is according to Stokes' law, the drag force on the bubble, F_d is

$$F_d = 6\rho\mu \, R_o \, V_\infty$$

and the velocity of a bubble under the influence of a surface tension gradient for a zero-gravity case can be estimated by equating F_d and F_m, giving

$$V_\infty = \frac{4}{9} \frac{R_o \lambda}{\mu}$$

For LiH, $\mu \approx 3.78 \times 10^{-3} \frac{\text{dyne}}{\text{s}\cdot\text{cm}^2}$ $(7.9 \times 10^{-6} \frac{\text{lbf}}{\text{s}\cdot\text{ft}^2})$ and $\frac{d\sigma}{dT} \approx 6.83 \times 10^{-2} \frac{\text{dyne}}{\text{cm-K}}$ $(2.6 \times 10^{-6} \frac{\text{lbf}}{\text{ft}\cdot{}^\circ\text{F}})$. Assuming $R_o \approx 0.30$ cm, the bubble velocity due to a 0.182 K/cm (10°F/ft) temperature gradient is

$$V_\infty = \frac{4}{9} \frac{(0.30 \text{ cm}) \left(6.83 \times 10^{-2} \frac{\text{dyne}}{\text{cm-K}}\right)\left(0.182 \frac{\text{K}}{\text{cm}}\right)}{3.78 \times 10^{-3} \times \frac{\text{dyne}}{\text{s}\cdot\text{cm}^2}}$$

$$= 0.44 \frac{\text{cm}}{\text{s}} \left(1.5 \times 10^{-2} \frac{\text{ft}}{\text{s}}\right)$$

From the analysis it can be concluded that for purposes of heat transfer analysis in the zero-gravity, zero contact angle case, the bubble can be assumed to be located at the hottest point in the liquid.

3.3.4 Boundary layer effects

Boundary layer effects in the thin layer of liquid near the point where the liquid-vapor interface contacts the wall is another aspect of void behavior that must be understood because of the important part this region plays in solidification. In order to simplify the analysis, the system considered for the boundary layer problem will consist of a flat plate with an axisymmetric bubble contacting the plate from below. The contact angle is zero and gravity is 1-g.

To further specify the problem, the bubble volume is set equal to that of a 0.254-cm radius sphere. This system, with bubble shape calculated using Eqs. (3.5) and (3.6), is shown in Fig. 3.11.

In the region near the wall the interface curvature is small, so a relatively simple equation relating the pressure difference across the interface to interface shape can be developed. The derivation follows the method given in Ref. 13. The variation of the free energy, F, of an isothermal capillary system is given by

$$\delta F = (P_v - P_\ell)\, \delta V_\ell + \sigma \delta A_c \tag{3.8}$$

where V_ℓ is the liquid volume and A_c is the capillary area. Consider a surface element on the interface. The area of the undeformed element, dA_o, is given by

$$dA_o = 2\pi r dr$$

and the area of the deformed element, dA, is

$$dA = \sqrt{1 + \left(\frac{dh}{dr}\right)^2}\, dA_o$$

where h is the vertical displacement from the plane z = 0. For small values of h, the above equation can be approximated by

$$dA \approx \left[1 + \frac{1}{2}\left(\frac{dh}{dr}\right)^2\right] \cdot 2\pi r dr \ .$$

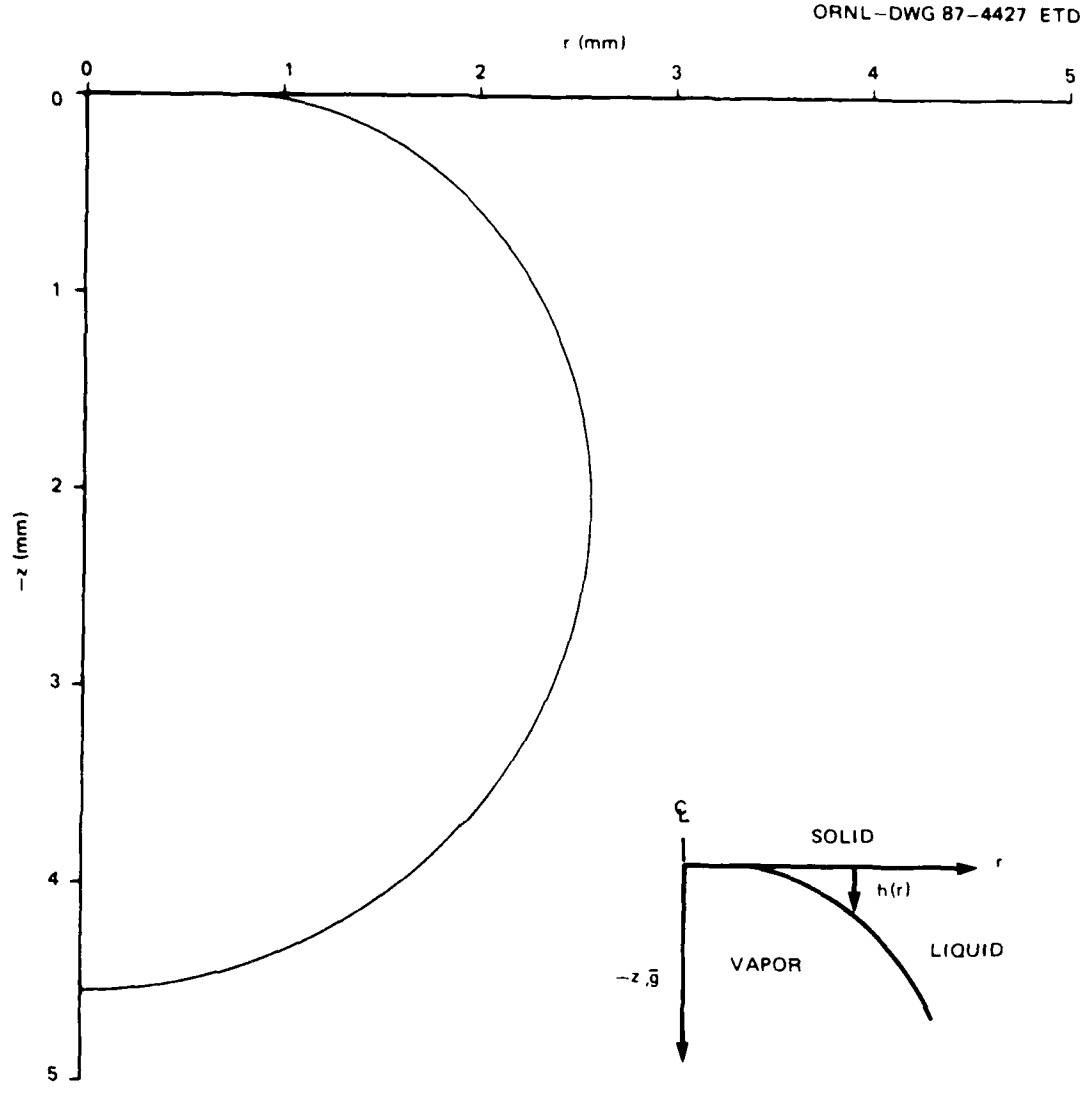

Fig. 3.11. Bubble contacting horizontal surface. 1-g, $\theta = 0°$.

The surface area after deformation is

$$A_c = 2\pi \int_o^R \left[1 + \frac{1}{2}\left(\frac{dh}{dr}\right)^2\right] r\,dr \,,$$

and the variation of the surface area is

$$\delta A_c = -2\pi \int_o^R \left(r\frac{d^2h}{dr^2} + \frac{dh}{dr}\right) \delta h\, dr \,. \qquad (3.9)$$

the change in the liquid volume produced by a small displacement of the surface is

$$\delta V_\ell = 2\pi \int_o^R r\, \delta h\, dr \,. \tag{3.10}$$

Substituting Eqs. (3.9) and (3.10) into Eq. (3.8), the change in the free energy is

$$\delta F = 2\pi \int_o^R \left[(P_v - P_\ell)\, r - \sigma \left(r \frac{d^2h}{dr^2} + \frac{dh}{dr} \right) \right] \delta h\, dr$$

For an equilibrium state $\delta F = 0$. Since δh is arbitrary, it follows that

$$(P_v - P_\ell)\, r - \sigma \left(r \frac{d^2h}{dr^2} + \frac{dh}{dr} \right) = 0$$

or

$$P_v - P_\ell = \sigma \left(\frac{d^2h}{dr^2} + \frac{1}{r} \frac{dh}{dr} \right) \tag{3.11}$$

The approximation implied by Eq. (3.11) can be determined by comparing Eq. (3.11) to Eq. (3.3). Equation 3.3 can be rewritten as

$$\frac{d^2z}{dL^2} = \left(\frac{P_v - P_\ell}{\sigma} - \frac{1}{r} \frac{dz}{dL} \right) \frac{dr}{dL}$$

Near the point of contact with the horizontal plate $dr \to dL$. Making this substitution in the above equation gives

$$\frac{d^2z}{dr^2} = \frac{P_v - P_\ell}{\sigma} - \frac{1}{r} \frac{dz}{dr}$$

which when rearranged is identical to Eq. (3.11). Thus, the approximation made in Eq. (3.11) is that the interface length $dL \approx dr$. If it is further assumed that the difference in hydrostatic head can be neglected across the boundary layer, the pressure difference is constant and Eq. (3.11) can be solved analytically. The resulting equation for h as

a function of r is

$$h = c\left(\frac{r^2 - r_c^2}{4} + \frac{r_c^2}{2}\ln\frac{r_c}{r}\right) \tag{3.12}$$

where $c = \frac{P_v - P_\ell}{\sigma}$, a constant, and r_c is the radius at which the liquid-vapor interface contacts the wall. ($\frac{dh}{dr} = 0$ at $r = r_c$ was used as a boundary condition.) Figure 3.12 shows the small displacement approximation solution, Eq. (3.12), compared to the exact solution (also shown in Fig. 3.11) for the example case. The results plotted in Fig. 3.12 indicate that the small displacement approximation agrees reasonably well with the exact solution for $h < 0.0254$ cm.

In order to determine the effect of solidification in the boundary region, the momentum integral equation can be applied over the boundary layer to derive a differential equation for the boundary layer thickness, h (r). The momentum integral equation for the present case can be

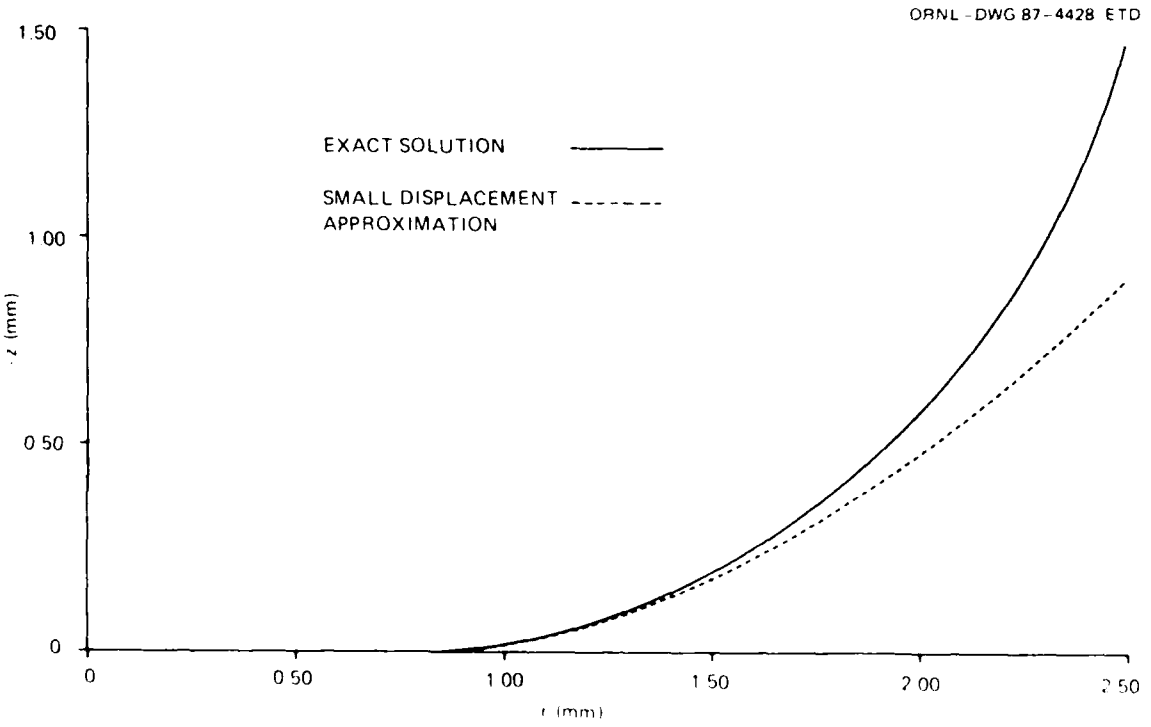

Fig. 3.12. Comparison of small displacement solution with exact solution.

derived by applying the conservation of momentum principle to a control volume as shown in Fig. 3.13 (Ref. 14). Since the flow is axisymmetric, the control volume forms an annular ring about the axis of symmetry. Total radial momentum entering and exiting the control volume is found by integrating over the entire boundary layer thickness. The change in momentum is equated to the sum of forces on the control volume, including viscous stresses and pressure. The resulting equation is

$$2\pi r \int_o^{h(r)} \rho u^2 dz \Big|_{r-\Delta r} - 2\pi r \int_o^{h(r)} \rho u^2 dz \Big|_r$$

$$= 2\pi r \left[h(P\Big|_r - P\Big|_{r-\Delta r}) + \Delta r\,(\tau_h - \tau_o)\right]$$

where u is the radial velocity component, τ_o is the shear stress at the wall and τ_h is the shear stress at the free surface. After rearranging and letting $\Delta r \to 0$, the final form of the momentum integral equation is

$$-\frac{d}{dr}\left[r \int_o^{h(r)} \rho u^2 dz\right] = r\left(h\frac{dP}{dr} + \tau_h - \tau_o\right) \tag{3.13}$$

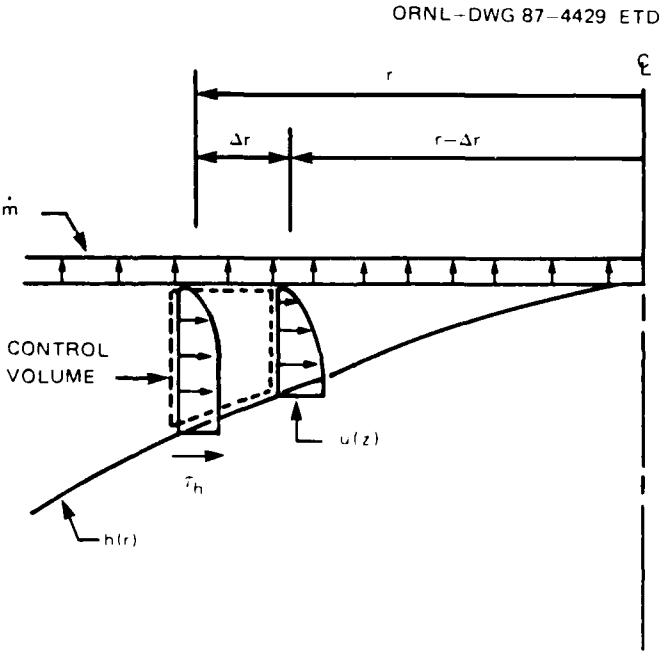

Fig. 3.13. Control volume for momentum integral analysis.

In order to solve Eq. (3.13) a velocity profile must be assumed. For creeping flow along a plate the velocity profile is parabolic, so the velocity profile is assumed to be of the form

$$u = A + B\ \frac{z}{h} + C\ \left(\frac{z}{h}\right)^2$$

where A, B, and C are constants. Boundary conditions on u are

$$u = 0 \quad \text{at} \quad z = 0$$

$$\mu \frac{du}{dz} = \tau_h \quad \text{at} \quad z = h$$

Applying the boundary conditions, the velocity profile can be rewritten

$$u = B\ \left(\frac{z}{h}\right) + \frac{1}{2}\ \left(\frac{\tau_h h}{\mu} - B\right)\ \left(\frac{z}{h}\right)^2$$

The value of the constant B is determined by mass conservation. Solidification is modeled by a constant mass flux per unit area through the wall, $\dot{m}$. Assuming the boundary layer extends to the centerline, as shown in Fig. 3.13, the requirement for conservation of mass can be written

$$\dot{m} \cdot \pi r^2 = 2\pi r \int_o^h \rho u dz$$

Inserting the expression for the velocity profile into the above equation, the value of the constant is found to be

$$B = -\frac{\tau_h h}{2\mu} + \frac{3}{2}\frac{\dot{m} r}{\rho h}$$

and the velocity profile is therefore

$$u = \left(-\frac{\tau_h h}{2\mu} + \frac{3}{2}\frac{\dot{m} r}{\rho h}\right)\ \left(\frac{z}{h}\right) + \frac{1}{2}\ \left(\frac{\tau_h h}{2\mu} - \frac{3}{2}\frac{\dot{m} r}{\rho h}\right)\ \left(\frac{z}{h}\right)^2 \qquad (3.14)$$

The shear stress at the wall can be found by differentiating Eq. 3.14,

giving

$$\tau_o = \frac{\mu}{h}\left(-\frac{\tau_h h}{2\mu} + \frac{3}{2}\frac{\dot{m}r}{\rho h}\right) \tag{3.15}$$

Setting $P_v = 0$ in Eq. (3.11) the pressure in the liquid is given by

$$P = -\sigma\left(\frac{d^2h}{dr^2} + \frac{1}{r}\frac{dh}{dr}\right) \tag{3.16}$$

Eqs. (3.14), (3.15), and (3.16) can now be inserted into Eq. (3.13) and after much algebra, the resulting differential equation for h is

$$\frac{d^3h}{dr^3} = -\frac{1}{r}\frac{d^2h}{dr^2} + \left[\frac{\rho}{\sigma}\left(\frac{6}{15}c_1{}^2 h - \frac{4}{15}c_1c_2\frac{r}{h} - \frac{2}{15}c_2{}^2\frac{r^2}{h^3}\right) + \frac{1}{r^2}\right]\frac{dh}{dr} + \frac{\tau_h}{6h} + \frac{\mu}{\sigma}\left(\frac{c_1}{h} - c_2\frac{r}{h^3}\right) + \frac{\rho}{\sigma}\left(\frac{2}{15}c_1{}^2\frac{h^2}{r} - \frac{8}{15}c_1c_2 + \frac{6}{15}c_2{}^2\frac{r}{h^2}\right) \tag{3.17}$$

where

$$c_1 = \frac{\tau_h}{2\mu}\ , \quad c_2 = \frac{3\dot{m}}{2\rho}$$

Equation (3.17) was solved by the Runge-Kutta method using representative values of $\dot{m}$ and τ_h. It was assumed that τ_h resulted from a surface tension gradient. Boundary conditions were provided by matching with the static solution given by Eq. (3.12) at h = 0.0254 cm. It was found that the deviation from the static solution was negligible for $h > 2.54 \times 10^{-4}$ cm. This result indicates that the static interface shape given by Eq. (3.5) and Eq. (3.6) is approximately correct in the boundary region during solidification.

In summary, the analysis indicates that in microgravity the void will be located at the hottest point in the liquid, and thus in the case of uniform cooling a concentric void will form. An analysis based on capillary hydrostatics appears to model void behavior in an axisymmetric solidification problem with sufficient accuracy. However, it should be

noted that in many instances liquid lithium hydride has been observed to "crawl" up the walls of containers in a manner that seems inconsistent with what the hydrostatic analysis would predict. The theory to explain such behavior is not available at present. Hopefully, an understanding of this behavior will be gained from the experiments to be conducted as part of this program.

3.4 Phase-Change Induced Stress

3.4.1 Spherical shell elastic stress analysis

As indicated in Sect. 3.2, the void is expected to be located in the sphere center following cooldown in a micro-gravity space environment. Then, during heat up, the liquid lithium hydride expands against the shell and solid lithium hydride as shown in Fig. 3.14a. Figure 3.14b shows the results of a thermal analysis performed for a 3.81-cm

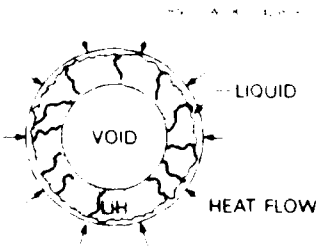

Fig. 3.14a. Heat-up scenario of spherically encapsulated lithium hydride in micro-gravity.

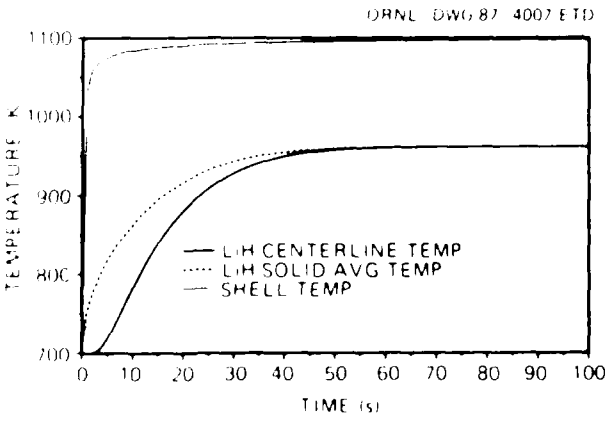

Fig. 3.14b. Spherically encapsulated lithium hydride thermal profile during heat-up, R_o = 1.9 cm.

diam sphere with an initial temperature of 700 K suddenly exposed to liquid metal at 1100 K. The one-dimensional "crush" model described in Sect. 3.2 was used to calculate the shell temperature, average temperature of solid lithium hydride and minimum temperature of solid lithium hydride as a function of time. It can be seen that while the shell reaches the liquid metal temperature very rapidly, much of the solid is at a temperature significantly below the melt point when the lithium hydride adjacent to the shell starts to melt. Since the shell has a limited capacity to expand elastically, there are three possible heatup scenarios:

1. rupture (plastically deform) the encapsulating shell,
2. "break" (deform or collapse) the lithium hydride shell, or
3. liquid leaks through the solid lithium hydride (via cracks) to the void.

If it is assumed that the void forms in the sphere center, and the lithium hydride contains no cracks, then a simple elastic analysis can be performed to determine, in an approximate manner, the required shell thickness to prevent shell rupture. Oliver[15] used elastic analysis to examine the potential use of a silicon carbide shell for lithium hydride containment.

The required shell thickness for shells constructed of 304L stainless steel and molybdenum were determined using an elastic analysis. In this analysis the following assumptions are made:

1. the void forms in the sphere center,
2. the solid lithium hydride forms a thick shell with no cracks,
3. the containment shell is a thin shell, and
4. thermal stresses other than those resulting from phase-change are neglected.

In addition, based on the thermal profiles in Fig. 3.14b, the containment shell is assumed to be isothermal at the peak operating temperature, and the solid lithium hydride is assumed to be isothermal at the minimum storage temperature. These assumptions lead to a conservatively low shell tensile strength and a conservatively high lithium hydride compressive strength.

A force balance on a thin-wall sphere with internal pressure, P, and no external pressure yields:[16]

$$P = 2t\ \sigma_s/r \quad , \tag{3.18}$$

where

t = shell thickness,

r = spherical shell radius, and

σ_s = shell tensile strength.

Timoshenko and Goodier[17] have developed the stress equations for a thick-wall spherical shell. The maximum principal stress occurs in the tangential direction at the inner radius, and is compressive:

$$\sigma_{LiH} = \frac{3\ Pr^3}{(r^3 - a^3)} \quad , \tag{3.19}$$

where

σ_{LiH} = maximum lithium hydride compressive stress,

a = inner radius of the lithium hydride shell, and

r = outer radius of the lithium hydride shell (encapsulating shell radius).

As shown by Oliver,[15] if the sphere is assumed to be completely full at the hottest liquid condition and a central void forms on cooldown, then:

$$(r/a)^3 = (1 - \rho_\ell/\rho_s)^{-1} \quad , \tag{3.20}$$

where

ρ_ℓ, ρ_s are the liquid and solid lithium hydride densities at the hottest temperature and minimum storage temperature, respectively.

Using Eqs. 3.18 through 3.20, it follows that the minimum required encapsulating shell thickness to prevent rupture is given by:

$$t = r/3\ (\sigma_{LiH}/\sigma_s)(\rho_\ell/\rho_s) \quad . \tag{3.21}$$

Pressed lithium hydride ultimate compression strength data are given in Fig. 3.15 (left vertical axis). As shown there is a strong temperature dependence.[18,19] Table 3.3 presents lithium hydride compressive

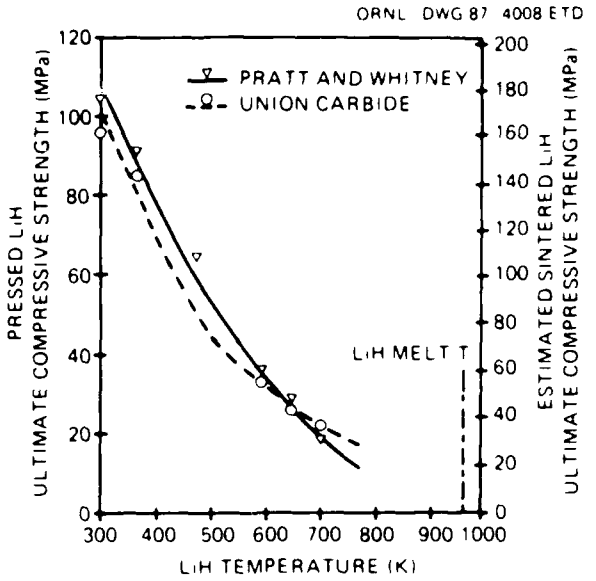

Fig. 3.15. Pressed and estimated cast lithium hydride ultimate compression strength (Refs. 18 and 19).

Table 3.3. Compressive strength of lithium hydride at room temperature (Ref. 20)

Strength		Comments
MPa	psi	
100.7 ± 3.34	14,600 ± 485	Cold pressed
135.6 ± 34.61	19,670 ± 5,020	Cold pressed and sintered, 3 cycles*
110.0 ± 30.13	15,950 ± 4,370	Cold pressed and sintered, 5 cycles*
167.5 ± 6.31	24,300 ± 915	Cold pressed and sintered, 10 cycles*
	(95% confidence interval - room-temperature data)	*Blocks thermal cycled from room temperature to 593°C, specimens machined from sound, uncracked portion of blocks

strength at room temperature for pressed and sintered material.[20] These data indicate that sintering results in large strength gains (about a factor of 1.7 greater for the 10 cycle sample). The sintered data are more likely representative of cast material, thus the data of Fig. 3.15

should probably be scaled upward by this factor. This has been done in the right vertical axis of Fig. 3.15.

At ~1100 K, the yield strength of 304L stainless steel[21] and molybdenum[22] are taken as 69 (estimated) and 255 MPa (10 and 37 ksi), respectively. These properties do not reflect any effects of hydrogen or lithium on strength; these effects are discussed in Sect. 3.6.

A small computer program, SHELL, was written to calculate achievable energy storage densities (i.e., includes shell and lithium hydride) based on the minimum required shell thickness determined as described above. Results are presented in Table 3.4 for encapsulated lithium hydride in spherical shells constructed of 304L stainless steel and molybdenum. Storage densities are based on a 500 s heatup period and use of naturally occurring lithium and are shown for a range of minimum storage temperatures. These results show that the required shell thickness is very large at low minimum storage temperatures, reflecting high lithium hydride compressive strength at low temperatures. Obviously, with thick shells, only a very low energy storage can be achieved. Even for minimum storage temperatures in the 500 to 700 K range, calculated shell thicknesses are much greater than permitted to obtain desired energy storage densities. As the lithium hydride melt temperature is approached and the lithium hydride strength becomes small, more reasonable shell thicknesses and energy storage densities can be achieved. For comparison purposes, energy storage with lithium is shown in Table 3.4 where it is assumed that a shell with negligible mass can be used. In the operating range of interest for the minimum storage temperature (500 to 700 K), the achievable storage density is still well below that desired.

The storage densities presented in Table 3.4 can be compared to those shown in Table 2.1 for Li^6H and Li^7H, alone, to see the penalty paid for the encapsulating shell or using lithium instead of lithium hydride. Based on elastic analysis it appears that a desired shell thickness of ~0.0127 cm (5 mil) cannot be obtained in the temperature range of interest (even for a molybdenum shell, a material with substantial high temperature strength) if lithium hydride forms a monolithic shell.

Table 3.4. Energy storage densities of lithium hydride and shell (stress constrained) and lithium

Minimum store T (K)	Molybdenum shell			Stainless steel shell			Li (no shell) energy storage density (MJ/kg)
	Required shell thickness (cm)	(mils)	Energy storage density (MJ/kg)	Required shell thickness (cm)	(mils)	Energy storage density (MJ/kg)	
300	0.29	116	0.90	1.08	426	0.50	3.7
400	0.23	92	1.0	0.86	338	0.51	3.3
500	0.17	67	1.2	0.62	246	0.57	2.5
600	0.097	38	1.7	0.35	139	0.77	2.1
700	0.069	27	1.9	0.26	101	0.88	1.7
800	0.043	17	2.3	0.15	61	1.1	1.3
900	0.013	5	3.1	0.051	20	2.0	0.84
962	0.0020	0.8	3.6	0.0076	3	3.0	0.56

Note: Sphere diameter = 3.81 cm.

LiH mass = 15.5 grams

Pulse duration = 500 s

Natural lithium

Peak storage temperature = 1100 K

However, it has been observed in tests conducted for this program and others,[23,24a] that cracks form in the lithium hydride during cool-down (see Sect. 4.1). Thus, cracks that penetrate the solid lithium hydride from the containment shell to the void, may provide a path for expanding liquid lithium hydride to reach the centrally located void during heatup. Hence, large hydrostatic forces are avoided, and a thin shell can successfully contain the lithium hydride.

In the event that predictable, "well-behaved" cracks do not form, there are a series of potential design modifications to mitigate the stress problem. These are discussed in the following section.

3.4.2 Potential design modifications to reduce phase-change induced stress

As previously mentioned, the potential for high stresses in the shell resulting from melting lithium hydride when the liquid is not in contact with the void is one of the most serious potential problems in developing a durable energy storage capsule. Design modifications that have been investigated as potential means of reducing phase-change induced stress are listed below:

1. providing internal fins made of the shell material
2. making the container from a non-wetting material or insulating part of the surface, thus causing the void to form at the wall
3. making the container flexible

These potential modifications are discussed below.

Internal fins

Two potential benefits result from providing internal fins that extend from the shell into the solid lithium hydride. First, they keep the lithium hydride from forming a monolithic solid, thus making the solid easier to break (the concept is somewhat analogous to removing ice cubes from an ice tray). In addition, by providing a thermal conduction path to the void, the fins provide a potential channel for liquid to by-pass the solid into the void. The effectiveness of fins as a heat conduction path can be estimated by a constant density finite difference calculation. For the example problem shown in Fig. 3.16, lithium

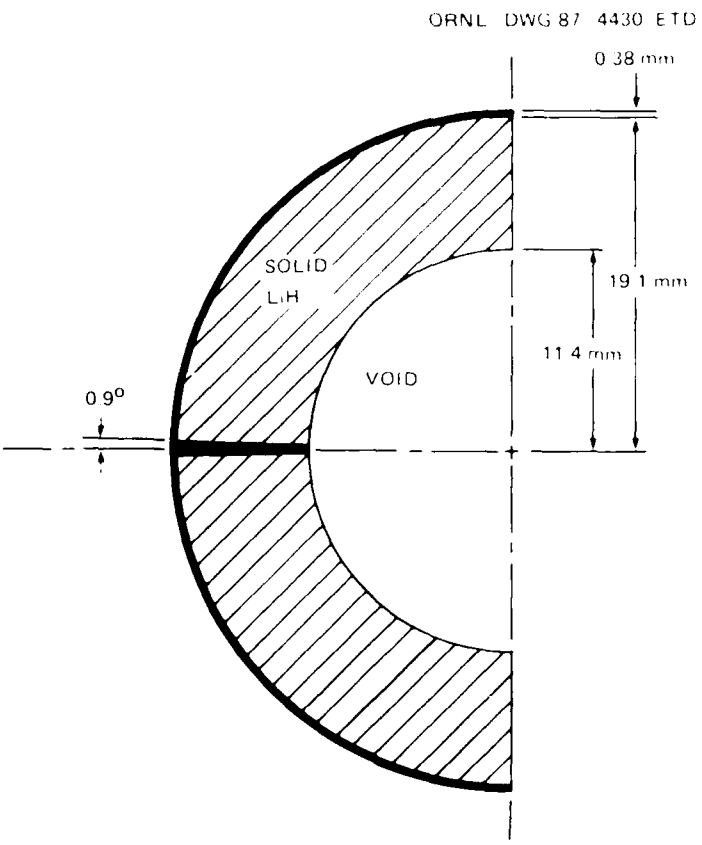

Fig. 3.16. Spherically encapsulated lithium hydride with an internal fin shown in cross-section in left symmetric half.

hydride in a 1.9-cm radius 0.0381-cm (15-mil) thick spherical container is considered. A fin made of the shell material extends completely around the equator of the shell. Figure 3.17 shows the effect of the fin on the temperature distribution in the solid lithium hydride when a sphere with initial temperature of 700 K (800°F) is suddenly exposed to convection from NaK at 1100 K (1520°F). Temperature distributions in the lithium hydride adjacent to the fin and along the centerline (at a 90° angle from the fin) after 1 s of heating are shown for shells made of stainless steel, niobium, and copper. (It should be noted that these temperatures are average values for the finite difference control volumes adjacent to the fin; temperatures at the fin surface are higher.) The effect of the fin is small in the case of stainless steel and niobium. Only copper has a conductivity sufficiently higher than the

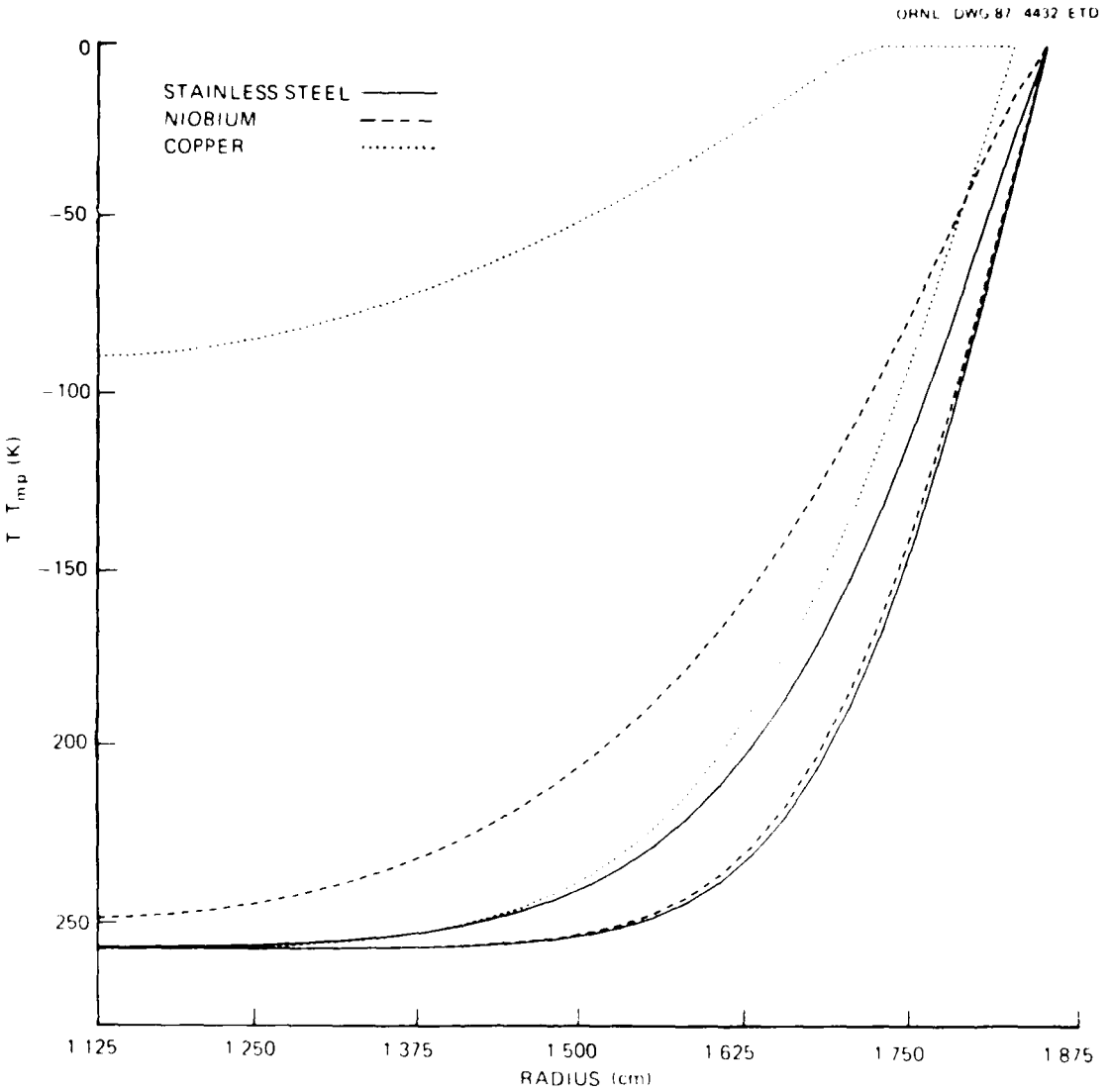

Fig. 3.17. Comparison of temperature distributions in solid lithium hydride adjacent to fin versus 90° away from fin after 1 s. heating.

lithium hydride to provide a conduction path that significantly reduces the mechanical strength of the lithium hydride near the fin. The thermal diffusivities of stainless steel, niobium and copper are, respectively, about 5, 25, and 120 times that of solid lithium hydride. It can be concluded from the above analysis that the shell thermal diffusivity would need to be about two orders of magnitude greater than

that of solid lithium hydride in order for fins to be an effective conduction path. It is not known if potential shell materials with such high thermal diffusivities exist. However, even without a significant heat conduction effect fins would be effective if the solid lithium hydride does not form a strong bond with the shell material and is a technique that merits further investigation.

Void management

In a micro-gravity environment, the liquid-vapor interface is a spherical segment with the radius being determined by the contact angle. For a non-zero contact angle the void would be most likely to form at a wall, since a wall-bound bubble has less surface area per unit volume than a free bubble.[11] Therefore, it would seem that if the container is made of a material which lithium hydride does not wet the void would form at the wall. It is not known at this time if such materials exist and efforts are underway to obtain data on lithium hydride wetting behavior. In any event, a cold container surface exposed to lithium hydride vapor would tend to form a thin surface layer of frozen lithium hydride as a result of condensation. The void would then assume the zero contact angle orientation. Therefore, it does not seem likely that wetting behavior alone can be used to control the void location.

Another possible method for influencing void location would be to reduce the cooling rate on part of the container. This would tend to cause the void to form at the area of slowest cooling and might result in a thinner layer of solid being formed in that area. A full evaluation of this idea will require a heat transfer computer code with an integrated void mechanics model. The influence of insulating a small section of the container surface on the rate of solidification can be demonstrated by a constant density finite difference calculation. For the example problem shown in Fig. 3.18, the surface of a 1.9-cm radius sphere containing liquid lithium hydride is exposed to liquid metal convection except for an area extending 15° from the axis of symmetry on one end, which is insulated. The temperature of the heat transfer fluid decreases gradually with time, simulating rejection of heat to space

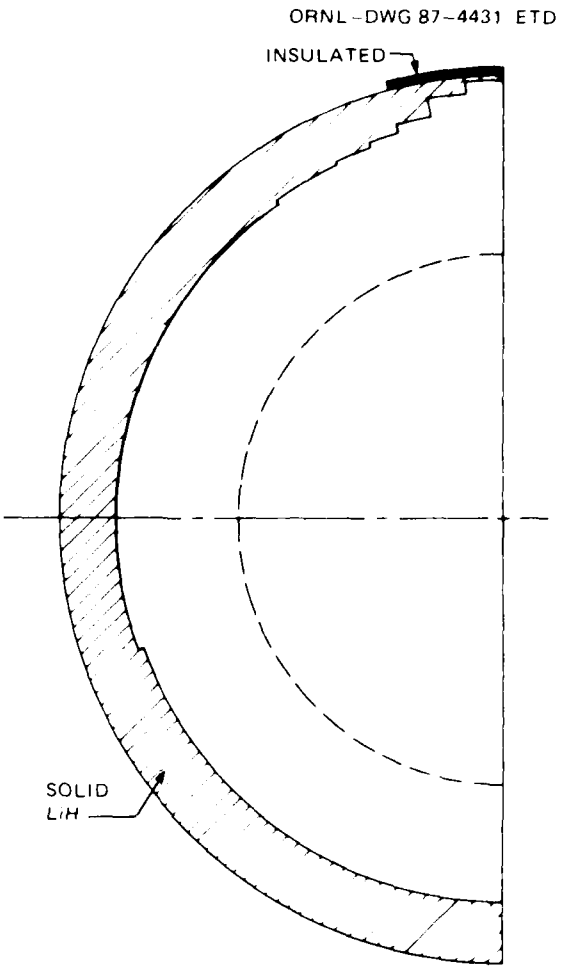

Fig. 3.18. Effect of an insulating surface on the solidification of spherically encapsulated lithium hydride.

through a radiator. As shown in the figure, the thickness of the frozen layer under the insulated area is much less than under the uninsulated surface after cooling for 800 s, and this effect should be increased when the influence of the void is taken into consideration. The dashed line in Fig. 3.18 shows the volume a concentric void would occupy when the lithium hydride is completely solid.

Unfortunately, it will not be possible to evaluate void management schemes experimentally under normal gravity conditions. Experiments in orbit will be needed to confirm the predicted performance.

Flexible containers

Phase-change induced stress in the container walls can be eliminated if the container can be designed to accommodate the excess liquid volume produced by melting via expansion. Estimates of the maximum volume expansion that axially symmetric containers can undergo without damage can be made by considering the container to be a thin elastic membrane. Equations for the deformations of shells of revolution subjected to uniform internal pressure are given in Ref. 25. These equations were solved for a sphere and for oblate spheroids (ellipse rotated about its minor axis) of various eccentricities. The flattest spheroidal shell that can be subjected to internal pressure without buckling has a ratio of semiaxes $\frac{a}{b} = \sqrt{2}$. It was found that for oblate spheroids with $\frac{a}{b} < \sqrt{2}$ a sphere ($\frac{a}{b} = 1$) has the greatest volume expansion for a given wall thickness and maximum allowable stress level. In any case, the maximum volume expansion that can be achieved with a practical shell design is about 1%, which is far less than needed to accommodate the liquid volume expansion.

On the other hand, bellows containers can accommodate rather large volumetric expansions, on the order of 20 to 30%, without incurring damage. Figure 3.19 shows a photograph of a 304L stainless steel seamless bellows with dimensions in the range of interest: length of

ORNL PHOTO 7903-86

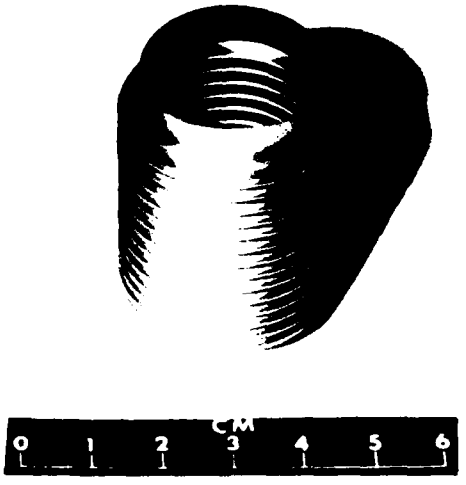

Fig. 3.19. 304L stainless steel bellows container.

3.6 cm, inside diameter of 2.3 cm, outside diameter of 3.2 cm, and a 0.0091-cm (3.6 mil) wall thickness. Optimal bellows dimensions and characteristics have not been determined; however, experimental testing with the bellows in Fig. 3.19 could be performed to determine first-order feasibility.

3.5 Hydrogen Diffusion

Lithium hydride tends to dissociate into lithium and hydrogen gas as it is heated to higher temperatures. To prevent lithium hydride dissociation an overpressure of hydrogen is required. Figure 3.20 presents

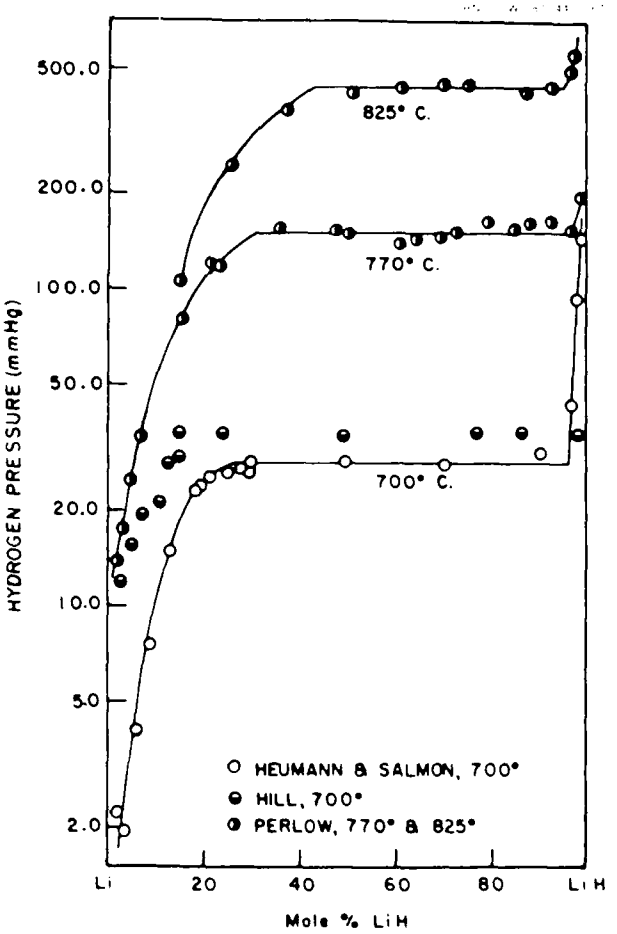

Fig. 3.20. Dissociation pressure isotherms for lithium-lithium hydride system.

Fig. 3.20 source: Messer, Charles, E., "A Survey Report on Lithium Hydride," NYO-9470, October 27, 1960, Fig. 2, p. 19b.

equilibrium dissociation pressure isotherms for a lithium-lithium hydride melt at 700, 770, and 825°C.[24b] The central, flat portion of each of the isotherms is referred to as the plateau region. In this region the equilibrium hydrogen pressure over the melt is insensitive to lithium hydride mole fraction. The plateau dissociation pressures as a function of temperature for the lithium-lithium hydride system are shown in Fig. 3.21.[24b]

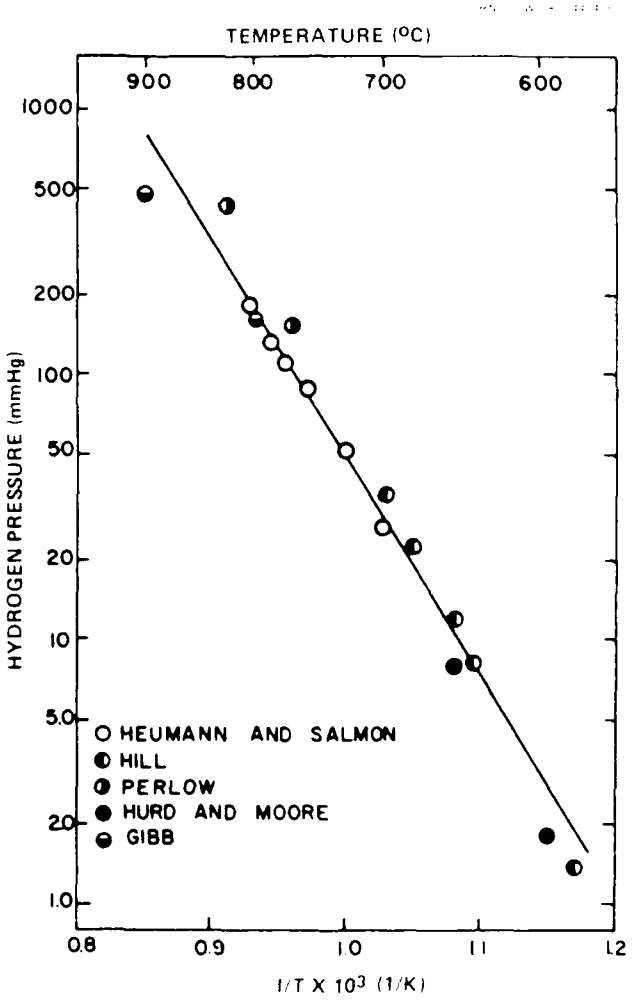

Fig. 3.21. Plateau dissociation pressures for lithium-lithium hydride system.

Fig. 3.21 source: Messer, Charles, E., "A Survey Report on Lithium Hydride," NYO-9470, October 27, 1960, Fig. 1, p. 19a.

As shown in Fig. 3.20, the required hydrogen overpressure to prevent lithium hydride dissociation for high mole fraction lithium hydride systems increases dramatically with increasing lithium hydride mole fraction. For a pure lithium hydride system (LiH mole fraction of 100%), the equilibrium hydrogen pressure would theoretically be infinite.[26] Thus, for a practical system it will be necessary that the encapsulated lithium hydride contain excess lithium to permit a reasonable hydrogen overpressure.

Since lithium hydride tends to dissociate, free hydrogen is present in the encapsulating container and can diffuse through the walls. The loss of hydrogen from the container results in a loss of energy storage density. As described in Ref. 27, hydrogen diffusion (loss) can be calculated using the following equation:

$$H_2 \text{ loss} = \frac{S\ t\ A\ P^{1/2}}{d}, \tag{3.22}$$

where

S = hydrogen permeability of the metal,

t = time,

A = surface area of the encapsulating metal,

P = hydrogen pressure, and

d = shell wall thickness.

Permeabilities of stainless steel and molybdenum, the materials of interest for encapsulating lithium hydride, are shown in Table 3.5 (Ref. 27) along with permeabilities of other materials.[28] As shown, the permeability of clean stainless steel is quite high whereas the permeabilities of oxidized stainless steel and molybdenum are much lower.

Hydrogen loss from lithium hydride encapsulated in molybdenum and clean stainless steel has been calculated for a 25 cycle lifetime.[29] The calculations were performed for a sphere with a diameter of 1.5 in. containing approximately 15.5 grams of LiH (initial mole fraction 99.16%). In addition, calculations assumed the use of naturally occurring isotopic hydride, a thermal storage temperature range of 700 to 1100 K, and a pulse duration and orbit time of 500 and 5880 s, respectively. Phenomenologically, it was assumed that hydrogen diffusion

Table 3.5. Hydrogen permeabilities of selected materials[27,28]

(Pressure = 760 mmHg)

Material	Permeability $\frac{cc(STP)mm}{h\text{-}atm^{1/2}\text{-}cm^2}$
SS 304 - clean	0.45[a]
SS 304 - oxidized	0.012[a]
Molybdenum	0.07[a]
SiC	4.3×10^{-5}[b]
Tungsten	0.0007[b]
Nickel	1.18[b]
Iron	1.47[b]

[a]Temperature near 1100 K.

[b]Temperature near 1000 K.

occurred, as calculated by Eq. 3.22, when liquid lithium hydride or hydrogen gas contacted the container wall, and that on cooldown lithium hydride freezes first and uniformly on the shell surface preventing further hydrogen diffusion (i.e., the lithium hydride freezes over the entire shell surface which ultimately results in a central void). The pressure used in Eq. 3.22 was allowed to vary from cycle to cycle and was assumed to be the hydrogen equilibrium pressure corresponding to the lithium hydride composition at the beginning of each cycle.

Based on the assumptions described above, Table 3.6 presents the calculated loss in energy storage density for molybdenum and clean stainless steel shells 0.00254, 0.0127, and 0.0381 cm (1, 5, and 10 mils) thick. These results indicate that hydrogen loss through a 0.0127 cm (5 mil) clean stainless shell is only 2.9%; however, the loss from a 0.00254 cm (1 mil) clean stainless steel shell is unacceptably high at 11%. On the other hand, molybdenum shells as thin as 0.00254 cm (1 mil) are acceptable with less than 3% loss in storage density. Since the hydrogen permeability of oxidized stainless steel is significantly better than molybdenum values, a 0.00254 cm (1 mil) oxided stainless

Table 3.6. Effect of hydrogen loss on energy storage density

Shell thickness (cm)	(mil)	Material	Energy density (MJ/kg)		Energy density loss (%)
			1st cycle	25th cycle	
0.00254	1	SS-clean	5.468	4.880	11.
0.0127	5	SS-clean	4.493	4.362	2.9
0.0381	15	SS-clean	3.112	3.068	1.4
0.00254	1	Molybdenum	5.379	5.250	2.4
0.0127	5	Molybdenum	4.206	4.173	0.78
0.0381	15	Molybdenum	2.725	2.715	0.37

steel shell would certainly be acceptable. The nominal stainless steel oxide coating would not be stable in this application. Thus, use of a very thin stainless steel shell (~1 mil) would require identification of a stable, low hydrogen permeability coating (possibly some type of refactory ceramic) to apply to the outside shell surface.[28]

3.6 Material Considerations

Successful encapsulation of lithium hydride requires that the shell material be compatible with lithium hydride, lithium and hydrogen since all three materials will be present in the capsule. Compatibility is required over the temperature range ~700 to 1100 K, where most of the exposure is at ~700 K. As mentioned previously, since the system is expected to be cycled 25 times over its lifetime, relatively short life is required at high temperatures (i.e., above the lithium hydride melt temperature).

In addition to being compatible with lithium hydride, lithium, and hydrogen, the shell must be resistant to thermal shock, since the heatup rate is severe. Thus, the shell material must be reasonably ductile with sufficient strength to contain lithium hydride in a thin wall shell

in light of thermal str sses, phase-change induced stress on heatup, and solidification shrinkage forces generated during cooldown. In addition, material costs must be considered as well as the relative ease of fabricating capsules.

The results of lithium hydride compatibility studies have been reported in several sources.[30-35] Figure 3.22 presents results of stress corrosion testing of a group of metals in contact with lithium hydride at 866 K.[30] As shown, only 430 stainless steel survived the full 1000 h without failure; however, the material has relatively low strength at

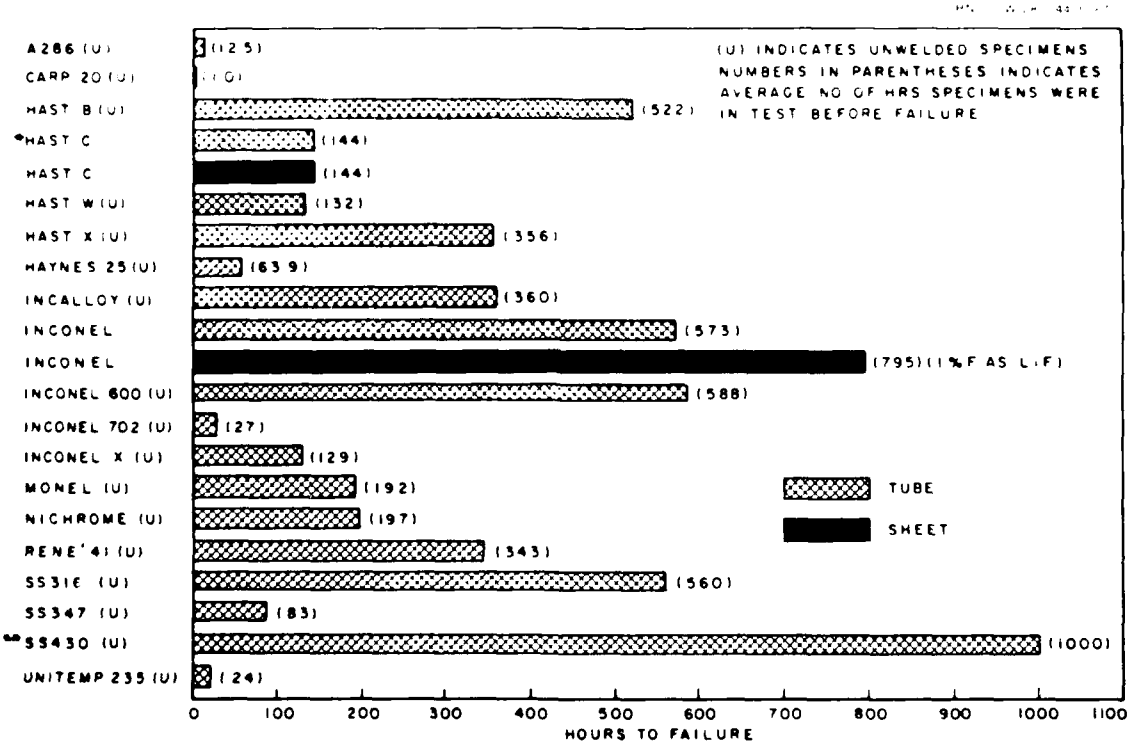

Fig. 3.22. Results of stress corrosion testing of various metals in contact with lithium hydride at 866 K.

Fig. 3.22 source: Hamill, C. W., "Stress Corrosion Testing of Various Alloys," Union Carbide Nuclear Company, in "Lithium Hydride as a Thermal Energy Storage Material," Woods, Frank L., Wannemacher, Marvin P., and Houck, Oscar O., editors, Wright-Patterson Air Force Base, ASD-TR-61-427, May 1962, Fig. 53, p. 79.

high temperature. Hastelloy B, Inconel, Inconel (exposed to lithium hydride with 1% F as LiF), Inconel 600 and 316 stainless steel survived for 500 h or more at 866 K. In tests at 644 K, 316 and 304 (with 1% boron by weight) stainless steels survived the full 1000 h. Stainless steel 316 also survived the full 1000 h in tests at 811 K. It is reported that at 811 K, 301 stainless steel performed the best.

In another study of lithium hydride corrosion,[31] molybdenum, niobium, Hastelloy C, and Hastelloy N samples were tested at 977 K in Hastelloy capsules. Molybdenum was found to be the best material, while niobium disintegrated during testing. It was reported that the niobium disintegration was thought to be due to the bimetallic effect rather than corrosion.

Royer[32] has indicated that pure iron (ARMCO) and low carbon, 300 series stainless steel are suitable lithium hydride containment materials below 1023 K, and that for higher temperatures tungsten and molybdenum might be used.

Smith and Miser[24c] have compiled a data base of lithium hydride (and lithium) compatibility and corrosion information. Based on studies by Messer,[33] it is reported that

> "molten lithium hydride of high purity does not appear to attack Armco iron, 312 or 347 stainless steels at temperatures below 720°C."

Messer does not recommend mild steel or silica for molten lithium hydride, even though others have reported favorable experience with lithium.

Lithium hydride corrosion studies have been conducted at General Electric by Welch[34,35] where austenitic stainless steels, and the 19-9DL alloy (Universial Cyclops alloy austenitic stainless steel type) were investigated. It was found that no significant changes in ultimate tensile strength and 0.2% yield strength occurred in 301, 304, 316, 316ELC, 317, 318, 321, and 347 stainless steels after exposure to lithium hydride at 992 K for periods up to 100 h. Results for the 19-9DL alloy were very similar. Yield strength data are presented in Fig. 3.23 for these metals for no exposure, and 65 and 100 h exposure. In general, the data (Tables 3.7 and 3.8 for common stainless steels)

Table 3.7. Percent elongation of unwelded stainless steels after various exposures to molten lithium hydride at 992±14 K

Type	301 SS		304 SS		316 SS		321 SS	
Test temp / Exposure	Room temp	727 K	Room temp	727 K	Room temp	727 K	Room temp	727 K
Controls	59	43	56	38	44	28	46	28
30 h	55	14	53	14	44	16	41	11
50 h	45	-	49	-	39	-	43	-
65 h	47	-	47	-	41	-	42	-
100 h	46	25	49	28	41	10	39	23

Source: Welch, F. H., "Properties of Lithium Hydride V: Corrosion of Austenitic Stainless Steels in Molten LiH," General Electric Company, APEX-673, August 1961, Appendix 2, p. 67.

Table 3.8. 727 K percent elongation of welded stainless steels after various exposures to molten lithium hydride at 992±14 K

Type specimen					
Type	Hrs exp	B[a]	BR[b]	C[c]	CR[d]
301	0	40.1	33.1	32.9	35.6
	65	30.8	14.7	20.0	25.2
	100	23.7	13.0	22.8	21.5
304	0	34.0	25.8	29.1	30.0
	65	29.2	21.0	22.7	24.7
	100	27.5	21.2	22.8	24.2
316	0	32.3	19.0	28.8	28.8
	65	28.5	18.0	24.0	23.5
	100	19.5	18.0	25.3	20.0
317	0	29.8	22.5	22.8	25.2
	65	25.3	19.5	16.8	14.5
	100	22.5	25.0	18.5	18.0
321	0	28.3	27.0	25.0	28.9
	65	20.3	19.2	16.7	16.7
	100	22.3	21.0	17.7	18.0
347	0	-	-	-	-
	65	26.7	20.0	17.8	18.7
	100	22.7	18.5	18.0	19.5

[a]Weld transverse to length of standard strip specimen; 0.037-inch-thick sheet.

[b]Weld transverse to length of standard strip specimen, ground flush; 0.050-inch-thick sheet.

[c]Weld longitudinal to length of standard strip specimen; 0.037-inch-thick sheet.

[d]Weld longitudinal to length of standard strip specimen, ground flush; 0.050-inch-thick sheet.

Source: Welch, F. H., "Properties of Lithium Hydride V: Corrosion of Austenitic Stainless Steels in Molten LiH," General Electric Company APEX-673, August 1961, Appendix 3, p. 68.

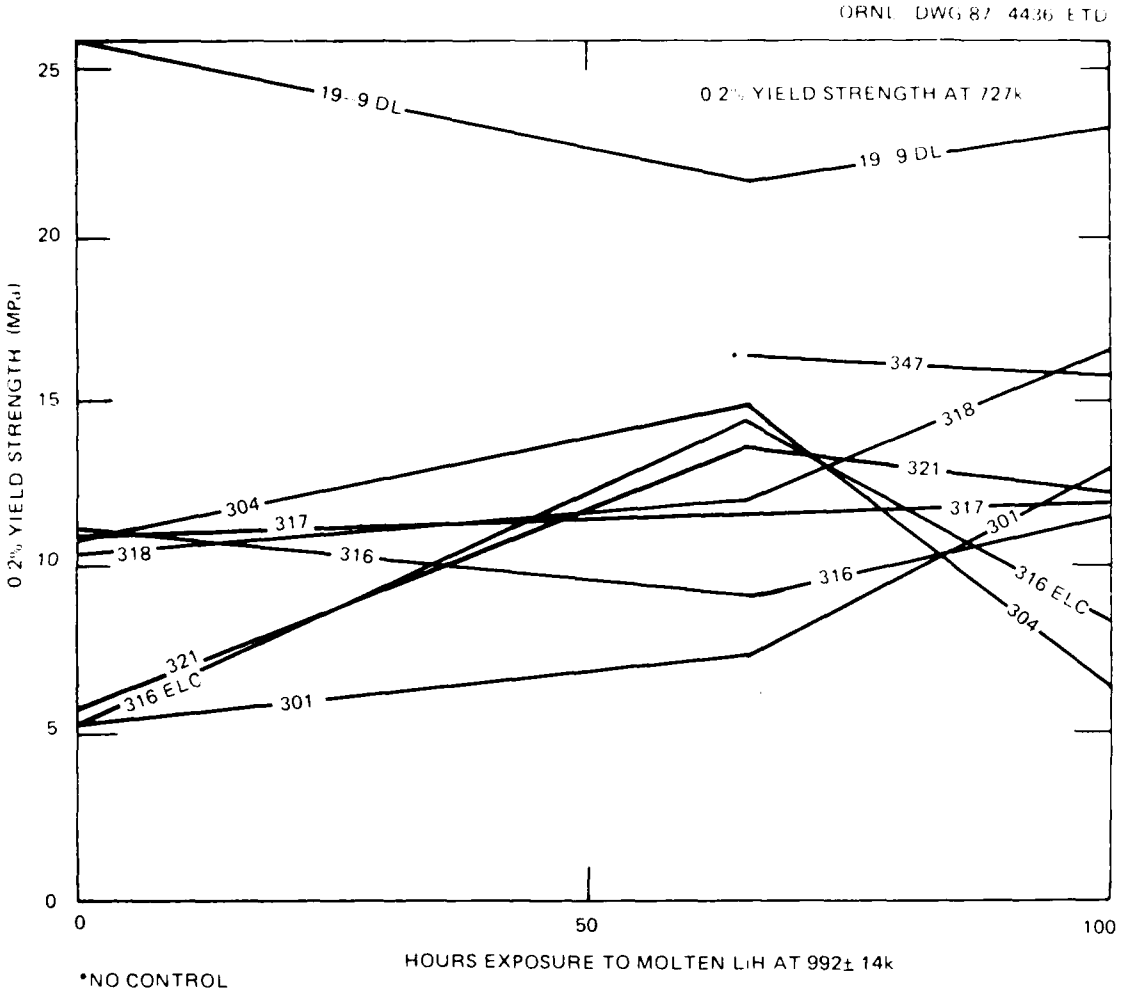

Fig. 3.23. 0.2% yield strength data for stainless steels and 19-9DL alloy exposed to molten lithium hydride at 992 K.

Fig. 3.23 source: Welch, F. H., "Properties of Lithium Hydride II, Lithium Hydride Corrosion Studies: 19-9DL Alloy," General Electric Company, APEX-586, April 10, 1961, Fig. 22, p. 34.

show that percent elongation decreased slightly (<~20%) from control values; however, more significant reductions occurred in 301 and 316 stainless steels tested at 727 K (850°F). In addition, large reductions in percent elongation can be observed after 30 h of exposure to lithium hydride in 301, 304, 316, and 321 stainless steels (Table 3.7). No large reductions in percent elongation were observed for 19-9DL alloy.[35]

Selected stainless steels and 19-9DL alloy were also exposed to heat and hydrogen determine the effect of hydrogen on mechanical properties. For these metals, the hydrogen exposure caused mechanical property changes of the same magnitude to occur. Thus, Welch concluded that exposure to molten lithium hydride does not have a significant effect on the ultimate tensile strength, and percent elongation of the metals tested over the time periods and temperatures examined.

For the 300 series stainless steels Welch reports,[34a]

> "Metallographic examination of unwelded and welded specimens of the eight alloys showed that exposure to molten lithium hydride up to 100 h at 1325°F or 65 h at 1425°F did not produce any significant attack (0.001 in. or less)."

At 1047 K (1425°F), corrosive attack became significant for 100-h exposure to molten lithium hydride for 304, 317, and 321 stainless steels (0.005-0.01 cm), and showed a slight increase in 316, 316ELC, and 347 stainless steel. 301 stainless steel was essentially unaffected at 1047 K (1425°F). For the 19-9DL alloy, Welch[36] found the lithium hydride attack to be slight with no definite indication of intergranular attack. Stainless steel and the 19-9DL alloy welds showed a slightly greater corrosive attack than the bare metal.

Welch,[35] based on his studies of the effects of molten lithium hydride on 300 series stainless steels and 19-9DL alloy,[34,35] concluded that the 19-9DL alloy was definitely superior to the others tested.

Several studies have examined the compatibility of various materials with lithium.[36-38] Figure 3.24 presents a summary of resistance of various materials to lithium.[36] As indicated, pure iron, ferritic-chromium stainless steel, columbium, tantalum, and molybdenum show good resistance to lithium up to at least 800°C (application peak design temperature is 1100 K or 827°C). However, since the system only operates for relatively short times at peak temperatures, it is probably reasonable to consider austenitic Cr-Ni stainless steel as being acceptable.

Reference 37 summarizes the results of numerous corrosion studies of refractory metals and alloys, among other materials. Studies indicate that Mo-30 W, Mo-0.5 Ti, and Mo-0.5 Ti-0.08 Zr resist static

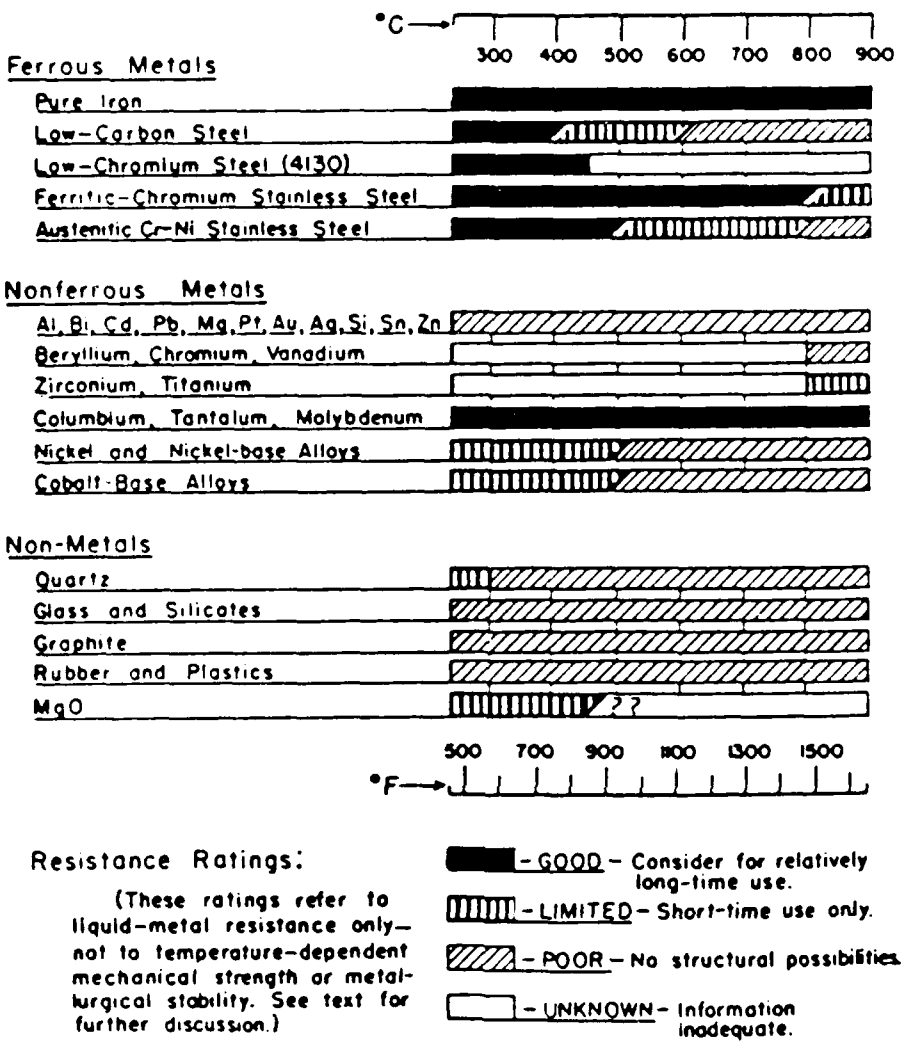

Fig. 3.24. Resistance of materials to liquid lithium.

Fig. 3.24 source: Atomic Energy Commission, Dept. of Navy, Liquid Metals Handbook, June, 1952, Chart III, p. 159.

lithium attack at 1200°C for 8 to 9 days, and that a TZM lithium heat pipe functioned without incident for over 9400 h at 1500°C. Studies also indicate tungsten and rhenium are resistant to corrosive attack for 100 h at 1538°C.

Resistances of some non-metals are shown in Fig. 3.24, and indicate "no structural possibilities" (or "unknown" in the case of MgO) for temperatures of interest. Corrosion resistance of various ceramics to

static lithium at 1089 K for 100 h is provided in Fig. 3.25 (Ref. 38). Of those studied, TiC, ZrC, and Cr_3C_2 show good lithium resistance.

The effect of hydrogen on the mechanical properties of many of the refractory metals prevents their use. Niobium suffers severe hydrogen embrittlement when exposed to hydrogen gas in the 500 to 600°C (773 to 873 K) range.[39] The material loses its ductility, and about half of its strength. Hydrogen also adversely affects the mechanical properties of tantalum,[40] titanium,[41,42] and zirconium.[43] On the other hand, rhenium has been reported[44] to behave well in hydrogen at elevated temperatures while tungsten is reported[45] as not reacting with hydrogen.

Westphal and Worzala[46] describe two forms of hydrogen damage in steels: hydrogen attack and hydrogen embrittlement. Hydrogen attack is distinguished from hydrogen embrittlement in that in the former, a methane reaction occurs, but not in the latter. In addition, hydrogen embrittlement is reversible and occurs below 473 K, while hydrogen attack is usually considered irreversible and occurs only above 473 K. In a summary paper by Morris[47] it is reported that for high temperature conditions (greater than 866 K), steels containing greater than 12% chromium, and the austenitic stainless steels are resistant to hydrogen attack in all known applications.

As described previously, Welch[34,35] studied the effects of heated hydrogen on the mechanical properties of selected stainless steels and 19-9DL alloy. For 316 and 318 stainless steels, and 19-9DL alloy, Welch concluded that the losses in ultimate tensile strength, yield strength, and percent elongation were due primarily to hydrogen. Welch, in arriving at this conclusion, was aware of reported stability of high chromium content austenitic steels to hydrogen.[35] It is interesting to note that 301 and 316 stainless steels (which, as indicated previously, suffered more significant reductions in percent elongation following exposure to molten lithium hydride) have less chromium content (16–18%) than the other common steels tested (SS 304 and 317 and 19-9DL alloy, 18—20%; and SS 321 and 347, 17—19%).

Based on the compatibility of shell materials with lithium hydride, lithium, and hydrogen in the temperature range of interest, many potential materials considered here can be eliminated for possible use. Most

ORNL DWG 67-4438 ETD

MATERIAL	THEORETICAL DENSITY (%)	CORROSION RESISTANCE TO LITHIUM			
		BAD	POOR	FAIR	GOOD
B_4C	80-90	■			
SiC		■			
TiC	97.4	■	■	■	
ZrC	100	■	■	■	
Cr_3C_2	98.7	■	■	■	
BN	60-98	■			
TiN		■			
Si_3N_4	67.7	■			
MgO*	100	■			
Al_2O_3*	100	◤			
ZrO_2*		■			
$MgAl_2O_4$*	100	◤			

SIGNIFICANCE OF SHORTEST BARS:
■ PIECES OF THE TESTED SPECIMEN REMAINED.
◤ THERE WAS NO VISIBLE TRACE OF THE TESTED SPECIMEN.

*A SPECIMEN FROM A SINGLE CRYSTAL.
*CaO-STABILIZED.

TYPE OF DATA	ARBITRARY CORROSION RATINGS AND DATA RANGE BASES			
	BAD	POOR	FAIR	GOOD
DEPTH OF ATTACK, mils*	3	2	1	0
WEIGHT CHANGE (%)**	6	4	2	0
DIMENSIONAL CHANGE (%)	3	2	1	0

*MEASURED IN METALLOGRAPHIC EXAMINATIONS.
**DETERMINED BY DIRECT MEASUREMENT AND/OR BY CALCULATIONS BASED ON THE MATERIAL(S) FOUND IN THE TEST MEDIUM BY CHEMICAL ANALYSES.

Fig. 3.25. Corrosion resistance of various ceramics in static lithium for 100 h at 1089 K.

Fig. 3.25 source: Cook, W. H., "Corrosion Resistance of Various Ceramics and Cermets to Liquid Metals," Oak Ridge National Laboratory, ORNL-2391, May 31, 1960, Fig. 10, p. 14.

of the non-metals can be eliminated due to incompatibility with lithium hydride and/or lithium. Exceptions include ZrC, TiC, and Cr_3C_2. With the exception of the refractory metals, nonferrous metals are not compatible with lithium. And, of the refractory metals, niobium, zirconium, titanium, and tantalum suffer from hydrogen embrittlement. Of the ferrous metals, pure iron, ferritic-chromium stainless steels, and austenitic Cr-Ni stainless steels offer either good or limited lithium combatibility at temperatures at least as high as 800°C.

In addition to material compatibility, other material considerations applicable to the encapsulating application include:

1. strength,
2. density,
3. ductility,
4. thermal shock resistance, and
5. material and fabrication cost.

Table 3.9 presents the yield strength, density, and ductility (total elongation) of materials (data from Refs. 21, 22, 48—53) which, based on material compatibility, could be considered for use. As indicated, pure iron and ferritic-Cr stainless steels have low strength at high temperature. Unlike SiC, TiC (and also ZrC and Cr_3C_2) do not have good thermal shock resistance.[52] Tungsten (and rhenium) have high densities. 304L stainless steel has moderate high temperature strength and density and good ductility. Similarly, molybdenum has moderate density, and good ductility (however, molybdenum has a high brittle-to-ductile transition temperature, ~100°C), but also possess high strength at elevated temperatures.

It is felt that constructing and sealing a shell using one of the carbide ceramics would be quite difficult.[54] Fabricating shells of tungsten or rhenium would be more difficult than molybdenum, which is a lower cost refactory metal which can be spun or hydroformed.[55] Obviously, the material and fabrication costs of stainless steels are much less.

Based on the data presented, it is concluded that molybdenum or one of the austenitic stainless steels would provide the best possible

Table 3.9. Selected mechanical properties of potential shell materials

Material	Yield strength[d] (MPa)	Density[e] (g/cm^3)	Total elongation[f] (%)
Pure iron[48]	~39	7.87	26.5-53.5
[a]SS-446[21,49a,50]	~29	7.6	25.[h]
[b]SS-304L[21,49b,51]	~69	8.03	35.-60.
[c]TiC[52]	296[g]	4.92	brittle
Molybdenum[22]	255	10.2	24.-26.
Tungsten[22,53]	~110	19.3	40.-60.[i]

[a]Representative of ferritic-Cr stainless steels.

[b]Representative of austenitic stainless steels.

[c]Representative of ZrC and Cr_3C_2.

[d]Yield strength at ~1100 K.

[e]Density at ~ room temperature.

[f]Property variation over temperature range of interest.

[g]Tensile strength at 1100 K.

[h]Nominal value.

[i]Above 300°C.

containment shell. Based on the Y-12 Plant successful experience with 304L stainless steel, its use is selected for testing over the other stainless steels. Although molybdenum is more difficult to fabricate and material costs are much higher, it appears to be a better material than stainless steel in terms of strength and compatibility with lithium hydride. The compatibility of a stainless steel shell with lithium hydride may be improved with a thin liner of pure iron on the inside and outside shell surfaces.

4. EXPERIMENTAL INVESTIGATION

A series of experiments which would address the feasibility of utilizing encapsulated lithium hydride as an energy storage medium have been identified. The series of tests can be subdivided into five groups:

1. initial scoping experiments,
2. thin-shell stress tests,
3. thermal characterization tests,
4. hydrogen diffusion tests, and
5. shell/lithium hydride compatibility tests.

To date, initial scoping experiments have been performed and are discussed in Sect. 4.1. The other four groups of tests, which address specific issues discussed previously, have not been conducted. It appears that it would be more efficient to conduct groups of experiments, each aimed at a specific issue, rather than try to design a "single" experiment to answer all questions.

Section 4.2 contains a discussion of experimental and analytical work performed to investigate the feasibility of using a high heat rate graphite induction furnace to simulate the rapid heatup required in the actual storage system ("real system"). Rapid heatup of capsules in the thin-shell stress tests is critical and is highly desirable in the thermal characterization tests.

4.1 Scoping Experiments

With the assistance of Y-12 plant personnel, initial scoping experiments were performed using cylindrical cans containing lithium hydride. The purposes of these experiments were to perform preliminary scoping tests of cylindrical containments and to gain experience in the thermal cycling of encapsulated lithium hydride. The tests provided insights into container (and weld) survivability during phase-change and the location and shape of the void formed during lithium hydride solidification. In addition, experience was gained in the areas of hydrogen gas

evolution due to impurities and lithium hydride decomposition, furnace equipment functioning, and the thermal response of furnace and sample.

The experimental setup is pictured in Fig. 4.1. As shown, the can fill-tube is attached through flexible tubing to a pressure gage, vacuum pump, and argon purge line. The lithium hydride container was placed in a stainless steel beaker and packed with MgO. A thermocouple was located adjacent to the outside of the lithium hydride container about halfway up the side. The beaker was placed inside the resistance heated furnace (900 W capacity) and the top of the furnace was covered with insulation. The cans were filled with preoutgassed lithium hydride powder (chemical analysis of similar samples indicated 99.16 mole % LiH). Following filling of the containers, the lid with fill-tube was welded to the can.

Using the setup described above, three tests were performed. Two tests used cylindrical cans 2.54-cm long, 3.81 cm in diameter, and 0.089-cm (35-mil) thick, filled with about 14 grams of lithium hydride. Based on density considerations, the container was ~88% full at the maximum experimental temperature (~1050 K). In the first test (test C-1), the can was cycled once from room temperature to ~1000 K and then back to room temperature. In the second test (test C-2), the can was cycled a total of four times over a two day period with two cycles performed each day. The second cycle performed each day was initiated from about 25 K below the melt point rather than after return to room temperature. However, based on thermal analysis and thermocouple response, it is fairly certain that complete freezing occurred after completing the first cycle. Heating from about 25 K below the melt point to about 50 K above the melt point occurred over 1 h; the cooling process was also 1 h in duration. The time-temperature and time-power curves for both tests are shown in Figs. 4.2a and 4.2b. The furnace power was controlled (manually) to provide heatup from ~25 K below the melt point to 25 K above the melt point; a similar strategy was employed on cooldown.

Since the powder was preoutgassed, it was anticipated that only a small amount of gas would evolve on heatup to the melt temperature. In all tests, this was observed. In heating through and above the phase-change temperature, the pressure rose in tests C-1 and C-2 to a maximum

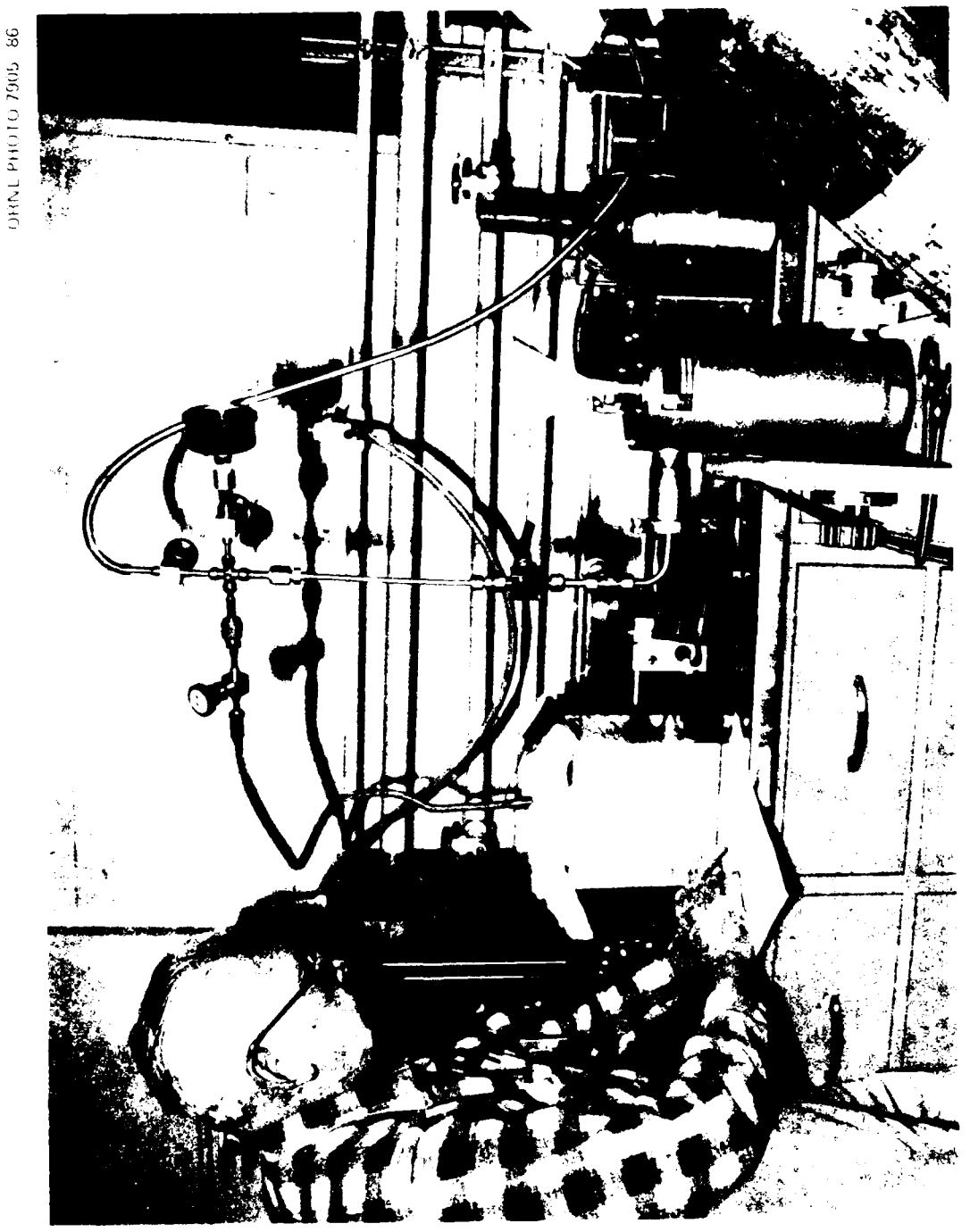

Fig. 4.1. Experimental setup for thermal cycling tests of cylindrically encapsulated lithium hydride.

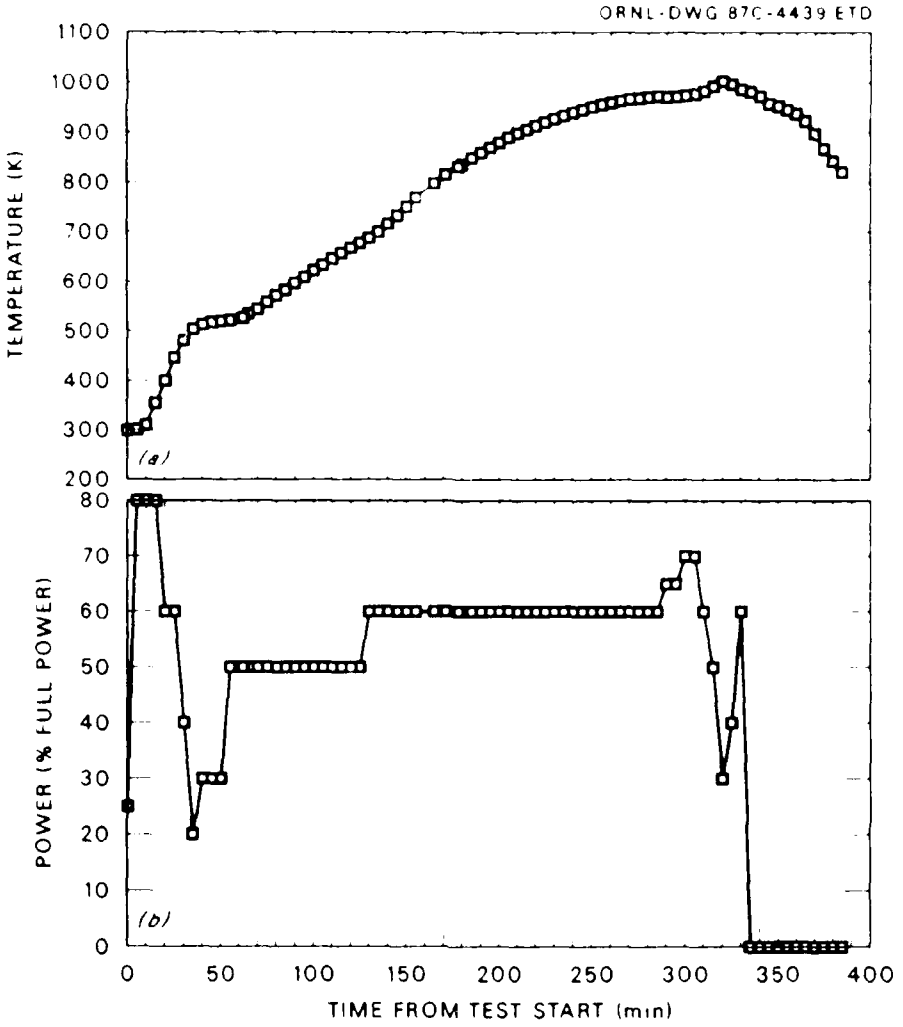

Fig. 4.2a. Temperature and power histories for test C-1.

of about 100 mmHg. Figure 4.3 presents two calculated equilibrium hydrogen pressure curves for the test C-2 container as a function of temperature (results for test C-1 are essentially the same).[26] The upper-most curve was calculated using an estimated container plus fill-tube free volume of 50 cm^3 and initial material composition of 99.16 mole % lithium hydride. Plateau dissociation pressures for the lithium-lithium hydride system are shown in the lower curve. Since the maximum temperature achieved in the test was 1034 K, one would expect to measure a much higher pressure with high mole fraction lithium hydride. However, post-test examination revealed that the lithium hydride had

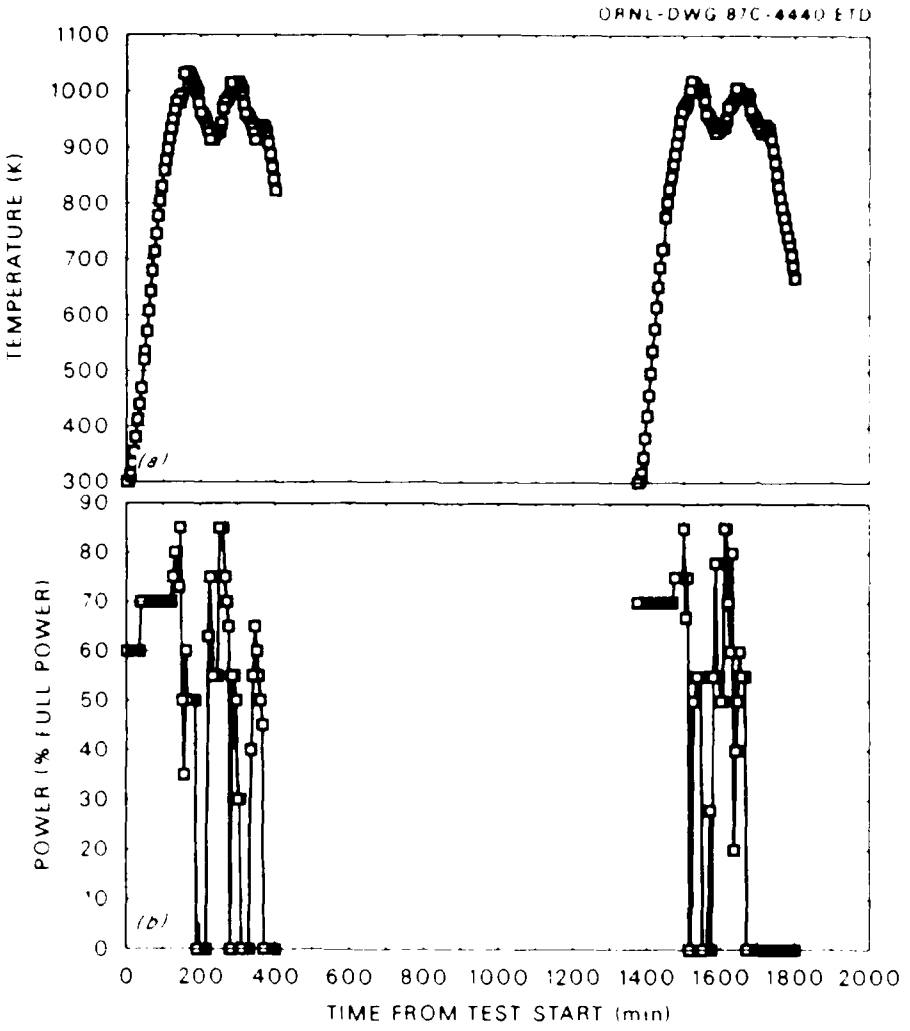

Fig. 4.2b. Temperature and power histories for test C-2.

"crawled" up the fill-tube and possibly isolated the lithium hydride in the can from pressure measurement. In test C-2, the lithium hydride had "crawled" through the fill-tube and entered the flexible tubing (lithium hydride only partially filled the fill-tube in test C-1). The mechanism for this behavior is not currently understood, but is being investigated.

Post-test examination of the cycled test C-1 and C-2 canisters showed that a single, continuous void formed near the top of the can in both tests. As shown in Fig. 4.4, the void in the test C-1 can was not

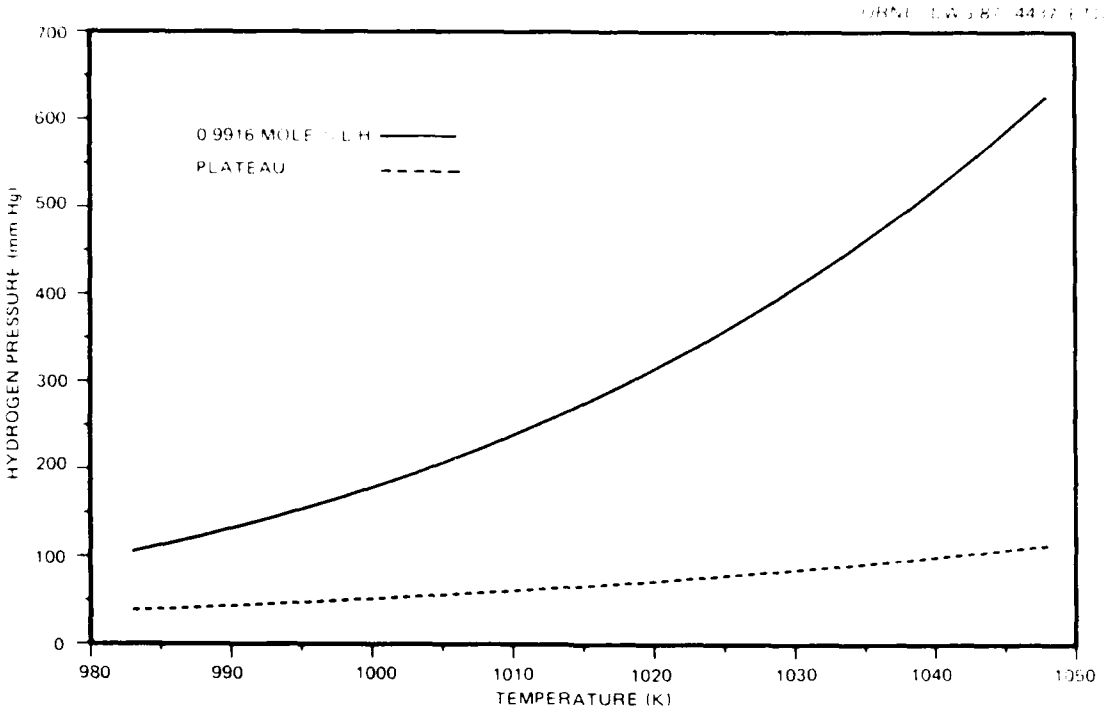

Fig. 4.3. Calculated equilibrium hydrogen pressure curves for test C-2.

ORNL PHOTO 7902-86

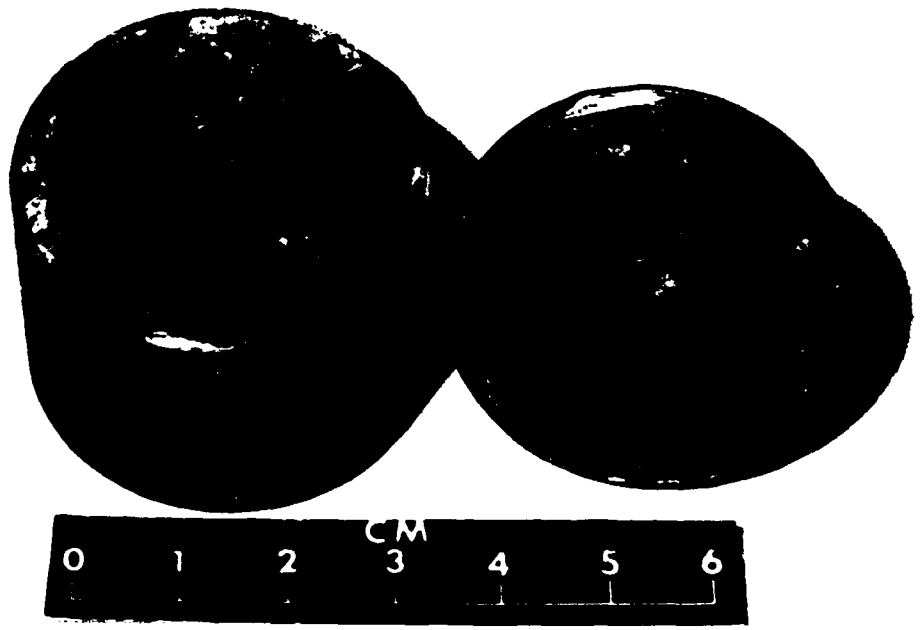

Fig. 4.4. Void and lithium hydride cracks formed upon freezing in test C1.

symmetrically formed, suggesting that the can was not level during testing and/or that there existed some nonuniform heating/cooling. Radiographs of the test C-2 can show a similar void shape and location.

Comparison of measurements of container diameter before and after C-1 and C-2 showed no measurable change. However, comparison of before and after top-to-top measurements for test C-2 showed that the top-to-top distance had decreased about 0.05 cm (20 mil) (similar data was not collected for test C-1). Since the top and bottom of the can were flat, these surfaces could easily be deformed, possibly by "gripping" or shrinkage forces generated by the lithium hydride during cooldown. As a result of heating in an air atmosphere, cans in both tests oxidized. Based on visual observation, the welds performed without failure.

Test C-3 was performed with a cylindrical can with the same dimensions as the first two tests, except that the wall thickness was 25 mils. The primary objective of the test was to examine void behavior in a "hot-full" container (i.e., the can was filled with 16 grams of lithium hydride to produce a can almost completely full of liquid at the highest temperature achieved). Experience with lithium fluoride at TRW[56] and ORNL[57] indicates that in some cases voids tend to be located near the center of the container following solidification even in the presence of Earth's gravity. Central voids occurred when the containers were both "hot-full," and cooled from the entire enclosing surface. TRW used rectangularly shaped test modules (Fig. 4.5) to study lithium fluoride phase-change behavior. Figure 4.6a shows a cross-sectional view of a TRW test module following thermal cycling of lithium fluoride. Since the top container surface had a significant downward dip (caused by machining operations in making thermocouple well grooves), the lithium fluoride in the molten state contacted the top surface. Then, as the test module cooled, lithium fluoride solidified on the container surfaces leaving a "centrally" located void. Figure 4.6b shows a contrasting situation where lithium fluoride did not contact the top plate surface in the molten. In this case, even in the presence of fins, the void tended to form at the top of the container.

Heat storage tubes for the NASA Brayton-cycle heat receiver were filled with lithium fluoride at ORNL. A photograph of a tube is shown

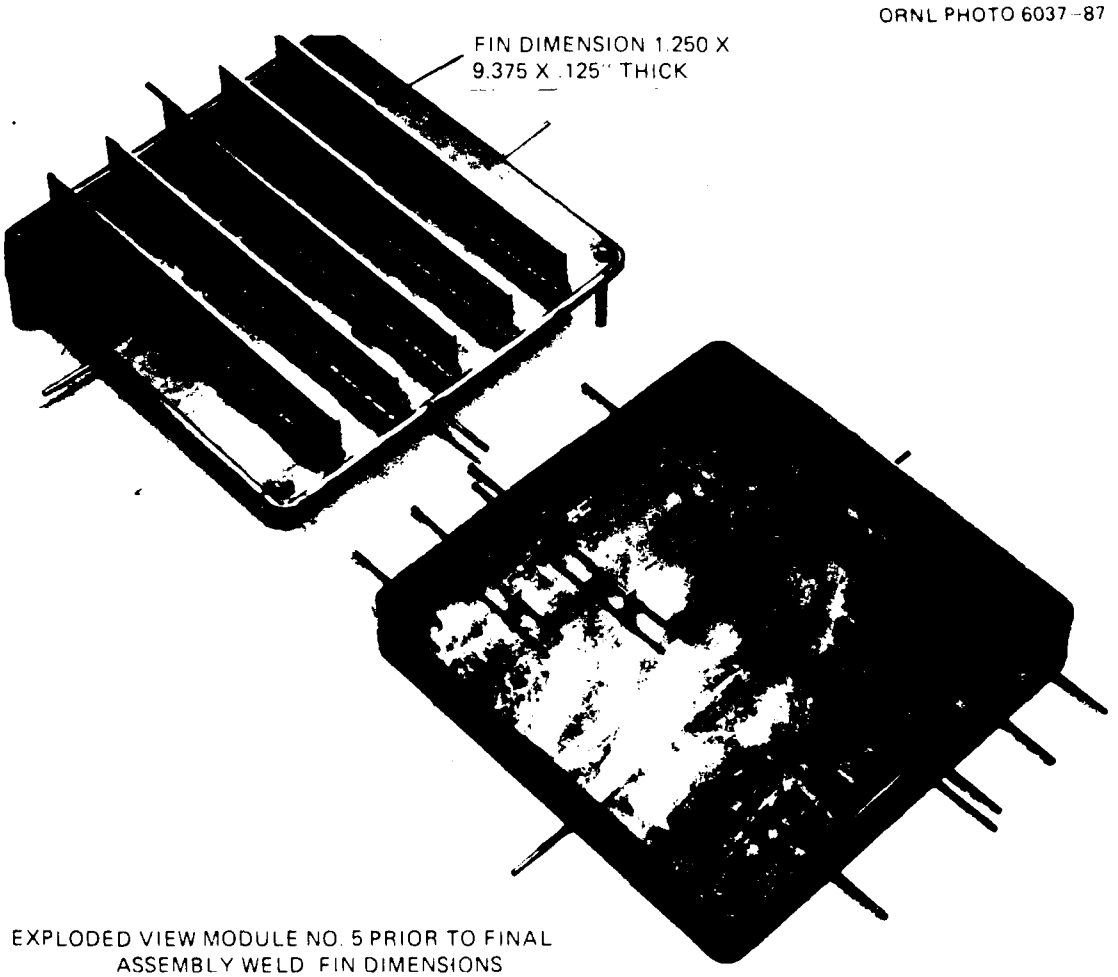

Fig. 4.5. TRW 316 stainless steel heat input test module No. 5.

Fig. 4.5 source: TRW Power Systems Department, "Brayton Cycle Cavity Receiver Design Study," TRW Equipment Laboratories, NASA CR-54752 ER-6497, Nov. 22, 1965, Fig. 24, p. 56.

in Fig. 4.7. Following liquid filling of lithium fluoride in the convoluted bellows, the assembly was cooled on the external surfaces and on the interior tube surface. The resulting void shape can be observed in radiographs of Fig. 4.8, where it is seen that a "centrally" located void has formed.

Results for a "hot-full" can of lithium hydride were not obtained in test C-3 due to a can leak. The leak apparently occurred at a weld point(s) where the top of the can was welded to the lid. This failure

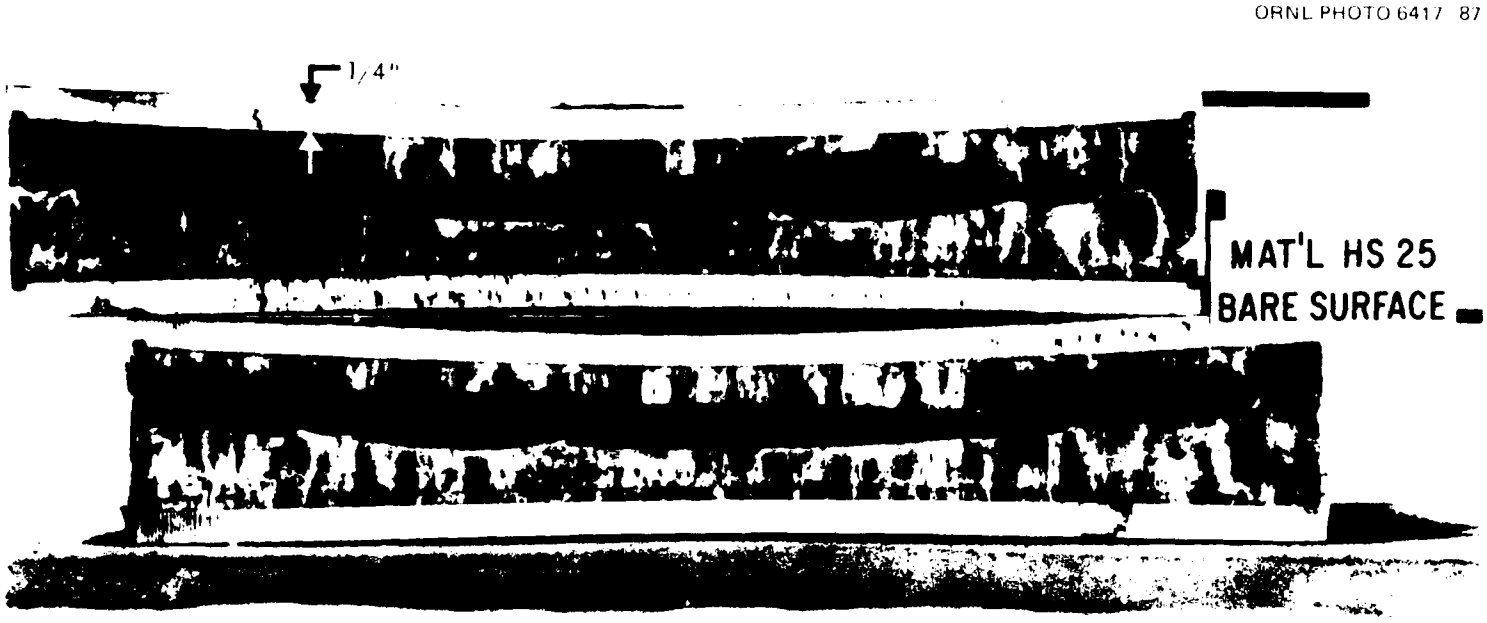

Fig. 4.6a. View of TRW module no. 2 sectioned after completion of testing.

Fig. 4.6a source: TRW Power Systems Department, "Brayton Cycle Cavity Receiver Design Study," TRW Equipment Laboratories, NASA CR-54752 ER-6497, Nov. 22, 1965, Fig. 35, p. 70.

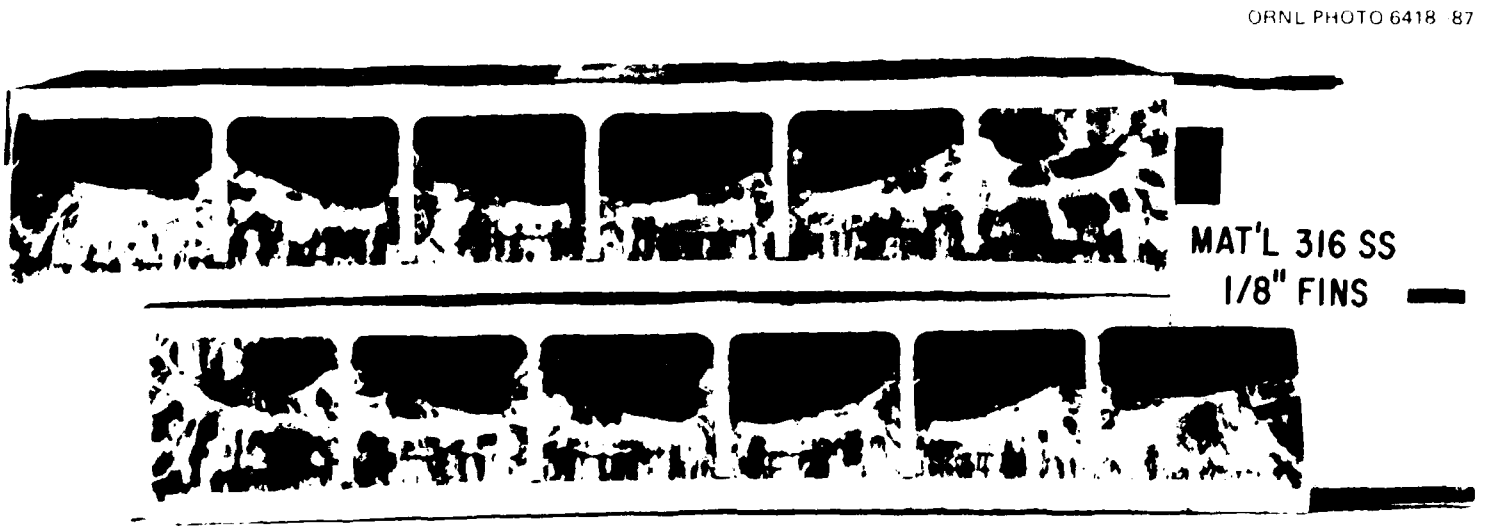

Fig. 4.6b. View of TRW module no. 4 sectioned after completion of testing.

Fig. 4.6b source: TRW Power Systems Department, "Brayton Cycle Cavity Receiver Design Study," TRW Equipment Laboratories, NASA CR-54752 ER-6497, Nov. 22, 1965, Fig. 36, p. 71.

ORNL PHOTO 75228A

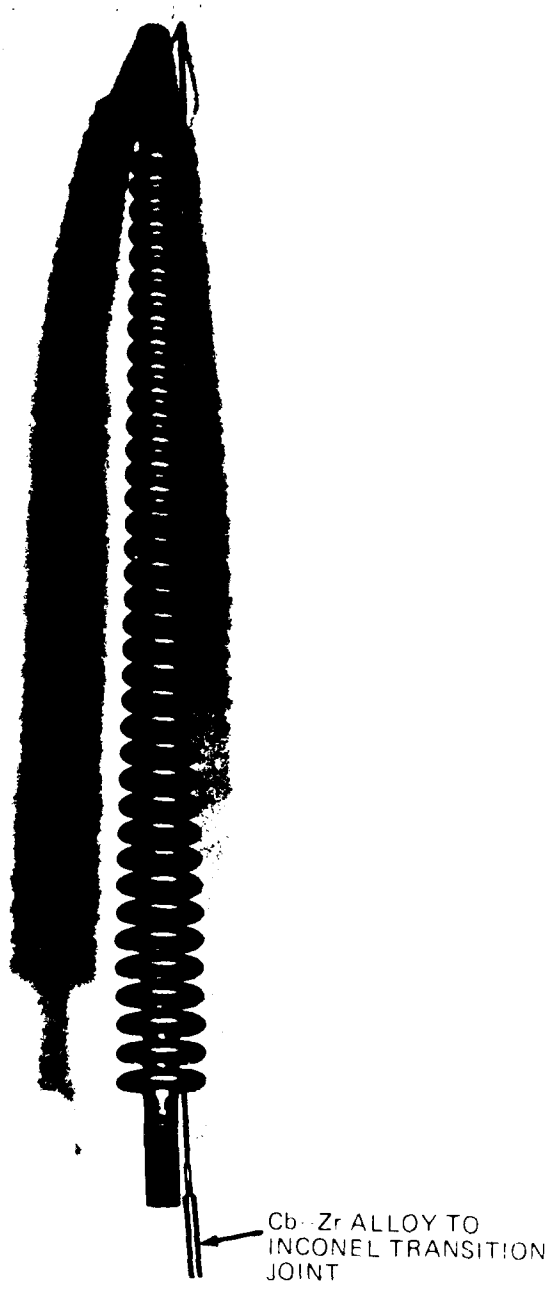

Fig. 4.7. Brayton-cycle heat storage tube.

Fig. 4.7 source: Gnadt, P. A., "Filling Heat Storage Tubes for Solar Brayton-Cycle Heat Receiver with Lithium Fluoride," Oak Ridge National Laboratory, ORNL/TM-2732, July 1970, Fig. 2, p. 4.

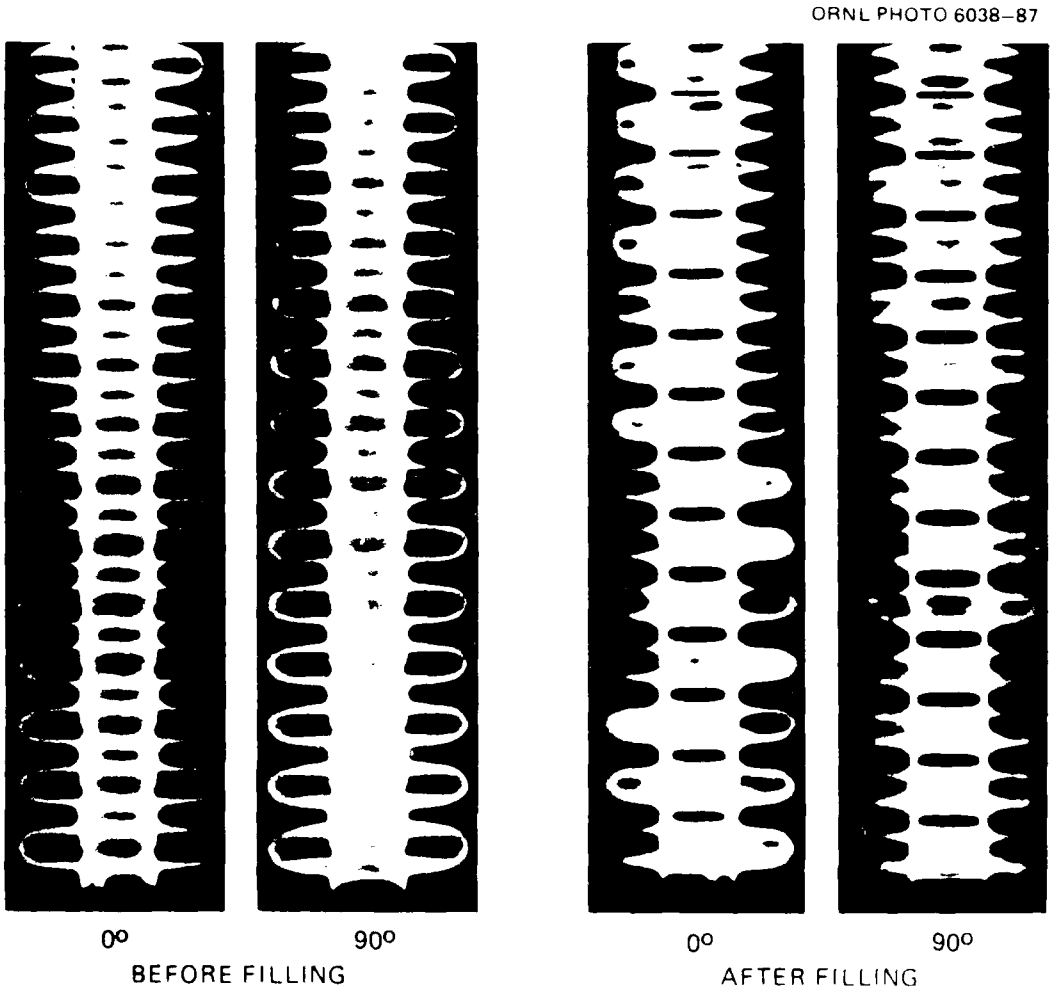

Fig. 4.8. X-rays of heat storage tubes.

Fig. 4.8 source: Gnadt, P. A., "Filling Heat Storage Tubes for Solar Brayton-Cycle Heat Receiver with Lithium Fluoride," Oak Ridge National Laboratory, ORNL/TM-2732, July 1970, Fig. 28, p. 61.

was not too surprising since the can was virtually completely full of powder when the weld was made. The weld was made with some difficulty as lithium hydride melted and made contact with the welded surfaces. Test C-3 was conducted in a similar fashion to Test C-1 with one cycle being performed from room temperature to ~1000 K and then back to room temperature.

Test C-3 temperature and pressure behavior was similar to that observed in test C-1 and C-2; however, the maximum pressure observed in

test C-3 was slightly lower (~80 mmHg). Post-test examination revealed that lithium hydride had "crawled" up the fill-tube and entered the flexible tubing as observed in test C-2. Although not apparent during the conduct of test C-3, lithium hydride leaked from the can, and solidified in the MgO. The MgO/LiH mixture formed a hard material which bonded tightly to the test can and beaker making it very difficult to remove the can. The can was removed by chiselling the MgO/LiH mixture from the can and beaker.

With the leakage of lithium hydride into the MgO, and the loss of lithium hydride up the fill-tube, a significant amount of lithium hydride was lost from the can. Radiographs of the test C-3 can show a void located as sketched in Fig. 4.9. Apparently, the lithium hydride was able to "crawl" up the can walls and exit through the opening(s) where the weld failure(s) occurred.

As mentioned previously, in tests C-1, C-2, and C-3 extensive cracking was observed (visually or radiographically) in the cast lithium hydride after cooldown (for example, see Fig. 4.4), and is most easily seen in radiographs. Lithium hydride cracking has been observed by others, namely Waldrop[24] who reports:

> "... some cracks are always present in finished [lithium hydride] casting of any appreciable size ... we have found it possible to prepare casting of considerable size which are sound, in the sense that there is no pipe, although there are numerous cracks."

Studies by Rapp at Thompson Ramo Wooldrige, Inc., as reported in Ref. 24, also indicate the formation of lithium hydride cracks following casting. Cracks were observed in a slab casting ~30-cm long, 15-cm wide, and 1.27-cm thick.

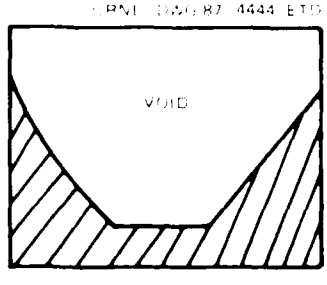

Fig. 4.9. Sketch of void shape, size, and location after testing C-3 can.

4.2 Development of Large, High Heat Rate Furnace

4.2.1 Graphite induction furnace performance

Comparison between the capsule experiments performed thus far and conditions anticipated in the "real system" show some very important differences, other than the obviously small number of cycles experimentally performed. As indicated previously, operational heatup times from ~700 to 1100 K will be on the order of 10 min, whereas the laboratory procedure required hours.

In order to obtain "real system" heatup times, an existing Y-12 Plant graphite induction furnace will be modified and used for cycle testing. The furnace is cylindrical with a peak operational power of about 60 kW, and about 0.01 m^3 (0.4 ft^3) of heated volume. The size and power of the furnace will permit multiple sample testing.

Initial heatup tests were performed with the furnace in its current configuration to assess its performance capabilities.[58] A sketch of the furnace cross-section is provided in Fig. 4.10. As shown the furnace contained a rather large graphite sample to provide some thermal mass.

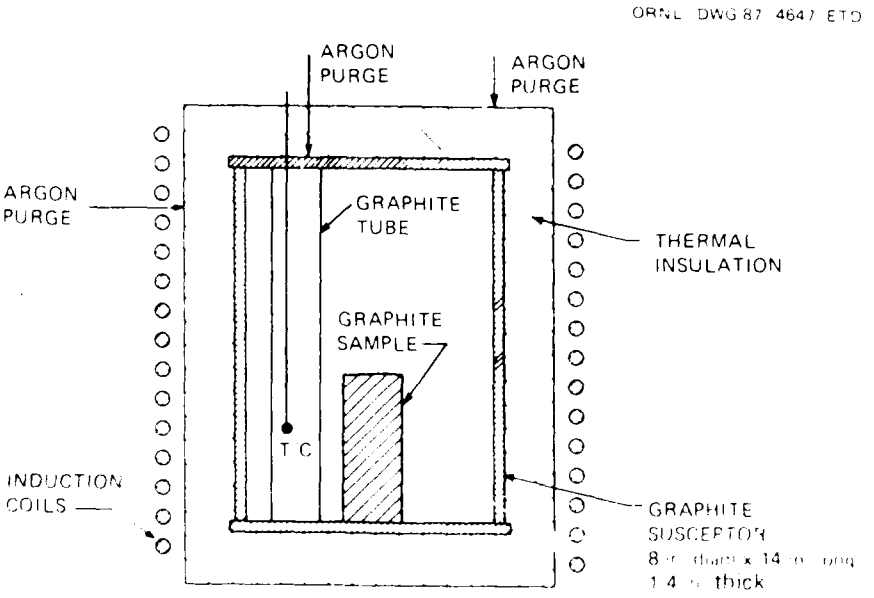

Fig. 4.10. Cross-sectional sketch of cylindrical graphite induction furnace.

In addition, the thermocouple was placed inside a graphite tube, which also provided thermal mass. Figure 4.11 shows the thermocouple response during two heatups, and the following cooldowns. During operation the system was purged with argon flowing at 0.003 m^3/min (0.1 ft^3/min). Following a brief, low power pre-heat, the furnace power was ramped quickly to 60 kW. In the first cycle (denoted "R1" in Fig. 4.11), the thermocouple temperature rose from ~150°C to a peak temperature of ~915°C over about 10 min. Furnace power was shut-off when the temperature reached 850°C. Following cooldown to ~300°C, a second cycle ("R2") was performed with similar results.

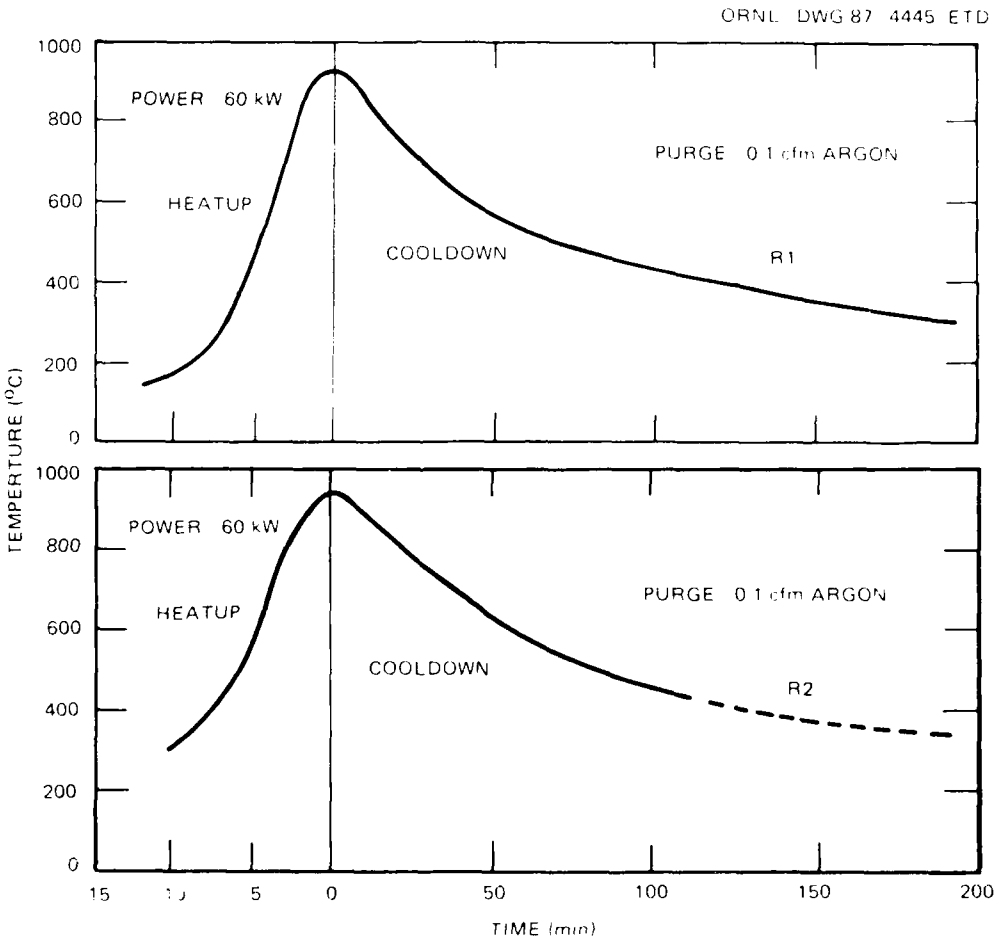

Fig. 4.11. Graphite induction furnace performance in current configuration.

Fig. 4.11 source: Wrenn, George, Y-12 Plant, Martin Marietta Energy Systems, Inc., Oak Ridge, TN, January 1987.

These data indicate that rapid heatups can be obtained in the induction furnace. It is anticipated that improvements in performance could be obtained by removing some of the thermal insulation, and reducing the susceptor wall thicknesses.

4.2.2 Projected performance of furnace

As described above, checkout tests of the 60 kW induction furnace indicate that a graphite sample can be heated in the furnace at a rate of about 100 K/min (180°F/min). In order to estimate the thermal response of a sphere containing lithium hydride being heated in the furnace, a computer simulation was carried out assuming the furnace radiates as a blackbody initially at ambient temperature with the furnace temperature increasing at a rate of 100 K/min (180°F/min). Lithium hydride contained in a 7.62-cm diameter, 0.0381-cm (15-mil) thick spherical stainless steel shell is surrounded by a muffle which is a 10.2-cm inside diameter, 0.076-cm thick, concentric sphere made of niobium. The muffle is exposed to radiation from the furnace. All surfaces are assumed to have an emissivity of 0.8, and all heat transfer is by radiation with no heat losses from the muffle or lithium hydride.

The resulting temperature profile in the solid lithium hydride at the initiation of melting is shown in Fig. 4.12. Also shown in Fig. 4.12 is the predicted temperature profile at the initiation of melting resulting from suddenly exposing a sphere with an initial temperature of 600 K (620°F) to convection heat transfer from NaK at 1100 K (1520°F), and the corresponding profile obtained in a low flux furnace (with an assumed heatup rate of 200 K/h or 360°F/h). It can be seen that while the average temperature of the solid in the high flux furnace sample is much higher than that expected in the real case, much of the solid is cold enough to retain some mechanical strength. Thus, some of the stress-related problems previously discussed are likely to be observed in tests conducted in the high-flux furnace. On the other hand, in low flux furnace tests the solid is all very close to the melt point at the time melting begins and it is not likely that stress problems will occur.

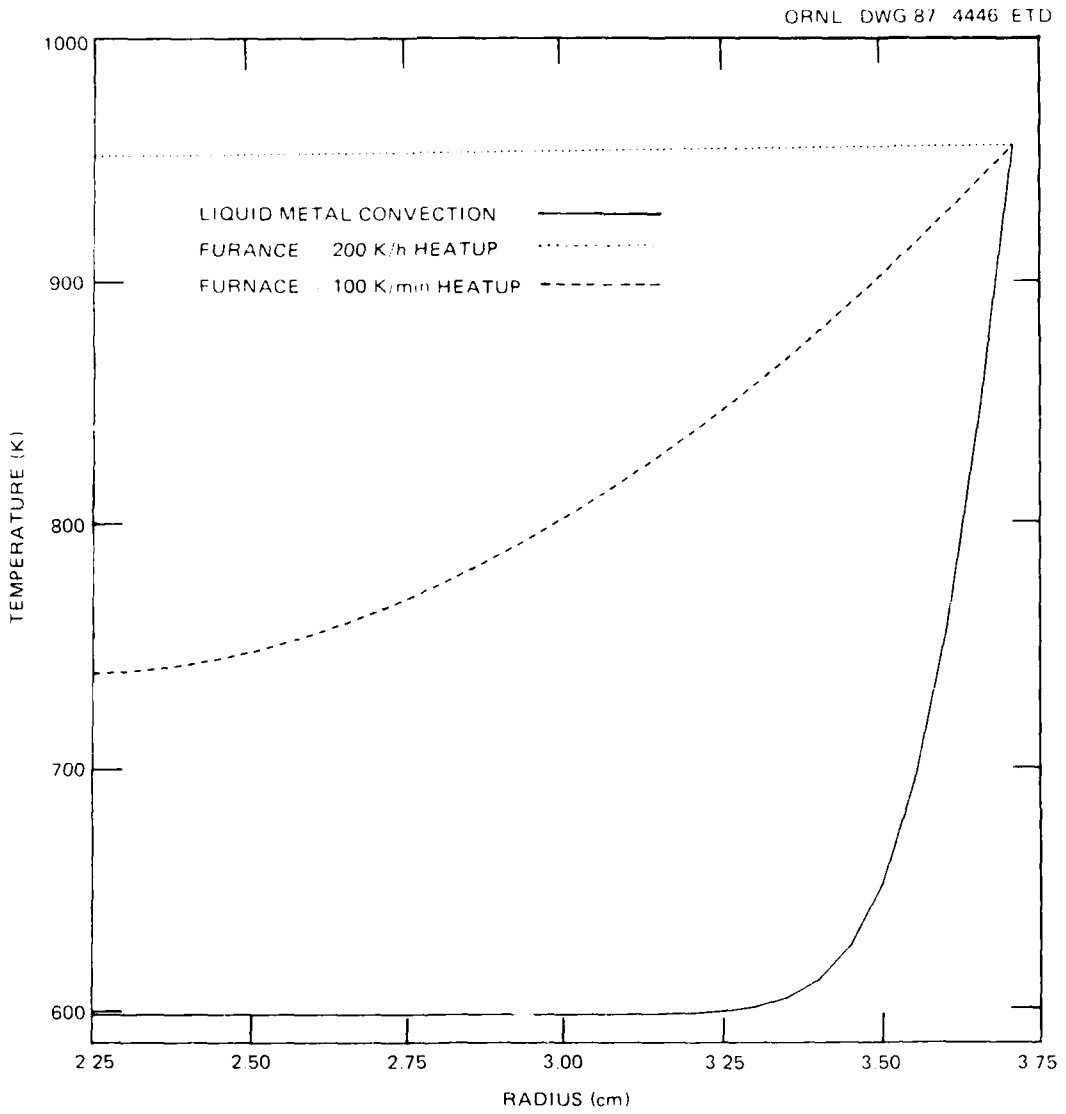

Fig. 4.12. Calculated lithium hydride temperature profiles at initiation of melting.

5. CONCLUSIONS

Based on preliminary system concept analysis, encapsulated lithium hydride thermal energy storage provides significant benefits to space burst power systems. The use of encapsulated Li^6H in a packed bed with a 75% packing density along with a lithium coolant, will provide calculated system mass benefits for burst periods as long as 800 s. In addition, the use of thermal storage will permit large reductions in radiator area, with larger benefits at shorter burst periods.

A group of feasibility issues associated with encapsulated lithium hydride thermal energy storage have been identified and studied. The feasibility issues include:

1. phase-change induced shell stress on heatup,
2. hydrogen diffusion and loss,
3. lithium hydride heat transfer,
4. void behavior/management, and
5. material considerations.

The key issue of concern is the possible large shell stress induced during heatup. Elastic analysis indicates that very thick shells will be required to prevent shell rupture, assuming the lithium hydride forms a structurally sound shell following solidification. However, cracks in the lithium hydride which have been observed to form during cooldown, may mitigate shell stresses and permit the use of a thin shell. Nevertheless, analysis has shown that void control, via sphere heat transfer control, can reduce significantly phase-change induced shell stress. In addition, optimization studies have indicated the benefit of high minimum storage temperatures (~500 to 700 K), at which lithium hydride has much less compressive strength. Alternatively, a flexible shell, such as a bellows, may be viable.

Based on material consideration, 304L stainless steel and molybdenum are leading candidate shell materials. Material considerations included material compatibility between the shell and lithium hydride, lithium and hydrogen, ductility, strength, density, material cost, and ease of fabrication. The refactory metals niobium, tantalum, titanium, and zirconium have been eliminated from consideration due to hydrogen

embrittlement. It was determined that SiC is not compatible with lithium at ~1100 K. Other ceramic materials have been eliminated primarily due to their poor thermal shock resistance. Molybdenum and 304L stainless steel possess reasonable ductility and moderate density. Molybdenum has greater strength and better material compatibility than 304L stainless steel, but is more expensive and harder to fabricate.

Based on projected system requirements, a 0.0127-cm (5-mil) stainless steel shell will provide sufficient hydrogen containment to prevent significant hydrogen loss, and associated loss of energy storage density. Due to molybdenum's lower hydrogen permeability, a molybdenum shell as thin as 1 mil could be used without significant hydrogen loss.

Initial scoping experiments have been completed for cylindrical cans, 2.54-cm long, 3.81-cm diameter, and 0.0635- and 0.0889-cm (25- and 35-mils) thick. Four thermal cycles were successfully completed in a low heat flux furnace for a 0.0889-cm (35-mil) can. Post-test examination of all cans tested show the presence of numerous cracks in the lithium hydride.

Future experimental work will be directed at determining the feasibility of using a thin-wall container. To this end, an existing, high power graphite induction furnace will be modified and used to simulate, as closely as possible, "real system" performance. The material and fabrication costs associated with using 304L stainless steel and molybdenum will be investigated. Presumably, both materials will be tested and will permit not only an assessment of shell heatup stress, but also hydrogen loss, material compatibility, and lithium hydride heat transfer.

Future analytical work will extend current capability to include the effect of surface tension gradients on void shape, void location, and liquid flow, and boundary layer effects on the void. In addition, the void and natural convection models will be integrated into the heat transfer code. These models, in addition to models for stress analysis and hydrogen loss, can then be compared to data to determine consistency.

Since the micro-gravity space environment will produce different behaviors than those on Earth, some basic verification tests should be

performed in space to determine the accuracy of model assumptions and results, and whether all important differences have been anticipated.

REFERENCES

1. Wetch, J. R., Space Power Inc., San Jose, CA, personal communication to Olszewski, M., Oak Ridge National Laboratory, Martin Marietta Energy Systems, Inc., Oak Ridge, TN, March 1986.

2. Olszewski, M. and Morris, D. G., "Energy Storage Concepts for Use in Sprint Power," Fourth Symposium on Space Nuclear Power Systems, Albuquerque, NM, January 12--16, 1987.

3. Solomon, A. D. et al., "Development of a Simulation Code for a Latent Heat Thermal Energy Storage System in a Space Station," ORNL-6213, April 1986.

4. Elrod, D. C. et al., "HEATING6; A Multidimensional Heat Conduction Analysis with the Finite Difference Formulation," NUREG/CR-0200, October 1981.

5. Patankar, S. V., "Numerical Heat Transfer and Fluid Flow," Hemisphere Publishing Co., 1980.

6. Stewartson, K. and Waechter, "On Stefan's Problem for Spheres," Proc. R. Soc. Lond. A.348, 415—526 (1976).

7. Hsu, C. J., "Heat Transfer to Liquid Metals Flowing Past Spheres and Elliptical Rod Bundles," Int. J. Heat Mass Transfer," Vol. 8, 303—315 (1965).

8. Adamson, A. W., "Physical Chemistry of Surfaces," John Wiley and Sons, 1976.

9. Hastings, L. J. and Rutherford, R., "Low Gravity Liquid-Vapor Interface Shapes in Axisymmetric Containers and a Computer Solution," NASA TM X-53790, October 1968.

10. Landau, L. D. and L'Fshitz, E. M., "Fluid Mechanics" Pergamon Press, 1959.

11. Reynolds, W. C. et al., "Capillary Hydrostatics and Hydrodynamics at Low g," Stanford University Report No. LG-3, September 1964.

12. McGrew, J. L. and Larkin, B. K., "Cryogenic Liquid Experiments in Orbit. Vol. II: Bubble Mechanics, Boiling Heat Transfer, and Propellant Tank Venting in a Zero-Gravity Environment," NASA CR-652, December 1966.

13. Levich, V. G., "Physiochemical Hydrodynamics," Prentice-Hall, 1962.

14. Kays, W. M. and Crawford, M. E., "Convective Heat and Mass Transfer, 2nd ed.," McGraw-Hill, 1980.

15. Oliver, Douglas L. R., "Issues Related to Lithium and Lithium-Hydride Thermal Storage Spheres," for Wright-Patterson Air Force Base, Contract No. F49620-85-C-0013, August 28, 1986.

16. Higdon, A., Ohlsen, E. H., Stiles, W. B., Weese, J. A., and Riley, W. F., *Mechanics of Materials*, John Wiley and Sons, Inc., 3rd edition, pp. 147—157, 1976.

17. Timoshenko, S. and Goodier, J. N., *Theory of Elasticity*, McGraw-Hill Book Company Inc., 2nd edition, pp. 356—359, 1951.

18. Anon., "Nuclear Propulsion Program Engineering Progress Report," PWAC-604, Oct. 1-Dec. 31, 1960, Pratt and Whitney Aircraft Corp., Jan. 31, 1961, pp. 88—89.

19. Anon., "Nuclear Propulsion Program Engineering Progress Report," PWAC-611, Jan. 1—Mar. 31, 1961, Pratt and Whitney Aircraft Corp., Apr. 18, 1961.

20. Welch, Frank H., "Properties of Lithium Hydride III. Summary of GE-ANP Data," XDC-61-5-67, Aircraft Nuclear Prop. Dept., General Electric Co., May 1961, p. 7.

21. Hoke, John H., "Mechanical Properties of Stainless Steels at Elevated Temperatures," pp. 21-1—21-20 in *Handbook of Stainless Steels*, Peckner, Donald, and Bernstein, I. M., editors, McGraw-Hill Book Company, 1977.

22. Anon., "Refractory Metals and Custom Fabrication," Rembar Company, Inc.

23. Waldrop, F. B., "Lithium Hydride as a Mobile Neutron Shield," Y-1191, Union Carbide Nuclear Corp., February 24, 1958, p. 7-8.

24. Smith, Roger L., and Miser, James W., "Compilation of the Properties of Lithium Hydride," NASA-TM-X-483, 1962. a, p. 171—200; b, p. 121—140; c, p. 171—195.

25. Ugural, A. C., "Stresses in Plates and Shells," McGraw-Hill, 1981.

26. Veleckis, Ewald, Deventer, Erven H. Van, and Blander, Milton, "The Lithium-Lithium Hydride System," in *The Journal of Physical Chemistry*, Vol. 78, No. 19, 1974, p. 1933—1940.

27. Flint, P. S., "The Diffusion of Hydrogen Through Materials of Construction," Knolls Atomic Power Laboratory, KAPL-659, December 14, 1951.

28. Braunstein, J., Oak Ridge National Laboratory, Martin Marietta Energy Systems, Inc., Oak Ridge, TN, personal communication to Morris, D. G., Oak Ridge National Laboratory, Martin Marietta Energy Systems, Inc., Oak Ridge, TN, March—April 1987.

29. Mahefkey, E. T., Air Force Weight Aeronautical Laboratories, AeroPropulsion Laboratory, Dayton, Ohio, personal communication to D. G. Morris, Oak Ridge National Laboratory, Martin Marietta Energy Systems, Inc., Oak Ridge, TN, January 1987.

30. Hamill, C. W., "Stress Corrosion Testing of Various Alloys," Union Carbide Nuclear Company, in "Lithium Hydride as a Thermal Energy Storage Material," Woods, Frank L., Wannemacher, Marvin P., and Houck, Oscar O., editors, Wright-Patterson Air Force Base, ASD-TR-61-427, May 1962, pp. 67—69 and pp. 75—79.

31. May, J. R., and Conrad, R. R., "Sundstrand Aviation-Denver," in "Lithium Hydride as a Thermal Energy Storage Material, Woods, Frank L., Wannemacher, Marvin P., and Houck, Oscar O., editors, Wright-Patterson Air Foce Base, ASD-TR-61-427, May 1962, pp. 31—46.

32. Royer, L. T., Y-12 Plant, Martin Marietta Energy Systems, Inc., Oak Ridge, TN, personal communication to Morris, D. G., Oak Ridge National Laboratory, Martin Marietta Energy Systems, Inc., Oak Ridge, TN, February, 1987.

33. Messer, Charles E., "A Survey Report on Lithium Hydride," NYO-9470, AEC, October 27, 1960, p. 41.

34. Welch, F. H., "Properties of Lithium Hydride-V: Corrosion of Austenitic Stainless Steels in Molten LiH," General Electric Company, APEX-673, August, 1961 a, p. 63.

35. Welch, F. H., "Properties of Lithium Hydride II, Lithium Hydride Corrosion Studies: 19-9 DL Alloy," General Electric Company, APEX-586, April 10, 1961.

36. Atomic Energy Commission, Dept. of the Navy, *Liquid-Metals Handbook*, June 1952.

37. Cowles, J. O. and Pasternak, A. D., "Lithium Properties Related to Use as a Nuclear Reactor Coolant," Lawrence Radiation Laboratory, UCRL-50647, April 18. 1969, pp. 34—35.

38. Cook, W. H., "Corrosion Resistance of Various Ceramics and Cermets to Liquid Metals," Oak Ridge National Laboratory, ORNL-2391, May 31, 1960.

39. McCoy, H. E. and Douglas, D. A., "Effect of Various Gaseous Contaminants on the Strength and Formability of Columbium," Oak Ridge National Laboratory, in *Columbium Metallurgy*, Douglass, D. L., and Kunz, F. W., editors, Interscience Publishers, New York, London, June 1960, pp. 85—118.

40. Hampel, Clifford A., "Tantalum," pp. 469-518, in *Rare Metals Handbook*, 2nd edition, Hampel, Clifford A., editor, Reinhold Publishing Corporation, 1961, p. 505.

41. Ogden, H. R., "Titanium,' pp. 559-579, in *Rare Metals Handbook*, 2nd edition, Hampel, Clifford A., editor, Reinhold Publishing Corporation, 1961, pp. 572—573.

42. Paton, N. E. and Williams, J. C., "Effect of Hydrogen on Titanium and Its Alloys," pp. 185-207, in *Titanium and Titanium Alloys*, Donachie, Matthew, J., Jr., editor, American Society for Metals, 1982.

43. Schlechten, A. W., "Zirconium," pp. 667-686, in *Rare Metals Handbook*, 2nd edition, Hampel, Clifford A., editor, Reinhold Publishing Corporation, 1961, p. 675.

44. Melaven, A. D., "Rhenium," pp. 418-433 in *Rare Metals Handbook*, 2nd edition, Hampel, Clifford A., editor, Reinhold Publishing Corporation, 1961, p. 428.

45. Li, K. C., "Tungsten," pp. 480-597 in *Rare Metals Handbook*, 2nd edition, Hampel, Clifford A., editor, Reinhold Publishing Corporation, 1961, p. 589.

46. Westphal, D. A. and Worzala, F. J., "Hydrogen Attack of Steel," pp. 79-89, in *Hydrogen In Metals*, Bernstein, I. M., and Thompson, Anthony, W., editors, American Society for Metals, 1974.

47. Morris, L. A., "Corrosion Resistance of Stainless Steels at Elevated Temperatures," pp. 198-215, in *Source Book on Materials for Elevated Temperature Applications*, Bradley, Elihu, F., editor, American Society for Metals, 1979, p. 209.

48. Hoyt, Samuel L., editor, *Metals Properties*, McGraw-Hill Book Company, 1st edition, 1954, p. 3—4.

49. Touloukian, Y. S., editor, *Thermophysical Properties of High Temperature Solid Materials*, Volume 3: Ferrous Alloys, Thermophysical Properties Research Center, Purdue University, the Macmillian Company, 1967. a, p. 55; b, p. 145.

50. McGannon, Herold E., "Iron and Steel," p. 6-12—6-46, in *Marks' Handbook for Mechanical Engineers*, 8th edition, Baumeister, Theodore, Avallone, Eugene A., and Baumeister, Theodore, III, editors, McGraw-Hill Book Company, 1979, p. 6—40.

51. Simmons, Ward F., and Echo, John A. Van, "The Elevated-Temperature Properties of Stainless Steels," American Society for Testing and Materials, ASTM Data Series Publication DS 5-S1, 1965, p. 20.

52. Hague, J. R. et al., editors, "Refactory Ceramics for Aerospace," The American Ceramic Society, Inc., 1964, pp. 93—151.

53. Bechtold, J. H., Wessel, E. T. and France, L. L., "Mechanical Behavior of the Refractory Metals," pp. 25-81 in *Refractory Metals and Alloys*, Semchyshen, M. and Harwood, J. J., editors, Interscience Publishers, 1961, pp. 37—38.

54. Wrenn, George, Y-12 Plant, Martin Marietta Energy Systems, Inc., Oak Ridge, TN, personal communication to Morris, D. G., Oak Ridge National Laboratory, Martin Marietta Energy Systems, Inc., Oak Ridge, TN, March 1987.

55. Berberich, Lois E., The Rembar Company, Inc., Dobbs Ferry, New York, personal communications to Morris, D. G., Oak Ridge National Laboratory, Martin Marietta Energy Systems, Inc., Oak Ridge, TN, February and March 1987.

56. TRW Power Systems Department, "Brayton Cycle Cavity Receiver Design Study," TRW Equipment Laboratories, NASA CR-54752 ER-6497, November 22, 1965.

57. Gnadt, P. A., "Filling Heat Storage Tubes for Solar Brayton-Cycle Heat Receiver with Lithium Fluoride," Oak Ridge National Laboratory, ORNL-TM-2732, July 1970.

58. Wrenn, George, Y-12 Plant, Martin Marietta Energy Systems, Inc., Oak Ridge, TN, personal communication to Morris, D. G., Oak Ridge National Laboratory, Martin Marietta Energy Systems, Inc., Oak Ridge, TN, January 1987.

ORNL/TM-10413

Internal Distribution

1. W. L. Asbury
2. L. Berry
3. J. A. Getsi
4. H. E. Guinn
5. H. W. Hoffman
6. C. E. Irwin
7. A. A. Kahn
8. S. C. Loggis
9. J. R. Merriman
10-14. D. G. Morris
15-19. M. Olszewski
20. L. T. Royer
21. C. M. Sigler
22. M. Siman-Tov
23. H. E. Trammell
24. R. P. Wichner
25. G. E. Wrenn
26. ORNL Patent Office
27. Document Reference Section
28. Central Research Library
29-30. Laboratory Records Department
31. Laboratory Records (RC)

External Distribution

32. Office of Assistant Manager for Energy Research and Development, Department of Energy, ORO, Oak Ridge, TN 37831
33. E. B. Kennel, AFWAL/POOS, Wright-Patterson AFB, Ohio 45433
34-37. AFWAL/POOS, Aeronautical Laboratory, Wright-Patterson AFB, Ohio 45433
    W. Borger
    E. T. Mahefky
    J. Beam
    J. Johnson
38-39. EG&G Idaho, Inc./INEL, P.O. Box 1625, Idaho Falls, ID 83415
    R. Rice
    J. F. Whitbeck
    J. Martinell
40-41. GA Technologies, P.O. Box 85608, San Diego, CA 92138
    C. Fisher
    G. Fitzpatrick
42. R. Giellis, Martin Marietta Corp., P.O. Box 179, Denver, CO 80201
43-44. Sandia National Laboratory, Albuquerque, NM 87185
    W. H. McCulloch
    F. Wyant
45-46. NASA Lewis Research Center, 21000 Brookpark Road, Cleveland, OH 44135
    Ted Mroz
    J. Sovie, MS 301-5
47. R. Verga, SDI Organization, The Pentagon, Washington, DC 20301-7100
48. A. D. Schoenfeld, TRW, One Space Park, Redondo Beach, CA 90278
49. J. R. Wetch, Space Power Inc., 1977 Concourse Drive, San Jose, CA 95131

50. S. H. Winkler, Grumman Aircraft Systems, Bethpage, NY 11714-3582
51. E. Wahlquist, U.S. Department of Energy, NE-54, F415/GTN, Germantown, MD 20545
52. J. P. Foote, Dept. of Mechanical Engineering, U.T. Space Institute, Tullahoma, TN 37388
53. Dr. Leon Bledjian, Aerospace Corporation, Box 92957 D8/M4-916, Los Angeles, CA 90009
54. Dr. Scott Samuelson, San Francisco DOE Ops, 1333 Broadway, Oakland, CA 94612
55. Major Joe Sholtis, [illegible] DOE, NE-50, Washington, DC 20545
56. Dr. Roger K. Wedel, Lockheed Missile Sys. Corp., Dept. 51-21, B586, Box 3504, Sunnyvale, CA 94088-3504
57. Dr. Wen Chiu, General Electric VPSC, P.O. Box 8555, Philadelphia, PA 19101
58. Mr. Irvin Adler, Hughes Aircraft Company, P.O. Box 9919, Bldg. S-41, MS A315, Los Angeles, CA 90009
59. Dr. Howard Collicott, Boeing Aerospace Corp., P.O. Box 3999, MS 82-23, Seattle, WA 78124
60. Dr. Dave Buden, SDIO/SLKT, The Pentagon, Washington, DC 20301-7100
61. Capt. Mike Brasher, AFSTC/TPC, Kirtland AFB, NM 87117-6008
62. Mr. G. Allen Beale, RPL/LKCS, Edwards AFB, CA 93523
63. Mr. Leroy Herold, TRW Electronics & Defense, Bldg. 4, Rm. 2066, One Space Park, Redondo Beach, CA 90278
64. Mr. H. S. Bloomfield, NASA LeRC, MS 301-5, Cleveland, OH 44135
65. Dr. Richard E. Rice, USDOE Idaho Ops Office, P.O. Box 2245, Idaho Falls, ID 83403-2245
66. Robert Brengle, Rockwell International, 6633 Canoga Ave. Canoga Park, CA 91303
67. DTIC, Cameron Station, Alexandria, VA 22304-6145
68. AUL/LSE, Maxwell AFB, AL 36112
69. AFWAL/IMST, Bldg. 22, WPAFB, OH 45433
70. Dr. E. T. Curran, AFWAL/PS, WPAFB, OH 45433-6563
71. Michael R. Beltran, Beltran Inc., 1133 E. 35th St., Brooklyn, NY 11210
72. Dr. Michael Hsu, Ztek Corp., 400-2 Totten Pond Rd., Waltham, MA 02154
73. Javier A. Valenzuela, Creare, Inc., P.O. Box 71, Etna Road, Hanover, NH 03755
74. Ned S. Rasor, Rasor Associates, 253 Humboldt Ct., Sunnyvale, CA 94086
75. Dr. Jack Holman, Mechanical Engineering Dept., Southern Methodist University, Dallas, TX 55275
76. Dr. Nils Diaz, 202 NSC Univeristy of Florida, Gainesville, FL 32611
77. Dr. Dean Jacobson, Dept. of Chemical & Bio Engineering, Ari[illegible] State University, Tempe, AZ 85287
78. Mr. Bob Campana, ElectroTechnologies Corp., [illegible] Ste G, San Diego, CA 92121
79. Roger Demler, Foster-Miller Corp, 350 Second [illegible] 02254

AD-A198 689 DEVELOPMENT OF ENCAPSULATED LITHIUM HYDRIDE THERMAL ENERGY STORAGE FOR SP (U) OAK RIDGE NATIONAL LAB TN ENGINEERING TECHNOLOGY DIV D G MORRIS ET AL DEC 87 2/2

UNCLASSIFIED ORNL/TM-10413 DE-AC05-84OR21400 F/G 10/4 NL

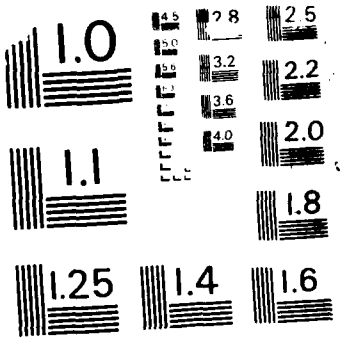

80. Harold T. Couch, HTC Inc., 11 Canaan Way, Simsbury, CT 06070
81. Jerome E. Toth, Thermacore Inc., 780 Eden Road, Lancaster, PA 17601
82. David Chittenden, L'Garde Inc., 1555 Placentia Ave., Newport Beach, CA 92663-2870
83. W. J. Carr, Jr., WJC ReSEARch and Development, 1450 Jefferson Hts., Pittsburgh, PA 15235
84. Dr. Mike Schuller, AFWL/AWYS, KAFB, NM
85-115. Technical Information Center, Department of Energy, Oak Ridge, TN 37831

☆ U.S. GOVERNMENT PRINTING OFFICE 1988—548-118/60135

END

DATE

FILMED

DTIC

4/88